UAB

Universitat Autònoma de Barcelona

Doctoral Thesis

DEVELOPMENT OF SENSORS BASED IN MEMS WITH MECHANOCHROMIC RESPONSE

Pedro Fernando Escudero Villa

Supervisor: María del Mar Alvarez Sánchez

Tutor: Jordi Aguiló Llobet

Submitted in partial fulfilment of the requirements for the degree of

Doctor of Philosophy in Electronic Engineering and Telecommunications

Universidad Autónoma de Barcelona
Departamento de Electrónica y Sistemas Electrónicos
Programa de Doctorado en Ingeniería Electrónica y de Telecomunicación

Bellaterra(Barcelona), junio 2019

Dra. **María del Mar Alvarez Sanchez**, investigadora del Instituto de Microelectrónica de Barcelona, y Dr. **Jordi Aguiló Llobet**, catedrático del Departamento de Microelectrónica y Sistemas Electrónicos de la Universidad Autónoma de Barcelona.
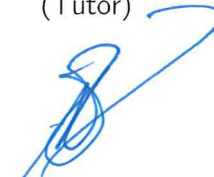
Certifican

que la memoria de tesis, **Development of sensors based in MEMS with mechanochromic response**, presentada por **Pedro Fernando Escudero Villa** para optar por el título de **Doctor en Ingeniería Electrónica y de Telecomunicación** se ha realizado bajo su dirección en el Instituto de Microelectrónica de Barcelona perteneciente al Centro Nacional de Microelectrónica del Consejo Superior de Investigaciones Científicas y ha sido tutelada en el **Departamento de Microelectrónica y Sistemas Electrónicos** de la Universidad Autónoma de Barcelona.

Dra. María Mar Alvarez Sánchez   Dr. Jordi Aguiló Llobet
(Directora)   (Tutor)

Bellaterra (Barcelona), Julio de 2019

A mi hijo Bastian…

Resumen

Los sensores nanomecánicos han sido reportados históricamente como una herramienta atractiva para la biodetección debido a su alta sensibilidad, alto rendimiento y alta integración. La mayoría de los sensores nanomecánicos se han fabricado con tecnología basada en silicio, pudiendo integrar miles de sensores en un solo chip. Sin embargo, el desarrollo de este tipo de sistemas implica no solo la fabricación de matrices de transductores mecánicos, que actualmente es un proceso muy establecido y de bajo costo, sino también la implementación de un sistema de lectura para leer independientemente la respuesta de cada transductor.

Esta tesis doctoral se centró en el desarrollo de un nuevo enfoque para la detección de la respuesta mecánica de una matriz de sensores mecánicos mediante el uso de instrumentación sencilla. Este enfoque consiste en el desarrollo de sensores mecánicos (microcantilevers y micromembranas) con respuesta mecanocrómica, es decir, sensores mecánicos que cambian su color intrínsecamente ante estimulación mecánica.

El desarrollo de sensores basados en MEMS con respuesta mecanocrómica es el resultado de una combinación efectiva de la coloración estructural producida por redes de difracción o cristales fotónicos, con el rendimiento de los transductores mecánicos. Los sensores mecánicos con una nanoestructura periódica dispuesta en una cara del sensor, son fabricados y caracterizados. El color mostrado por los sensores cambia intrínsecamente por la acción de un estímulo mecánico externo (carga de presión o tensión superficial) cuando el transductor se deforma, siendo el cambio de color recogido por el uso de un LED y una cámara RGB de bajo costo.

Para llevar a cabo este desarrollo, se realiza un estudio teórico de la física de coloración estructural y de modelos matemáticos que describen el principio de funcionamiento del dispositivo mecanocrómico. Con estos elementos básicos, los materiales mecanocrómicos basados en dos tipos de estructuras fotónicas, redes de difracción 1D y ensamblajes coloidales, son fabricados y caracterizados por espectrometría UV-Visible, identificando los principales contribuyentes del cambio de color (variaciones en el período de la nanoestructura y cambios en el

ángulo de iluminación de punto de vista). Estos materiales a continuación son integrados a matrices de sensores mecánicos colorimétricos para ser caracterizados por medio de tensión biaxial. Se fabrica, caracteriza y evalúa una matriz de sensores de presión colorimétricos basados en membranas flexibles nanoestructuradas y suspendidas, libres de marcajes y de alimentación de energía orientado a las aplicaciones optofluídicas multiplexadas. La plataforma muestra una sensibilidad de $0.17\,kPa^{-1}$ en la detección de presiones neumáticas bajas o de fluidos (en un rango entre -1 y $1\,kPa$) y se demuestra la idoneidad del método de detección colorimétrico midiendo el cambio de color de las membranas que muestran una sensibilidad de $117\,nm\,/\,kPa$. Finalmente, se realiza un estudio teórico de un sensor nanomecánico colorimétrico de tensión superficial basado en cantilevers y se demuestra su desempeño en la detección de cambios conformacionales moleculares fotoinducidos. De esta manera, el método de detección es capaz de detectar cambios de $1\,°$ en la escala de tono (HSV), o $0.75\,nm$ de longitud de onda en el rango visible ($400\,nm$ a $650\,nm$).

El desarrollo de sensores basados en MEMS con respuesta mecanocrómica se presenta como una herramienta útil que cumple con los requisitos para el desarrollo de un dispositivo de punto de atención, tales como: alta sensibilidad, bajo costo, alto rendimiento, libre de marcajes, de montaje externo, desechable, multidetección, y también que no requiere un sistema de detección sofisticado.

Abstract

Nanomechanical sensors have been historically reported as an attractive tool for biodetecction due to its high sensitivity, high throughput, and high integration. Most of nanomechanical sensors have been fabricated using silicon based technology being able to integrate thousands of sensors in a single chip. However, the development of this kind of systems involves not only the fabrication of arrays of mechanical transducers, which is currently a well-established and low-cost process, but also the implementation of a read-out system to independently read each transducer response.

This Doctoral Thesis focused on the development of a new approach for the detection of the mechanical response of an array of mechanical sensors by using simple instrumentation. This approach consists in the development of mechanical sensors (microcantilevers and micromembranes) with mechanochromic response, i.e. mechanical sensors with an intrinsic tunable colour under mechanical stimulation.

The development of sensors based in MEMS with mechanochromic response is a result of an effective combination of the structural coloration produce by diffraction gratings or photonic crystals, with the performance of mechanical transducers. Mechanical sensors with a periodical nanostructuration disposed on one face of the sensor, are fabricated and characterized. The colour displayed by the sensors change intrinsically by the action of an external mechanical stimulus (pressure load or surface stress) when the transducer deflects, being the colour change collected by the use of a LED and a low cost RGB camera.

In order to carry out this development, a theoretical study of the physics of structural coloration and the mathematical models that describe the working principle of the mechanochromic device is performed. With these basics, the mechanochromic materials based on two types of photonic structures, linear 1D gratings and colloidal assemblies, are fabricated and characterized by UV-Visible spectrometry, finding the main contributors of colour change (variations in the nanostructure period and changes in the illumination and point of view angle).

These materials are then integrated into arrays of coloured mechanical sensors and characterised under bi-axial strain. A label-free and power-free array of colour tunable pressure sensors based on flexible nanostructured suspended membranes is fabricated, characterized and evaluated for multiplexed optofluidics applications. The platform shows a sensitivity of $0.17\,kPa^{-1}$ for the detection of low pneumatic or fluid pressures (in a range between -1 and $1\,kPa$) and the suitability of colorimetric detection method is demonstrated by measuring the membrane colour change with a sensitivity of $117\,nm/kPa$. Finally, a theoretical study of a surface stress colorimetric nanomechanical sensor based in cantilevers is performed and demonstrated its performance for the detection of photo-induced molecular conformational changes. In this case, the detection method is able to detect changes of 1° in the hue scale (HSV) or $0.75\,nm$ for the visible band in wavelengths ($400\,nm$ to $650\,nm$).

The development of sensors based in MEMS with mechanochromic response is presented as a useful tool that fulfils the requirements for the development of a point-of-care device, such as: high sensitivity, low-cost, high throughput, label-free, out of the shelf, disposable, multidetection, and also that does not require a sophisticated detection system.

Agradecimientos

La paciencia es la actitud que lleva al ser humano a poder soportar contratiempos y dificultades para conseguir algo bien (Wikipedia). Por tanto, la realización de este trabajo ha sido posible gracias a la gran paciencia de muchas personas que han brindado su colaboración en el trabajo del día a día durante el tiempo de estancia en el Centro de Microelectrónica de Barcelona (IMB-CNM).

En primer lugar, quiero agradecer a mi director de tesis Mar Alvarez por su esfuerzo, orientación, y guía continua desde el primer día que llegué al IMB-CNM. El camino ha sido algo pedregoso y desorientador a mi parecer, aunque exagero al decir que el reinventar la rueda no es sencillo, y mucho más si se desea conseguir materializada una idea original trabajando en una línea de investigación alejada de mi formación. Muchas gracias Mar por tu ayuda, trabajo perseverante, amistad, y tu gran paciencia.

Quiero agradecer también a los integrantes del Grupo de Aplicaciones Biomédicas (GAB), Zea, Yeste, Moya, Martínez, Xavi, Eli, Antón, Gemma, Rosa, Miguel, y Javier por el buen ambiente de trabajo que me han brindado durante los cuatros años siendo parte del grupo. También a las personas que en su momento fueron parte del GAB y con las que he trabajado (Alba, Arnau, Rosella, Irina) y a los nuevos integrantes incluido Daniel.

Me gustaría agradecer a muchas de las personas del IMB-CNM (Marta D., Perla, Carolina, Xavi M., María Isabel, Marta M. Juan-Ma., Rafaela, Philippe, Steven, Michele, Paco S., Daniela...) que me han brindado su amistad y hemos podido compartir momentos de trabajo, de fiesta microelectrónica, o simplemente el cálido "Hola/Hey.!!" de cada día.

En este párrafo quiero agradecer a quienes conforman el departamento de becas de la Secretaria de Educación Superior, Ciencia, Tecnología e Innovación (Senescyt - Ecuador) por la financiación para la realización de estudios de postgrado, de la misma manera agradecer al Instituto de Fomento al Talento Humano (IFTH-Ecuador) por la gestión de la beca. Sigan adelante a pesar de las dificultades.

Finalmente, quiero agradecer a mi familia Patricia y Bastian por sobrellevar mi ausencia en el día a día, por ser la alegría que espero al salir del trabajo, la dulce distracción y el motivo de desconexión que necesito al llegar a casa. A mi familia que incondicionalmente me espera y me apoya desde Ecuador, mi Madre que es mi ejemplo a seguir por su inteligencia, carácter firme, generosidad, amor de madre, y su arduo trabajo, a mi Padre junto a mi docena de hermanos incluidos los adoptados políticamente, los llevo a todos siempre presente como un gran apoyo diario.

Table of Contents

Statement of Original Authorship

The work contained in this thesis has not been previously submitted to meet requirements for an award at this or any other higher education institution. To the best of my knowledge and belief, the thesis contains no material previously published or written by another person except where due reference is made.

Signature: _____

Date: ___17 - 07 - 2019_____

Motivation and objectives

Currently, there is a huge demand of rapid, accessible, and affordable tools for the decentralized analysis of samples in many different areas, including environmental, food analysis or healthcare. This has resulted in a further development of point-of-care (POC) devices, especially in the healthcare area for the diagnosis and prevention of diseases. The early detection of harmful agents and especially the early diagnosis of diseases, would significantly improve the prognosis and survival rate, reducing the duration and cost of treatments. The early diagnosis of many diseases or even the quality monitoring of our environment is only possible by the simultaneous detection of several analytes or compounds in a single sample. Currently, the number of POC devices found in the market is very large; however, most of them can only detect a single agent. More research effort must be directed to the development of new sensing techniques with a high multidetection capability, high sensitivity, and low energy consumption.

Nanomechanical sensors has demonstrated to be a powerful and promising tool for sensing and biosensing due to their small size, fast response, high sensitivity and their compatible integration into POC devices. Different works demonstrated the simultaneous detection of several transducers, up to sixteen, by using different detection systems. However the multiplexed capability for monitoring several surface stress transducers (each one associated with the detection of a specific compound) still presents important limitations related mainly with the integration of the read-out system when working with arrays of transducers (integration, alignment, power,...).

The Thesis constitutes the development of a novel sensing method that aims to solve the difficulties experienced by nanomechanical devices when carrying out the detection of multiple analytes. The developed approach born from the combination of the latest advances in nanostructured intelligent materials and the demonstrated high sensitivity of micro-electro-mechanical systems (MEMS) based on the change of surface stress. The development of this type of sensors and biosensors would allow the simultaneous detection of different analytes or compounds in a quantitative and rapid way, by means of colorimetric detection without the need of labelling, and by using a LED and a

low cost RGB camera. The colour change experienced by the mechanical sensors of an array during the detection processes is further quantified by using colour analysis software.

The proposed system is based on the development of arrays of polymeric suspended mechanical sensors (microcantilevers and membranes) with structural coloration derived from the diffraction of white light into the periodical nanostructures (linear gratings or two dimensional photonic crystals) fabricated in one of their surfaces. Polymeric nanostructured materials, in addition to being economical and easily manufactured in mass, have demonstrated a mechanochromic behaviour producing a change of colour of the material when subjecting them to deformation processes, mainly due to changes on the angle of interaction of the light and the distance between nanostructures.

The final aim of this Thesis is the development of a POC device that consist on an array of mechanical sensors, where each sensor of the array would respond in a unique and selective way to a certain analyte, parameter or factor, that produces a change in the surface stress induced bending, resulting in a variation of the colour diffracted by each sensor (mechanochromic response).

The achievement of this PhD Thesis represents a great advance in the development of multi-sensor systems for the detection and monitoring of different parameters, with a wide range of applications ranging from the monitoring of environmental parameters or water quality control, to the control and monitoring of diseases in an individualized way (personalized medicine).

With this scope, the specific objectives outlined in this work are listed as follow:

- To perform a theoretical study of the physics involved in the mechanical transduction for membranes and cantilevers including an optical analysis of structural coloration and its common structures; photonic crystals and diffraction gratings.

- To establish a robust fabrication method for the development of mechanochromic sensors based in elastomers such as PDMS and polymers such as polyimide, or SU-8.

- To establish a robust sensor integration method easily compatible with standard microfabrication processes.

- To develop an image acquisition method including the images processing to monitor the sensors colour change.

- To demonstrate the suitability of structural coloration (white light interference) as detection mechanism of mechanical sensors based in cantilevers or membranes.

- To demonstrate the potential application of structural colour mechanical sensors to the development of POC biosensors based in surface stress changes.

Thesis Outline

This thesis is organized in seven chapters as follow:

First chapter. – Introduction. This chapter provides an introduction to current technology and applications where the development of high sensitivity and multiplexed sensors based in MEMS are needed. It provides a general description of the state-of-the-art of point-of-care (POC) devices including a detailed description of current developments of mechanical (bio)sensors and its main detection methods. It also describes the developments of colorimetric detection. The last part of this chapter describes the main proposed approach idea of the development of an array of structural colored mechanical sensor.

Second chapter. – Physics of mechanical transducers and structural coloration. This chapter introduces the physics and mathematical models that describe the working principle of our device. It includes a description of the general mechanical behaviour of microcantilevers and micromembranes when surface stress or pressure changes are applied on these transducers. In the last part of the chapter, it includes an analysis of the optical and morphological properties of diffraction gratings and photonic crystals.

Third chapter. – Development of mechanochromic materials. This chapter describes in detail the development of mechanochromic materials based on two types of photonic structures: linear gratings and colloidal assemblies. It includes a description of 1D linear polymeric grating preparation by master moulding and the optimisation of the methods to self-assembly polystyrene nanoparticles on substrates, maintaining the periodicity of the assembly and a close-packed configuration. This chapter also contains an in-depth study of the morphology of the assemblies, performed by scanning electron microscopy (SEM), with the aim to analyse their contribution in the material colouration (measured by UV-Visible spectrometry), looking to minimise the imperfections and ensuring uniformity in colouration. Finally, this chapter includes a brief description of the fabrication of coloured mechanical sensors (membranes and cantilevers) and a proof-of-concept of a wafer-scale fabrication of mechanical

sensors with mechanochromic response by using standard microtechnology processes.

Four chapter. – Opto-mechanical analysis of structural colour materials. In this chapter a deep study of the opto-mechanical response of the fabricated structured colour materials is performed, both under linear and bi-axial strain. Both UV-visible spectrometry and image analysis are used to that end. It also includes a general description of the fabrication of arrays of mechanochromic suspended membranes, necessary to carry out the bi-axial out-of-plane deformations.

Fifth chapter. – Colorimetric array of nanostructured membranes as a pressure sensor for optofluidics applications. This chapter describes the development of 2D nanostructured flexible array of membranes that tune their reflective colour depending on the pneumatic or fluidic pressure inside a microfluidic channel (pressure sensor). It describes the fabrication of elastomeric nanostructured membranes based in inverse 2D colloidal photonic crystals (colloidal diffraction grating). It also includes the study of morphology, mechanical properties and colour tuning of the fabricated membranes when exposed to bi-axial strains by applying pneumatic pressures. Finally, it includes a demonstration of the suitability of white light interrogation to measure the fluid pressure.

Sixth chapter. – Surface-stress colorimetric sensors based in cantilevers. This chapter contain a theoretical study of a surface stress colorimetric mechanical sensor based in microcantilevers and a demonstration of its performance for the detection of photo-induced molecular conformational changes. It describes the sensor, based in a diffraction grating designed into one microcantilever surface, with capabilities to produce a change in coloration under deformation. It describes also an analysis of the colorimetric method (capabilities and limitations) when the cantilever deflects by surface stress. In the same way, it includes the search of the optimum transducers parameters to maximize both the mechanical response and the colour change associated. In the final part of this chapter, the cantilever colour changes due to the surface stress produced by a thin layer of photosensitive molecules (azobenzene) disposed on the cantilever flat surface is demonstrated.

Seventh chapter. – Conclusions. This chapter summarize the results and conclusions of this PhD Thesis along with the perspectives and future related work.

Chapter 1: Introduction: MEMS – (Bio)Sensors

From the origins of life, the human being has needed to compare objects animals, food, or natural events such as seasons and temperature. To compare is a process inherent in the nature of human beings especially in the exploration and knowledge of the physical world. The result of this comparison was to be able to distinguish the differences between the properties of objects or events. Through the history, multiple ways of measuring were developed and with this, different definitions about what are to be measured. The fact of measuring the nature of objects and events has opened a broad range of possibilities for the development of new technologies. Measures as important as the determination of the speed of light in vacuum, or the heat transference in materials, among others, contributed to the determination of new magnitudes of measurement in multiple areas of science, engineering and health care.

Technologically, the need of measure led to the development of new devices called sensors allowing the transduction of a form of energy into another giving a new magnitude of measurement. Progress in technology development not only allowed the miniaturization of sensor devices, but also the improvement in sensitivity, performance, rapid response, less energy consumption, high specificity and low-cost manufacture.

This technology evolution began in 1947, with the development of the first computer and first transistor and has evolved to the nowadays mainboard of a smartphone, full of what we know today as microelectromechanical systems (MEMS). From the year 2000, due to the progress and integration experienced by the MEMS systems and the polymer technology for the manufacture of microfluidics, there was an explosion of the development of MEMS systems applied to medicine and health (BIOMEMS). The evolution of sensors devices applied to medicine and health resulted in higher miniaturization, an increase of biocompatibility and functionality, increase in accuracy and reduction of measurement and analysis time, finding numerous applications in this field. The technological developments in the health area have been focused on achieving automated analysis and diagnosis systems (lab-

on-a-chip systems, LOC, and point-of-care systems, POC) for the control and patient monitoring.

Healthcare is precisely one of the areas that have experienced a major impact from the development of sensors, leading to an evolution and transformation towards a decentralized medicine, which prioritizes the prevention of diseases by promoting an active and healthy life, an early detection to reduce the cost of treatments and management of chronic diseases. The development of new tools for early diagnosis and the study of the pathophysiology of diseases are key to continue to transform health care and reduce the costs associated with it.

The combination of BIOMEMS with what is known as the Internet of Things (IoT) allows carrying out a continuous monitoring of health, and a massive sending of continuously updated data to the cloud, where a processing and fusion of these data is carried out in order to perform an early and personalized evaluation, minimizing the risk to suffer certain diseases.
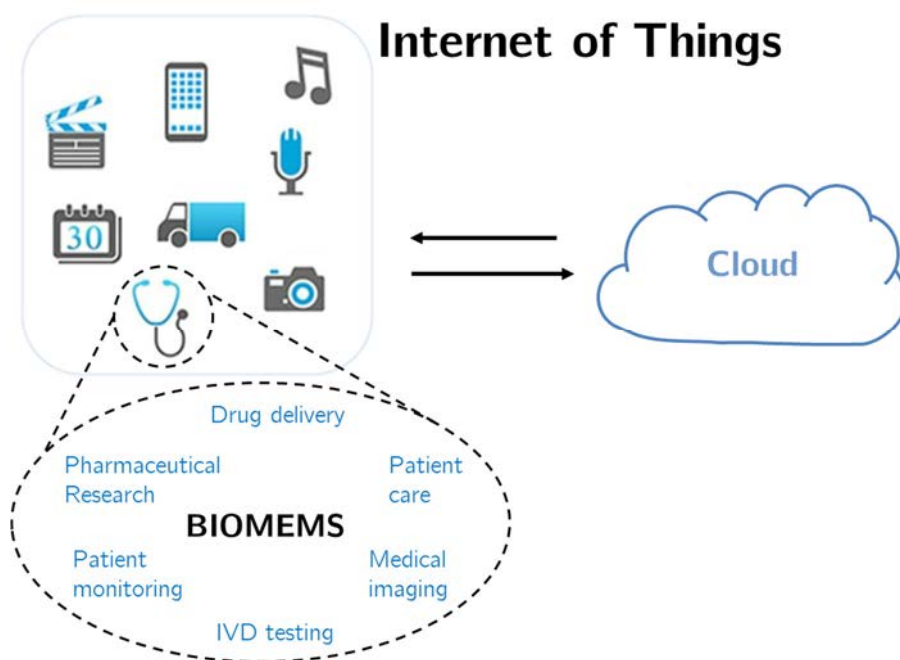
Figure 1.1 Internet of Things and BIOMEMS application areas.

The increase of the population, the increase of the life time, and the increase in the number of people affected by different types of diseases, such as

diabetes or cancer, make necessary the development of new technologies applied to the field of health in order to prevent and treat diseases, improve the quality of patient life, and reduce health costs. In this scope, it is necessary to decentralize the analysis and be able to carry out an early diagnosis at the point of care or even by the patient in any time and develop a precision medicine that reduces the use of ineffective treatments. Therefore, it is necessary to develop new tools based on POC technology that can be used at the medical consultancy and outside hospital environments [1], [2].

The POC devices have their origin in the microfluidic devices or systems originally called lab-on-a-chip (LOC) [3], [4]. These LOC devices arise thanks to advances in micro and nanotechnologies and allow carrying out within a single chip of small dimensions, conventional clinical, cellular and omics performed in large laboratories. These devices provide the aforementioned advantages of miniaturization and automation, increased accuracy and reduced measurement and analysis times, and have produced a revolution in the field of clinical diagnostics with the integration of sensing devices that allow detection in real time and at the point of care (POC)(**Figure 1.2**). POC devices include both the detection of vital signs, such as pulse, heart rate or oxygen saturation, and the biochemical detection of elements such as biomarkers, glucose, hormones, among others [2]–[5].

The variety of POC systems is very high, depending on the type of application. Thus, there are large systems that can be transportable, or portable systems, disposable, and more. In all of them, in addition to the sensor device (transducer) to perform the detection, it is necessary an electronic system that allows reading the signal emitted by the transducer and whose complexity will also depend on the type of application, and especially on the multidetection capacity [4], [6]. New generations of POC devices propose the use of technologies developed for smartphones to read transducers, thus avoiding the specific development of their own electronics [7]–[9]. More recently, POC devices have evolved into massive development of "wearables" devices, for monitoring vital signs, such as pulse, respiration or stress, or body markers that may be indicative of diseases, especially the final products of reactions such as glucose or lactate in easily accessible media such as sweat and tear (**Figure 1.2**, diagnostic) [10]–[14]. The main concept behind these platforms is the continuous monitoring of health, and the massive sending of

continuously updated data to the cloud, where processing and merging of the data is carried out in order to be able to perform an early and personalized assessment of the risk to suffer certain diseases (smart health) (**Figure 1.1**).
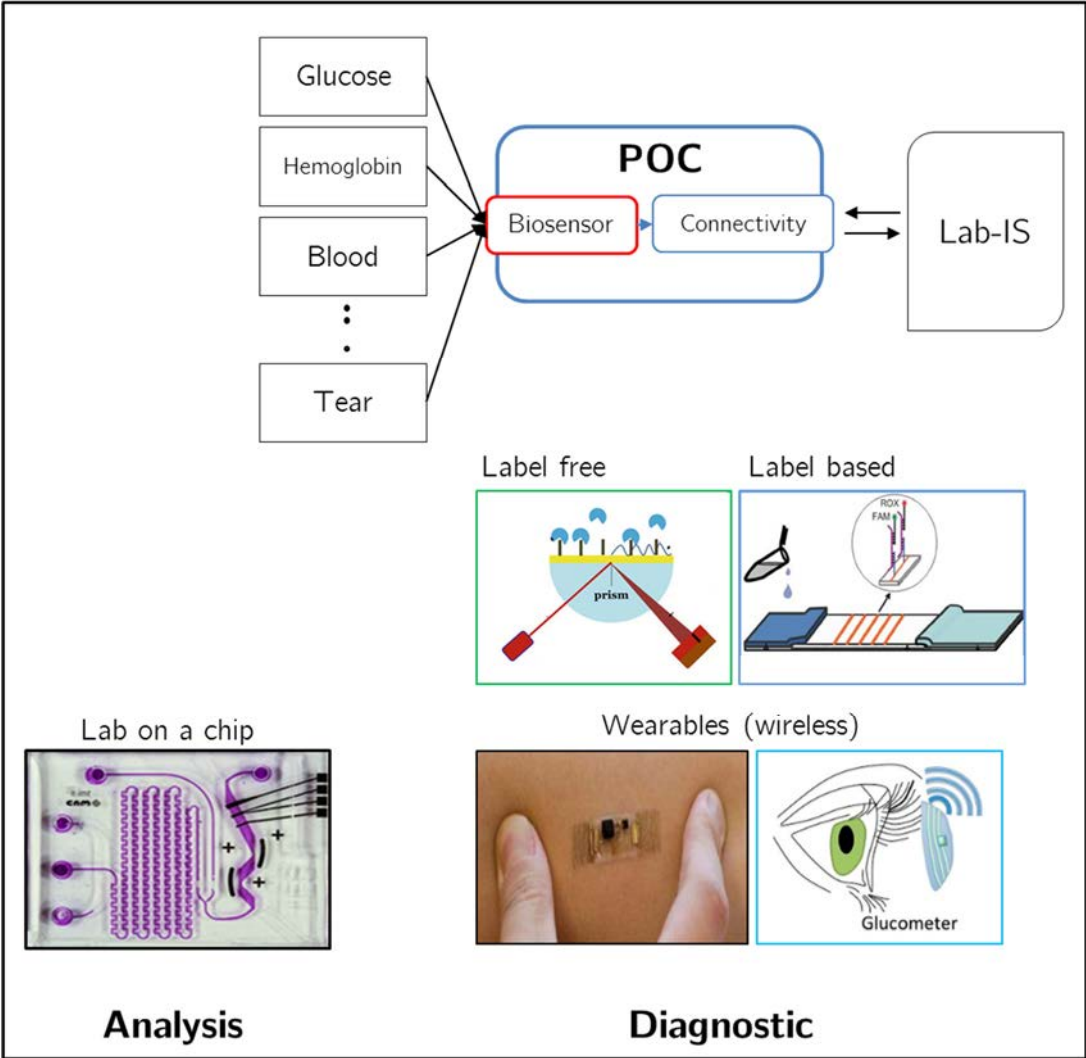
Figure 1.2 Technology for analysis and diagnostic. (**Analysis**) LOC, self-validating determination of biological analytes that undergo enzyme-catalyzed-reactions [15]. (**Diagnostic**) (Up) Schematic of a POC device, where the biosensors is the main component, and the connectivity with the laboratory information system. (Down) Label-based POC [16]. Label-free POC [17]. Wearable (wireless) POC [12], [14]

1.1 (Bio)Sensors

As previously mentioned, a device able to transform a form of energy into a measurable magnitude is called sensor. When this sensor is able to transform a biochemical interaction into a readable signal, it is known as biosensor. A

biosensor is therefore an analytical device, which integrates a transducer in direct contact with a biological layer specific to the analyte to be detected (antibodies, enzymes, aptamers, DNA, among others) (**Figure 1.3**), capable of transforming the biochemical interaction into a measurable response. In comparison with the current techniques of diagnosis and monitoring, done at central laboratories outside the hospitals, these integrated systems represent an ideal tool for the diagnosis of diseases, given their characteristics of rapid response, high sensitivity, analyte quantification capabilities, range of applications, low cost and easy use, without the need for large or expensive instrumentation.

Different types of sensors and biosensors have been developed, depending on the mechanism of transduction, having proven its viability in a wide range of applications (**Figure 1.3**). Lateral flow biosensors based on colorimetric markers, and electrochemical transducers, especially amperometric, are the most extended and commercialized devices, precisely due to their easy miniaturization and integration into POC devices. Another type of biosensors, are those based on optical transducers without markers, such as surface plasmon resonance (SPR), integrated optics or colloidal crystals, which have shown great sensitivity in very different fields. The commercialization of these systems has been achieved only at the research laboratories level, without reaching hospitals or patients, due to scalability drawbacks. Also, the piezoelectric and mechanical sensors have been broadly reported, being the last one the transducers that will be developed in this thesis. There are currently large companies involved in the development and commercialization of diagnostic devices in the clinical field (F. Hoffmann-La Roche Ltd., LifeScan Inc., Bayer Healthcare AG, Abbott Point of Care Inc., Medtronic or Siemens Healthcare, among others), being the blood glucose control sensors the most commercialized devices, covering the 85% of the total biosensor market, followed by of pregnancy tests (hCG) [18]. However, there are still many limitations to be resolved in order to achieve functional POC devices that can reach the market and solve social needs.
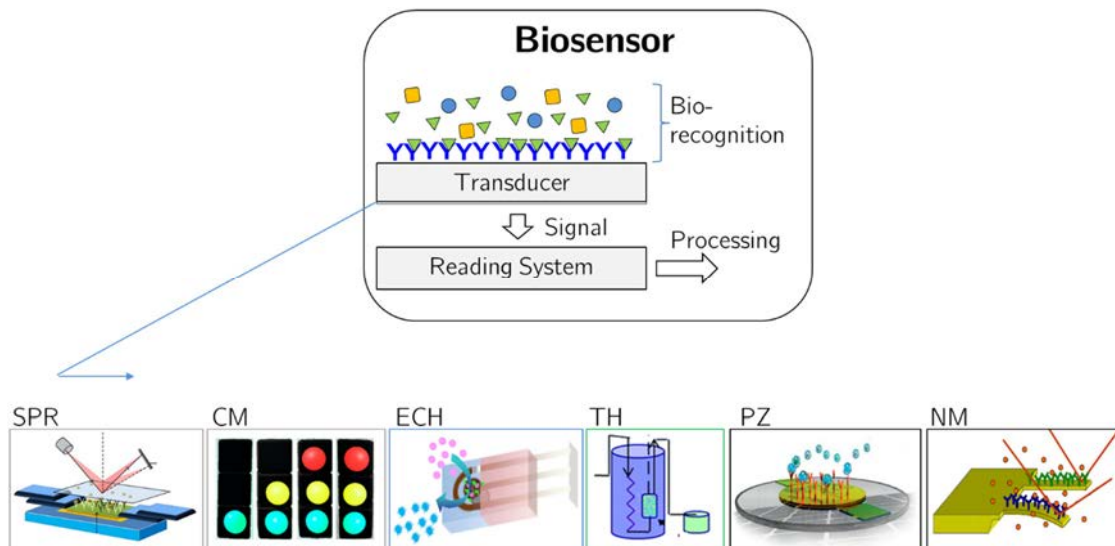
Figure 1.3 (Up) Schematic of a biosensor working principle, (Down, left to right) examples of biosensors generally classified by the transduction system, optical (Surface plasmon resonance (SPR) [19], (CM) colorimetric [20]), (ECH) electrochemical [21], [22], (TH) thermal [23], mechanical ((PZ) piezoelectric [24], and (NM) micro/nanomechanical [25]).

1.2 Micro/nanomechanical (bio)sensors

The advances in nanofabrication technologies have enabled the fabrication of increasingly smaller nanomechanical transducers capable of detecting the forces, motion, and mechanical properties that emerge in biomolecular interactions and fundamental biological processes.

Mechanical transducer can operate in static and dynamic mode. In dynamic mode its mechanical properties are determined mainly by their spring constant and resonance frequency (both parameters depend on the transducer material and geometry). In the static mode, the deflection arises as a consequence of a surface stress change induced by any process that takes places on only one of the transducer surfaces. Cantilevers are the most used structure, and can be fabricated in different shapes and thicknesses according to the detection propose or application (**Figure 1.4**). Cantilevers are mainly fabricated by silicon technology and only few applications have been reported using cantilevers based in polymeric materials, such as SU-8 or polyimide, and elastomers such as PDMS [26]–[29].

Many different applications have been developed based in the used of mechanical sensors in the static mode (surface stress). Detection of temperature changes, thin layer deposition, materials swelling, conformational changes or chemical and biochemical detection have been demonstrated with a very high sensitivity [30]–[32], in the range from $\sim 100\,pM$ to nanomolar. In a surface stress sensor, the magnitude or process to be detected occurs only in one surface of the sensor, inducing a mechanical deflection of the sensor as consequence of the difference on the surface stress generated in opposite surfaces. During the detection of the interaction of molecules or analytes (absorption or bio-recognition), small changes in surface tension are produced owed to many different forces: electrostatic repulsion, attraction, steric interactions, hydration, and entropy. Microcantilevers surface stress sensors have been used for detection and monitoring a wide variety of biomolecules, such as: tumor cells [33], [34], proteins [35], toxins [36], cholesterol [37], cancer cells [38], drug concentration [39], and conformational changes of enzymes [31].
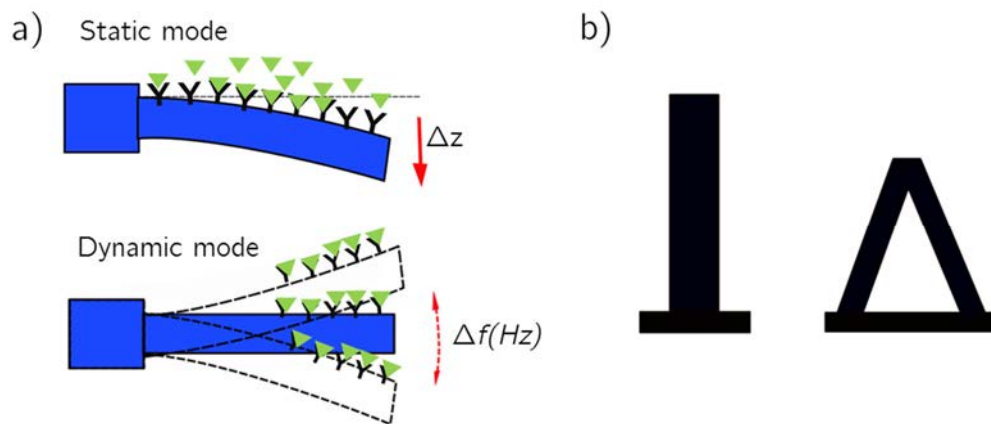
Figure 1.4 a) Microcantilevers working modes: static mode (deflection by surface stress) and dynamic mode (resonance). b) Microcantilevers common geometries (rectangular, V-shaped).

In a similar way than cantilevers, suspended membranes have been used for sensing and biosensing. A wide variety of sensors based in membranes has been reported for optofluidics applications commonly working by load deflection method [40]–[42]. For biosensing, static mode (surface stress) and dynamic mode are common working modes reported for detection and monitoring

biomolecules [43]–[46] (**Figure 1.5a**). In theory, membranes are less sensitive to surface stress variations than cantilevers under the same boundary conditions because they are peripherally supported [47]. Membranes have been fabricated using different ceramic materials (silicon, silicon nitride, or silicon oxide) [43], [48]–[50], polymeric materials such as SU-8, Poly(methyl methacrylate)(PMMA)), or Polydimethylsiloxane (PDMS). PMDS has been used to achieve higher sensitivity due to its low Young's modulus and for its high performance in terms of biocompatibility, and chemical inertness [51]–[53].

An advantage of the sensors based in membranes is the configuration of the sensing and detection layer, which can be in separated mediums as shown in **Figure 1.5**. With this configuration, the sensor improves the signal-to-noise ratio, and it's an ideal configuration for developing surface stress-based capacitive biosensors [44], [48]. Another way to improve the performance of the sensor has been reported using different membrane geometries (mostly circular and rectangular) [51], [54] (**Figure 1.5c**). Biosensor based in membranes have been used to measure the surface stress produced by DNA hybridization [48], [52], changes in deflections produced by thermal response of chemical reactions [44], and bacteria detection such as E. coli [53].
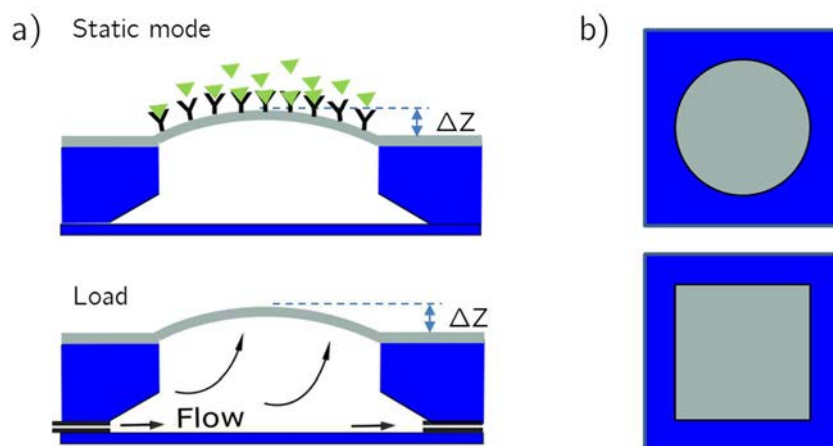
Figure 1.5 Membranes working modes: static mode (deflection by surface stress), and deflection by load, b) membranes common geometries (circular, and square).

1.2.1 **Detection Methods**

The small deflections produced by cantilevers and membranes are in the order of few nanometers for transducers based in silicon materials. Mechanical sensors with the transducers coated with different materials (metals and polymers) have been reported. Depending on the transducer material and dimensions, the coatings could increase the transducer Young's modulus reducing consequently the transducer displacements [53], [55]. In order to measure such small changes, different detection methods have been reported for membranes and cantilevers.

For **microcantilevers based sensors** the detection methods are designed according to different factors such as cantilevers operation mode, and integration with the sensor system. Most of applications based on nanomechanical microcantilevers report the use of an **optical** detection system. This method is highly sensitive and simple to implement (**Figure 1.6**, optics). Movements of the cantilevers free end are detected by measuring the reflected laser beam displacement into a position-sensitive photodetector (PSD) [56]. Other metrology techniques are based on diffraction and interference. Interferometry based in Michelson configuration (**Figure 1.6**, Interferometric) can achieve even higher sensitivities [57]. Interferometry techniques have been as well implemented using gratings or interdigital structures –fabricated into the microcantilever- and calculating the interference centroid position [58], [59]. More recently, Hermans et al. explored the use of laser diffraction effects for measuring the bending of nanomechanical sensors [60]. Many optical systems configurations have been proposed to measure more than a single cantilever at the same time (multiplexing light sources, scanning laser source, or using CCD camera) [61], [62]. However, most of the reported systems are based in the use of a single or few cantilevers, using a complex instrumentation or alignment systems, and are quite far of being portable [63]–[65].

Capacitive detection method has been as well demonstrated for the detection of gases and bio-interactions [66]. This method uses the cantilever as a conductor plate, separated by a dielectric from a second conductor plate. In this way, the capacitance between these two conductors varies with the deflections of one of them (cantilever) (**Figure 1.6**, Capacitive). The challenge of this method is the dielectric characteristics of the media (sample solution), conditioning the type of media in study [67], [62], [68], [69].

A detection system based in **piezoresistive** materials has been used in microcantilevers based sensors with high sensitivity. Most of these systems are fabricated in the same cantilever platform, enhancing the integration with microcantilevers systems (**Figure 1.6**, Piezoresistive). This method includes the detection by the measure of electric conductivity variations in piezoresistive materials produced when the cantilever is under bending. The major challenges of this method are the isolation of the piezoresistive materials from the media of study, and control of possible heat induction in cantilevers from piezoresistive materials. Small changes in the thermal conductivity led to parasitic cantilever deflections and piezoresistance changes [70]–[72], [62].

Piezoelectric materials have been used to fabricate microcantilevers or part of them allowing integrate the transducer and the read-out in the same system (**Figure 1.6**, Piezoelectric). The detection is performed by measures of the electric charge accumulated in piezoelectric material when it is under deflection. This system is commonly used in microcantilevers working in dynamic mode. There are some similitudes with the piezoresistive detection system due to high integration with arrays of cantilevers and challenges [73]–[75], [62].

Two-dimensional microcantilever arrays with geometrically configured metal-oxide semiconductor field-effect transistors (**MOSFETs**) have been used as an alternative detection method (**Figure 1.6**, MOSFET). The detection system is integrated into the base of the cantilever allowing the read-out in arrays of cantilevers. When the cantilever is under bending, the transistor drain current decreases. This high sensitive method presents low noise for a direct readout, being capable to detect cantilever deflections as small as $5\,nm$. In this method, the detection system is isolated from the media of study avoiding the direct contact [76]–[78].

The main problem associated with the used detection methods is the poor scalability of the optical components and the electronics required to work in an array configuration. A challenge still remains in the detection of several transducers simultaneously with a simple, portable and sensitive instrumentation. The development of new detection mechanism that fulfills these requirements will have a strong impact on the evolution of surface stress-based biosensors.
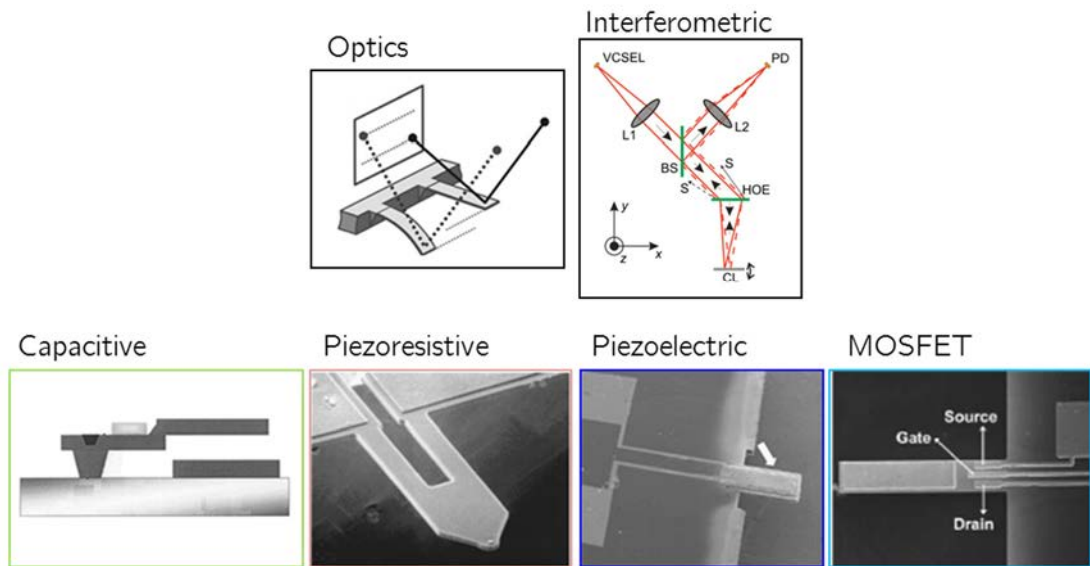
Figure 1.6 Common detection methods for microcantilevers based sensors. Optical [56]. Interferometric [57]. Capacitive [66]. Piezoresistive [62]. Piezoelectric [79]. MOSFETs [76], [80].

For mechanical sensors based on **membranes** working under load deflection, optical detection methods are commonly used [41], [81], [82]. Optical techniques based on the use of **confocal microscopy** or **interferometry** has been reported to measure the small changes of membranes when these are working in load deflection and static mode (surface stress) [83], [84]. The simplest method reported is the use of a **camera** laterally placed to measure the membrane profile while it is under deformation [85]. Other approaches are based on the deformation of embedded optical microstructures (e.g. diffraction gratings) [86], [87] and the optical detection of the diffraction pattern change after deformation [88], [89]. In a similar way than cantilevers, **piezoresistive** [45] and **piezoelectric** [24], [46], [90] systems have been used to measure the small deflection of membranes produced by surface stress changes (**Figure 1.8**). Other sensors use the small variations in **capacitance** produced when the membrane deflects by surface stress [44], [48], [51].
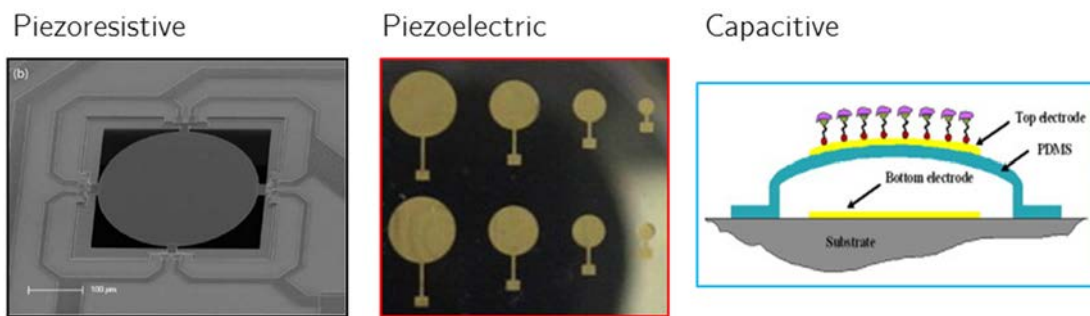
Figure 1.7 Common detection methods for mechanical sensors based on membranes. Piezoresistive [45]. Piezoelectric [46]. Capacitive [51].

1.3 Visual sensors: colorimetric detection

The colorimetric detection represents a simple and powerful detection mechanism, especially suitable for the development of low-cost and simple to use sensors and POC devices with a multisensing capability. Colorimetric sensors provide visual or optically detectable readout signals, arising from the distinct colour changes of the materials which serve as the key active element of the sensors [91], [92]. The optical readout can be easily read by a camera and even naked eyes and further analyzed for quantitatively evaluation of the signal, providing user-friendly monitoring of health and environment.

Based on the sensing materials and mechanisms of colour generation, colorimetric sensors can be generally classified into chromophore- and dye-based, plasmonic nanoparticle-based, and structural colour-based sensors [91], [93]. Structural coloration originates from the interaction of the light with micro and nano-structures via interference, diffraction or scattering. In contrast to chromophore and dyes, structural coloration does not have additional energy consumption, and is more cost-effective than plasmonic nanoparticles.

Structural coloration is a widespread phenomenon in natural creatures, which has served as inspiration for the development of new label-free colour sensors and smart stimuli-responsive materials [94]–[98]. In general, these sensors combine the creation of photonic structures and the employment of responsive materials which change their volume upon exposure to analytes [92] or external stimulus (temperature, humidity, mechanical) [99], [100], changing their photonic structure. The colour response is especially sensitive to changes in the material structure, which makes them very interesting materials able to

convert external mechanical stimulus into observable changes of the material colour (**mechanochromic**) [101]–[104].

Different type of structures has been used to produce changes in colour such as photonic crystals, diffraction gratings or high-contrast meta-structures (HCMs) (**Figure 1.8**). Different techniques have been proposed for the fabrication of flexible mechanochromic photonic materials for monitoring mechanical deformations [105]. One of the simplest and most extended methods to achieve periodically structured polymeric materials is by using 2D and 3D colloidal assemblies (bottom-up approach), known as colloidal photonic crystals (CPhC, **Figure 1.8a**). These materials are particularly interesting for the development of visual deformation sensors, including materials swelling or strain [106]–[108]. Elastomeric materials, such as silicone rubber, have been used by several groups to detect mechanical stimulus [107], [108]. Other approaches are based on top-down processes for the fabrication of the flexible structural colored systems, including **diffraction gratings** (**Figure 1.8b,** D-gratings) or photonic crystal slab supporting guided modes resonance (GMR). High refractive index materials are usually required to enhance the diffracted colour or support the propagation of resonance modes, which present serious limitations when using metal or semiconductor layers due to the cracking of this layer during the deformation [109], [110]. As an alternative, Karrock *et al.* [111] reported the fabrication of flexible photonic membranes with quasi-guided modes resonances formed by a refractive index layer of TiO_2 nanoparticles on a periodically nanostructured surface. With this approach, an estimated limit of detection of $160\,Pa$ was reported by colour imaging of the membrane. **HCMs** made of one single-layer (high-refractive-index material fully surrounded by low-index material) and periodicity of nearly one wavelength have been as well used for the detection of strain. By using flexible HCM with enhanced -1st diffraction order, Zhu *et al.* reported a large colour change with small deformation [112] (**Figure 1.8c,** HCM).
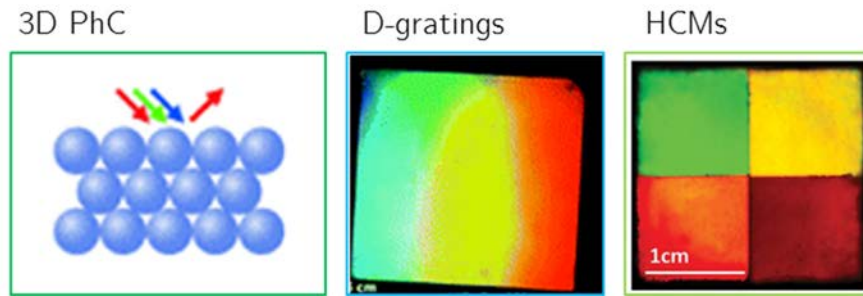
Figure 1.8 Colour materials based on colloidal photonic crystals [105], diffraction gratings [105], HCMs [112].

1.4 Array of structural coloured mechanical sensors: mechanochromic response

As a novelty and alternative to the complex detection systems normally used to measure the mechanical response, a new approach based on opto-mechanical sensors with colorimetric reading of deflection is proposed in this Thesis. The developed sensors arise from the combination of suspended mechanical structures and structural coloration based on diffraction gratings and photonic crystals. The developed colorimetric detection (without labels), represents a simple and powerful detection mechanism, especially suitable for the development of low-cost sensors and POC devices, since it does not require extra energy consumption or complex instrumentation beyond an LED and a RGB camera, being possible to make a reading with the naked eye or with an smartphone.

The structural coloration of the mechanical sensors is achieved using diffraction gratings and colloidal photonic crystals manufactured in the sensors surface. The diffraction of the white light upon striking these surfaces gives the systems a specific colour depending on the surface corrugation periodicity and the light interaction angle. When the deflection of the sensor occurs, during the sensing processes, a variation in the spacing between corrugations and a change in the light interaction angle occur, giving rise to a colour gradient along the transducer (mechanochromic response). The photonic crystals are obtained from a bottom-up process, through the self-assembly of polymeric nanoparticles with adequate size to work in the visible range. The optical responses of the mechanical devices (membranes and cantilevers) manufactured with these

materials are analysed by UV-Visible spectroscopy and by mean of a camera and colour analysis from images.

The opto-mechanical devices therefore consist of a suspended polymer structure, where one of its surfaces will contain the photonic nanostructures providing the system a variable coloration depending on the deformation, while the other surface is functionalized with a specific sensing layer for the specific application under development, which can be biological, polymeric or plasmonic metamaterials. The use of metamaterials and polymers capable of selectively absorbing the radiation and producing a change in the structure of the material are also possible action mechanisms of devices.
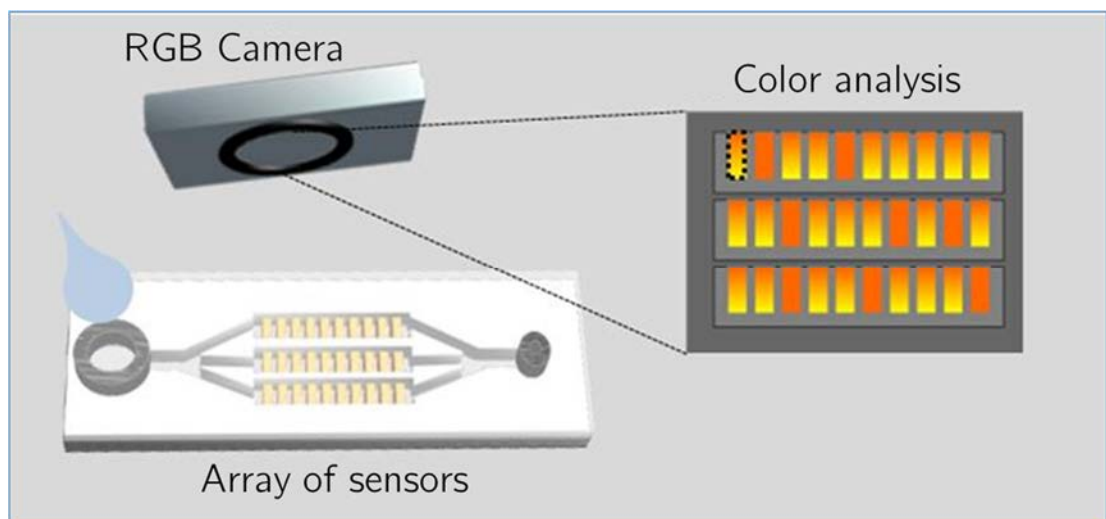
Figure 1.9 Schematic of the proposed POC device based in an array of structural coloured mechanical sensors.

Chapter 2: Physics of mechanical transducers and structural coloration

2.1 Introduction

Mechanical sensors sensitivity depends on shape, size, and material properties. Therefore, a deep study of the physics involved in the deflection of transducers is required for an optimum design. Mathematical models used to simulate the deflection of a cantilever are based in a beam exposed to a uniform or local free-end forces [113]–[115]. This approach has been used in the design of many sensors and biosensors based on cantilevers [116], [117]. In membrane-based sensors, the maximum deflection of the system has been approximated to the shape of a half-parabola considering a uniform deformation when it is fixed to its contour. In these both types of transducers, the sensitivity is characterized by the detection of small changes in surface stress or mechanical loads.

In other hand, structural coloration refers to the colour exhibited by a material caused by the interaction of white light with micro- and nano-structures [118]. Structural coloration can be produced by film interference, diffraction gratings, scattering and photonic crystals [118]–[121]. By tailoring the structures at the nanoscale, photonic materials could be constructed with specific optical properties and functions. The applications of structural colour materials range from decoration, painting, displays, light wave guiding units for photonic communication and in optoelectronic devices, or sensors in anti-counterfeiting and chemical/biomedical analysis. Optical readings based in colour or intensity variations are especially interesting to provide an intuitive and quantitative method for non-invasive multiplexed and wireless detection, by using a simple instrumentation.

The effective combination of mechanical sensors and materials with structural coloration offers new possibilities and challenges for the development of mechanical sensors with colorimetric response. In this sense, the intention of this chapter is to introduce the physics and mathematical models that describe

the working principle of our device. The general mechanical behaviour of microcantilevers and micromembranes is initially described when surface stress or pressure changes are applied on these transducers. In the last part of this chapter, the optical and morphological properties of diffraction gratings and photonic crystals are analysed.

2.2 Mechanics of microcantilevers in static-mode

Sensors based in mechanical microcantilevers that operate in static mode take advantage of the bending moment in response to local stress. In general, local surface stress is a result of materials thermal expansion after a temperature or phase change, changes in the volume of the coating (swelling), or intermolecular interactions on the sensor surface. The local surface stress generated on one of its surfaces results in the bending of the sensor (**Figure 2.1**), being possible to detect conformational changes or biorecognition events with extremely high sensitivity by monitoring the sensor displacement. Many different coatings have been used to produce surface stress induced bending's, such as: thin films of metallic and polymeric materials, self-assembled monolayers (SAM) of organic molecules, or biological agents between others. Surface stress origin is due to the covalent bonding of surface atoms and the added coating atoms or linker molecules, intermolecular forces between absorbed molecules (van der Waals, steric hindrance, hydrogen bonding or electrostatic), configurational entropy or change of electronic charge density, etc. (**Figure 2.1**).
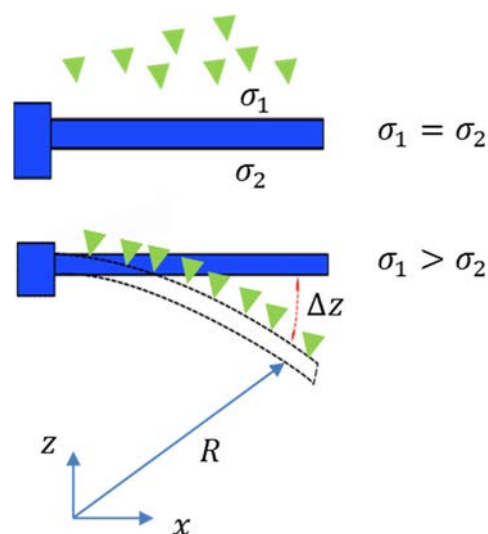
Figure 2.1 Schematic of a microcantilever sensor working under static mode (surface stress change).

2.2.1 Surface stress and surface tension

Surface stress is defined as the reversible work per unit area needed to stretch a solid elastically, causing an increase in its surface (first defined by Gibbs [122]). This implies the variation of the distance between the atoms of the surface. In this case, only the distance between them is modified, remaining constant the number of atoms on the surface [123]. The *surface tension* can be represented as the summation of atoms forces on a surface of a solid over the volume of it. Surface tension is the mechanical work per area of formation of the surface in a reversible process and at a constant number density n of atoms at the surface. This action of transferring atoms from one area to another occurs in plastic deformations or in the deformation of fluids, where atoms have greater freedom of movement [124].

The most extended definition was proposed by Shuttleworth [125], relating the surface stress, γ, with the total surface free energy of Helmholtz H per unit of area A.

$$\gamma = F + A\frac{\partial F}{\partial A} \tag{2.1}$$

where $F = H/A$, for a one component liquid, where surface free energy and tension are equal.

In plastic deformations, the molecules move to adapt to the new situation, changing the number of molecules on the surface and keeping the area per molecule. For solids is necessary to include the energy associated with the elastic deformations, where the surface is created by stretching of an existing surface remaining constant the number of molecules in this surface. Due to the difference in the physical nature of the plastic and elastic deformation, two different concepts are also defined in the thermodynamics of surfaces: Gibbs free energy, γ, and surface tension. According to Shuttleworth,

the tension tensor, σ_{ij}, for an infinitesimal deformation is expressed as [122], [125]:

$$\sigma_{ij} = \frac{1}{A} \frac{\partial(\gamma A)}{\partial \varepsilon_{ij}} = \gamma \delta_{ij} + \frac{\partial \gamma}{\partial \varepsilon_{ij}} \qquad (2.2)$$

where A is surface area, γ the Gibbs free energy per unit area of deformed surface, δ_{ij} the Kronecker's delta, and ε_{ij} the deformation tensor. In the case of solids, the second term of the equation (2.2) responds to the change of energy by deforming the surface in certain directions, positive (tensile) or negative (compressive), in consequence, the surface tension of a solid can be both positive and negative. The sign of the surface tension means that there is a decrease or an increase in the area of the modified surface. In the case of solids where the length and width are much greater than their thickness, the increase or decrease of the area of one of their surfaces produces a deformation in the solid with a constant radius of curvature R. In this way, the surface stress induced in a cantilever can be calculated with high precision by experimentally measuring the cantilever displacements.

2.2.2 Stoney equation

In microcantilevers working in static mode, the deflection produced by molecular recognition in one face of the cantilever is equivalent to the deflection produced by a thin film deposited in this face. Measurements of the curvature radius of the cantilever allow obtaining information about the surface stress change produced by the thin film. Experimentally G. G. Stoney [126] demonstrated the relationship of the curvature radius of a plate with the external tension applied by a thin metallic film deposited in one face of the plate. The Stoney expression (equation (2.3)) is [126].

$$\text{Pt} = \frac{Eh^2}{6R} \qquad (2.3)$$

where P is the tensile force per unit cross section of deposited film (normal tension), t, the thickness of the thin film, h the thickness of the plate, and R the curvature radius of the plate. The equation (2.3) is redefined to include the

biaxial state of the stress, where for cantilevers with $h \gg t$ the apparent Young's modulus is $\hat{E} = E/(1 - v^2)$, where v is the Poisson coefficient [127].

The change of surface stress applied is equivalent to load the cantilever free end with a moment $M = bh\Delta\sigma/2$, where $\Delta\sigma$ is the difference of stress between the surfaces (**Figure 2.1a**), $\Delta\sigma = \sigma_1 - \sigma_2$, and b the cantilever width. Combining the equation (2.3) with the Euler-Bernoulli equation [128], the commonly used Stoney's equation is obtained (equation (2.4)). This equation relates the curvature radius with the external surface stress applied to the cantilever.

$$\frac{1}{R} = \frac{6(1 - v)}{Eh^2}\Delta\sigma \tag{2.4}$$

The Stoney's equation is broadly used for mechanical sensors analysis considering some assumptions [122].

- Both the film thickness t and substrate thickness h are uniform, and the film and substrate have the same radius R, and $t \ll h \ll R$.
- Both the film and substrate are homogeneous, isotropic, and linearly elastic.
- The film stress states are in-plane isotropic or equal on both axes while the out-of-plane direct stress and all shear stresses vanish.
- The system's curvature components are equal on both axes while the twist curvature vanishes in all directions.
- All the stress and curvature components are spatially constant over the plate system's surface; and the strains and rotations of the plate system are infinitesimal.

One of the restrictions of the Stoney's equation is the application only in the "thin-film approximation", that is, for coatings films much thinner than the substrate $\delta = t/h \leq 0,1$, being needed a correction factor $(1 + \gamma\delta^3)/(1 + \delta)$, where γ is the quotient of biaxial module [129].

On the other hand, the Stoney's equation is obtained for free plates, while the sensors based in cantilevers are fixed in one end. The fixation effect in the cantilever deflection increase as the relation L/b decrease. The Stoney's

equation is valid for $L/b > 1$. For $L/b \rightarrow \infty$, the fixation effect is negligible. Many authors have studied the effect of the cantilever fixation in conditions where $L/b >> 1$ for V shape cantilevers [113] and rectangular cantilevers [130].

2.2.3 Relationship between deflection and surface stress

Focusing on the use of cantilevers that deflects by the action of surface stress, an expression that relates the surface stress and deflection is needed.

From the geometrical parameters showed in the **Figure 2.2a,b**, for a small cantilever deflection and circular deformation, the relation between the curvature radio R and the curvature angle θ_c is expressed by the equation (2.5):

$$\theta_c = \frac{L}{R} \tag{2.5}$$

where the suffix c is the extreme point of the cantilever free end (normal to R) (**Figure 2.2b**). Replacing R in the equation (2.4), the Stoney's equation in function of the curvature angle can be written as:

$$\Delta\sigma = \frac{Eh^2}{6L(1-v)}\theta_c \tag{2.6}$$

In order to determine the relationship between the deflection angle and the vertical displacement of the cantilever free end (Δz), the slope for each point x along the cantilever is calculated by the expression (2.7) considering a circular deformation (**Figure 2.2b**):

$$\tan\theta = \frac{du_z(x)}{dx} \approx -\frac{x}{\sqrt{R^2 - x^2}} \tag{2.7}$$

For a curvature radio R larger than microcantilever length, $R \gg L$, and integrating the equation (2.7) for $x = L$, the curvature radius is expressed as $R = L^2/2\Delta z$. Replacing this new R expression in the equation (2.5), the relation between the cantilever displacement and its angle is expressed as:

$$\theta_c = \frac{2\Delta z}{L} \tag{2.8}$$

Thus, replacing the equation (2.8) in the Stoney's equation (2.6), the relation between the cantilever deflection and the surface stress that produces it is expressed as follow:

$$\Delta\sigma \approx \frac{Eh^2}{3L^2(1-v)}\Delta z \tag{2.9}$$
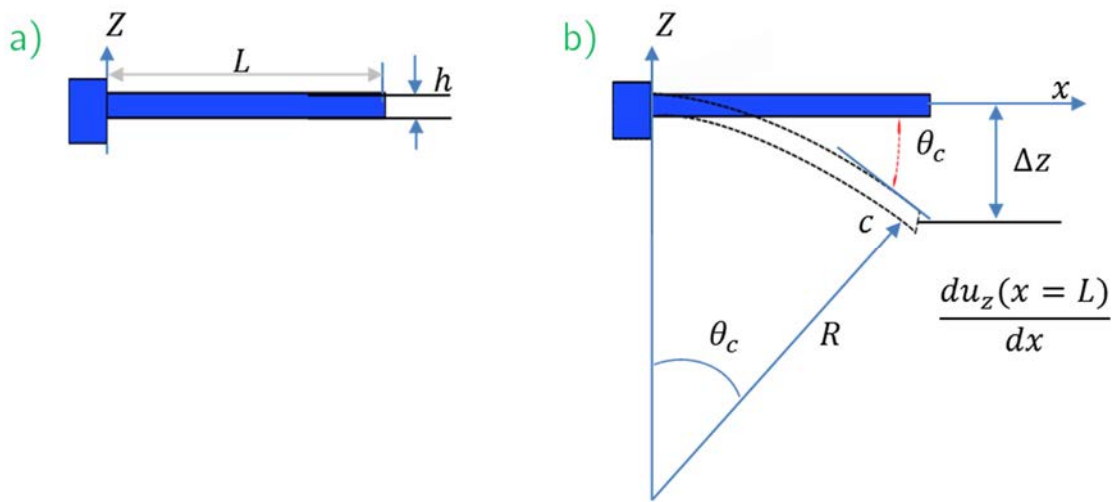
Figure 2.2 a) Geometrical parameters for a microcantilever. b) Microcantilever under deflection with curvature radius R and L<<R.

2.3   Mechanics of membranes

After microcantilevers based sensors, membranes systems are another configuration of sensitive mechanical transducers used for detecting small changes by surface stress and under load deformation. A circular membrane system is constituted for a film that is fixed or clamped at circular rim. The mechanical analysis of a membrane system under load deformation (bulge test) provides an essential tool to improve the sensitivity of sensors.

2.3.1 Bulge test

This technique is carried out to investigate the behaviour of a material film subjected to tensile stresses in biaxial directions [131]–[133]. The test is performed by clamping or fixed a membrane around its rim and subjecting it to a pressure on one side, hence producing a deflection of the system (**Figure 2.3**). While the membrane is under deformation, the maximum deflection can be measured in the central region of the membrane. Bulge test is widely used because of its simple design and fast implementation [85], [134]–[138]. This test provides valuable mechanical information about the material of study.
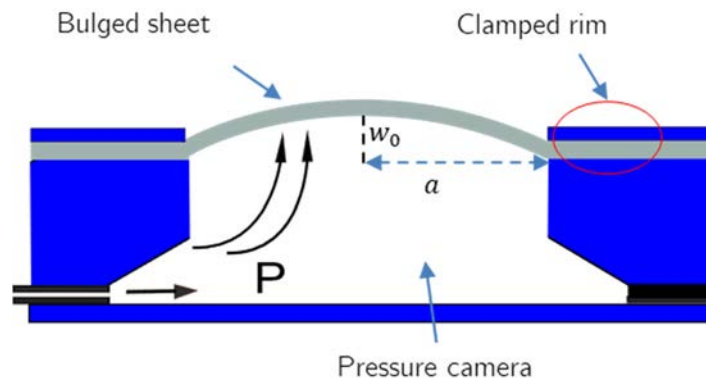
Figure 2.3 Bulge testing configuration for a membrane with its parameters: radius, a, deformation, w_0, and uniform load, P.

The bulge test is commonly used to determine the residual stress, σ_0, and the biaxial Young's modulus $Y = E/(1 - v)$ on square or circular membranes [139]. Different analytical technics have been reported to convert pressure displacement values into stress-strain results [132]. The relation of the uniformly applied load, P, and the maximum deflection at the centre of the membrane, w_0, produced on a circular film can be represented by the equation (2.10) [140]:

$$P = \frac{16t^3E}{3(1 - v^2)a^4}w_0 + 4\frac{t\sigma_0}{a^2}w_0 + 2.43\frac{Et}{(1 - v^2)a^4}w_0^3 \tag{2.10}$$

where t is the thickness of the sample, v is the Poisson's ratio, E is the Young's modules and a is the radio of the membrane. The three terms in

equation (2.10) describe the contribution of the bending moments, residual stress, σ_0, and stress due to straining of the neutral fibre, respectively. Bending moments and residual stress show a linear interrelationship between pressure change and membrane deflection, while the stress due to straining contributes with its third power. This membrane behaviour suggests that for detecting low pressure changes, in a low pressure range, the governing parameter is given for the change in the curvature of the membrane, discarding the effect of the neutral fibre strain (no change in the thickness of the membrane).

For multilayer membrane, the biaxial modulus and residual stress of the structure can be calculated as the summation of the thicknesses and modulus for each layer of the structure as shown in equation (2.11) [133], [139]:

$$M_{multilayer} = \left(\frac{t_1}{t_{total}}\right) M_1 + \frac{t_2}{t_{total}} M_2 + \cdots + \left(\frac{t_n}{t_{total}}\right) M_n \qquad (2.11)$$

where $M_{multilayer}$ is either biaxial modulus or residual stress of the structure, $t_{1,2,3\ldots n}$ are the thicknesses of each layer, and $M_{1,2,3\ldots n}$ are the biaxial modulus or residual stress for each layer.

2.3.2 Bulge test models and strains

The models commonly used to analyse the mechanical properties of membranes are derived from the shape of the membrane. Some models for spherical cap geometry have been developed to calculate stress and strain in bulged films.

2.3.2.1 Solution for an initially flat and unstressed film

For a spherical cap geometry membrane (**Figure 2.4**), the stress in the film is derived from the condition of force equilibrium and represented by the equation (2.12).

$$\sigma = \frac{PR}{2t} \qquad (2.12)$$

where t is the thickness of the film, P the applied pressure, σ represents the film in stress, and R the curvature radius, which is the same in both the radial and circumferential directions [133] .
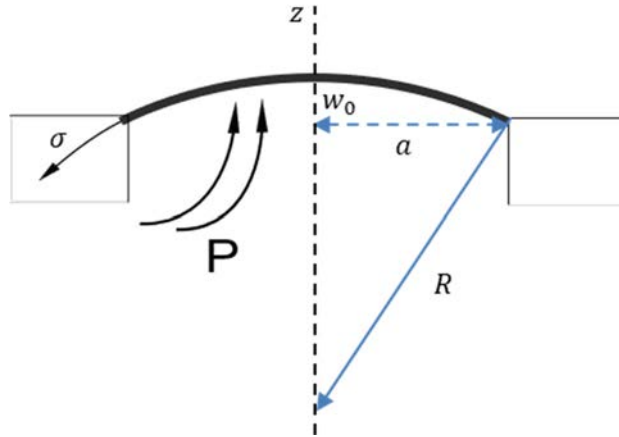
Figure 2.4 Spherical cap geometry.

From equation (2.12), the stress σ and strain ε are expressed in terms of the deformation height w_0, when it is much less than the film radius a (equation (2.13) and (2.14)). The strain is defined as the change in arc length divided by the unstressed film length [133].

$$\sigma = \frac{Pa^2}{4w_0 t} \tag{2.13}$$

$$\varepsilon = \frac{2w_0{}^2}{3a^2} \tag{2.14}$$

Combining the equations (2.13) and (2.14), the pressure-displacement relation predicted for an elastic material is expressed by equation (2.15)

$$P = \frac{8Yt}{3a^2} w_0{}^3 \tag{2.15}$$

The total strain can be written as the sum of the strain due to the residual tension stress in the film, σ_0, and the strain due to the applied pressure $\varepsilon = \varepsilon_{bulge} + \varepsilon_0$, resulting the equation (2.16).

$$\varepsilon = \frac{2{w_0}^2}{3a^2} + \frac{\sigma_0}{Y} \tag{2.16}$$

2.3.2.2 Energy minimization method

For the shape of the membrane (**Figure 2.5**), the energy minimization method is a common approach to approximate the deformation behaviour of a thin film in a bulge test. The most commonly used method is that given by Timoshenko [131]. In this method, the shape of the deformed body is assumed and the load-deflection behaviour is calculated by minimizing the strain energy of the system with respect to constants in the shape function. The method is given for large displacements of rectangular plates under uniform normal loads. From this method, two solutions are derived for the applicability for circular films [128], [131].

The **first solution** is derived by assuming that the shape of the deformed film could be approximated as that of a clamped **circular plate** under normal loading (**Figure 2.5a**). A plate is defined by small centre deflection w_0 at $r = 0$ (bulge height), compared with its thickness t. For a constant load, the deflection is in function of the distance r from the centre. This approximation is represented by the equation (2.17) [131], [132].

$$w(r) = w_0 \left[1 - \left(\frac{r}{a}\right)^2\right]^2 \tag{2.17}$$

where a is the radius of the film. Applying the energy minimization method for a plate shape film, the relation pressure-displacement result as follow:

$$P = \frac{16Yt^3}{3a^4(1+v)} w_0 \left(1 + 0{,}488\frac{{w_0}^2}{t^2}\right) \tag{2.18}$$

In the **second solution**, the shape was defined as a circular arc using the approximation that the bulge height is much less than the film radius (also called **thin membrane**) [131], [132] (**Figure 2.5b**). In this solution the bending moments are small, and the deflection is a function of the intrinsic stress and the elastic straining of the film.

$$w(r) = w_0 \left[1 - \left(\frac{r}{a} \right)^2 \right] \tag{2.19}$$

Applying the energy minimization method for a circular arc shape (thin membrane), the relation pressure-displacement result as follow:

$$P = \frac{Y(7-v)t}{3a^4} {w_0}^3 \tag{2.20}$$

For both solutions, the radial displacement is represented by equation (2.21), where C_1 and C_2 are arbitrary constants.

$$u = r(a-r)(C_1 + C_2 r) \tag{2.21}$$
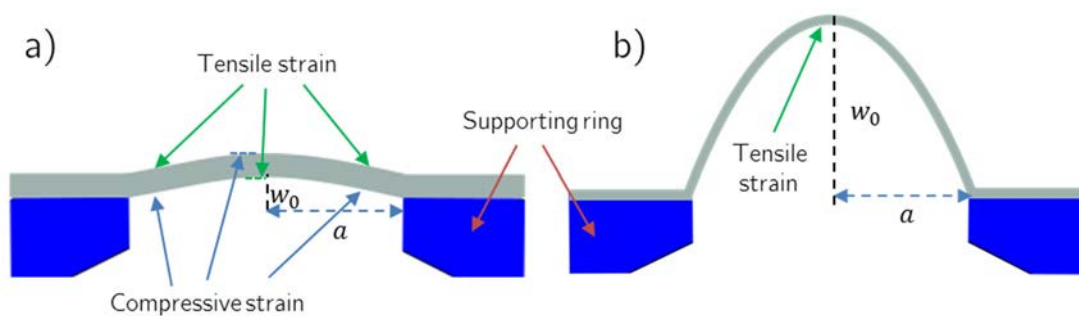
Figure 2.5 a) Thick diagram, b) Thin membrane.

2.3.2.3 Stress and strain distribution

For **plates** (**Figure 2.5a** and equation (2.17)), the major forces acting against this deflection are the bending moments of the plate. In this way, when the plate is deflected by a pressure difference P, the areas with tensile and compressive strain respectively develop on its surface in the radial direction. The sign of strain is opposite on opposite sides of the plate as shown in **Figure 2.5a**. The distribution of the stress on the surface of the plate in radial, σ_r, and tangential, σ_t, direction is represented by the equations (2.22)and (2.23) [131], [140], [141].

$$\sigma_r = \frac{3}{8}\frac{P}{t^2}(a^2(1+v) - r^2(3+v)) \tag{2.22}$$

$$\sigma_t = \frac{3}{8}\frac{P}{t^2}(a^2(1+v) - r^2(1+3v)) \tag{2.23}$$

From the stress distribution equations (2.22) and (2.23), the strain in radial, ε_r, and tangential, ε_t, direction on the surface of the plate are calculated as follow:

$$\varepsilon_r = \frac{\sigma_r}{E} - v\frac{\sigma_t}{E} \tag{2.24}$$

$$\varepsilon_t = \frac{\sigma_t}{E} - v\frac{\sigma_r}{E} \tag{2.25}$$

where E and v are the Young's modulus and Poisson's ratio of the plate respectively. Combining the stress equations (2.22) and (2.23) with the strain equations (2.24) and (2.25), the strain distribution on the surface of a plate can be calculated as follow.

$$\varepsilon_r = \frac{3}{8}\frac{P}{Et^2}(a^2(1-v) - 3r^2(1+v^2)) \tag{2.26}$$

$$\varepsilon_t = \frac{3}{8}\frac{P}{Et^2}(1-v^2)(a^2 - r^2) \tag{2.27}$$

For **thin membranes**, the bending moments are negligible, the stress on both sides of the membrane and tensile strain on the entire membrane are nearly the same. The stress is approximated to be constant over the entire membrane. In the centre of the membrane, the radial and tangential stress and strain are the same. However, there is no tangential strain at the rim, where the membrane is fixed. For a constant radial strain, ε_r, over the entire membrane, the tangential strain can be estimated from the difference between the length of the diameter $2a$ of an undeflected membrane and the segment of the circular arc with a centre deflection of w_0 [131], [140], [141].

$$\varepsilon_r = \frac{2}{3}\frac{w_0^2}{a^2} \tag{2.28}$$

$$\varepsilon_t = \varepsilon_r \left(1 - \frac{r^2}{a^2}\right) = \frac{2}{3}\frac{w_0^2}{a^2}\left(1 - \frac{r^2}{a^2}\right) \tag{2.29}$$

The tangential strain, ε_t, is assumed to drop quadratically from the centre of the membrane to its rim, as shown in **Figure 2.5b**.

2.4   Structural coloration

Structural colour originates from the physical interaction of micro- and nano-structures with light. By defining sophisticated nanoscale architectures, the propagation of light could be well controlled. Light within a certain range of wavelengths shows high reflectivity and is perceived by the human eye due to selective spectral sensitivities of photoreceptors in the retina. The coloration is given by the interaction of light with various types of spatial inhomogeneity. Thus, fundamental optical processes such as reflection, refraction, interference, diffraction and scattering can become sources of structural colour. In this way, the mechanisms of structural colour can be categorized into different optical phenomena such as thin-film interference, multilayer interference, diffraction grating and photonic crystals. Most of structural colours present in nature use mechanisms to enhance the coloration by combining the structural colour and iridescence (also known as goniochromism) [95], [97]. The iridescence appears in a restricted sense when the colour apparently changes with the angle of view or when the angle of illumination changes. Thin-film interference, diffraction gratings and photonic crystals are basic mechanism of iridescence [142]. The range of colours of natural iridescent objects can be narrow, for example shifting between two or three colours as the viewing angle changes, or cover a wide range of colours [94], [95], [143].

In this section, the optical and morphological properties of two mechanisms of structural coloration are analysed: diffraction gratings and photonic crystals.

2.4.1 Optical properties of diffraction gratings

Diffraction gratings are optical structures with high importance in the spectral analysis of light. These components consist of periodical corrugations along the surface (grating). The diffraction is produced when light is incident on the grating surface and it is diffracted from the grooves (**Figure 2.6a**). The light diffracted by each groove combines to form a set of diffracted wavefronts (**Figure 2.6c**). The usefulness of a grating depends on the fact that there exists a unique set of discrete angles along which, for a given spacing d between grooves (also called pitch), the diffracted light from each angle is in phase with the light diffracted from any other angle, leading to constructive interference [144]. For all other angles there will be destructive interference between the wavelets originated at successive grooves. Thereby each groove becomes a small source of reflected/transmitted light (**Figure 2.6ab)**.
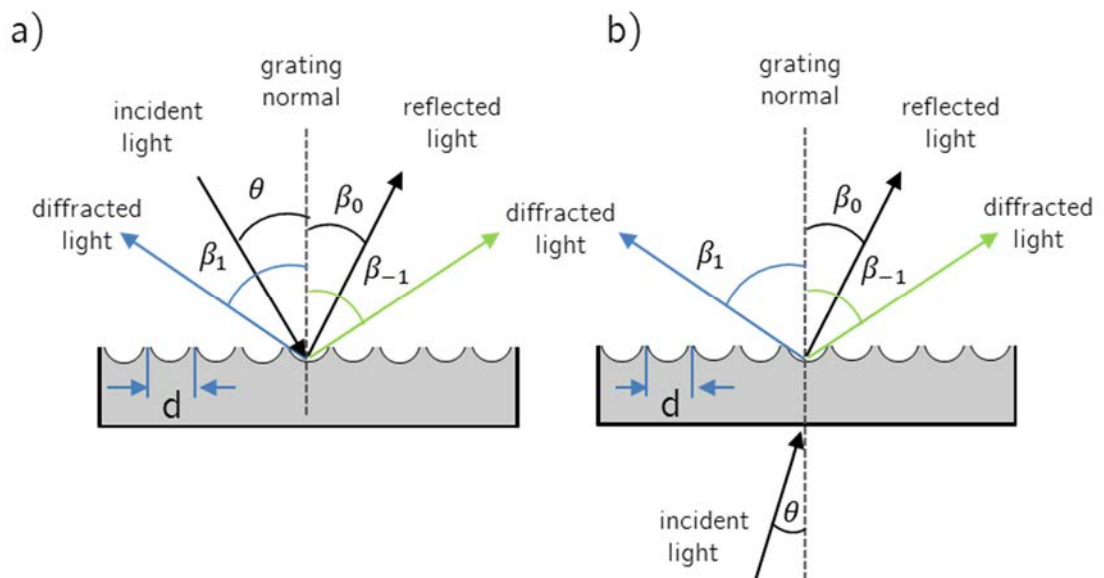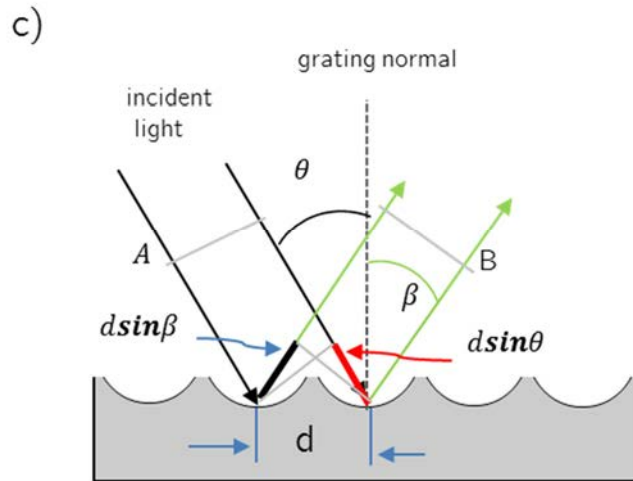
Figure 2.6 a) Reflection. b) Transmission. c) Geometry of diffraction for planar wavefronts.

The geometrical path difference between light from adjacent grooves is expressed by $d\big(sen(\theta) + sen(\beta)\big)$, where $dsen(\beta)$ is negative for $\beta < 0$. In this way, the main property of gratings to diffract incident light is expressed by the **grating equation** (2.30).

$$m\lambda = d\big(sen(\theta) + sen(\beta)\big) \tag{2.30}$$

where θ is the incident angle, β is the diffracted angle, d is the grating period, m is the diffraction order $(m = 0, \pm1, \pm2, \pm3, \dots)$, and λ is the wavelength (**Figure 2.6**). All values of m for which $|m\lambda/d| < 2$ correspond to diffraction orders. In the case where $m = 0$, leads to the law of reflection $\beta = -\theta$ (specular reflection).

2.4.1.1 Diffraction orders

Diffraction orders represent the integer values of m that satisfy the grating equation. For a period d, wavelength λ, and incident angle θ, the grating equation satisfy more than one diffraction angle β. The order number represents the number of wavelengths between light reflected from successive grooves; assuming a monochromatic and ideally collimated incident light. For $\lambda/d \ll 1$, exist large number of diffracted orders. The distinction between

positive and negative orders is identified for, $\beta > -\theta$ positive orders $(m > 0)$, with $\beta < -\theta$ negative orders $(m < 0)$, and for the specular reflection when $\beta = -\theta$, in consequence $(m = 0)$ [144], [145]. The sign convention is represented in **Figure 2.7ab**.

For non-collimated and non-monochromatic light, the linear diffraction can be represented as a superposition diffraction of all its plane-wave components, as shown in **Figure 2.7d**, where the wavelength diffracted in the first order overlap the next order wavelengths. The superposition of wavelengths would lead ambiguous diffraction data, thus adding troubles to distinguish between light of different wavelengths incident on it.
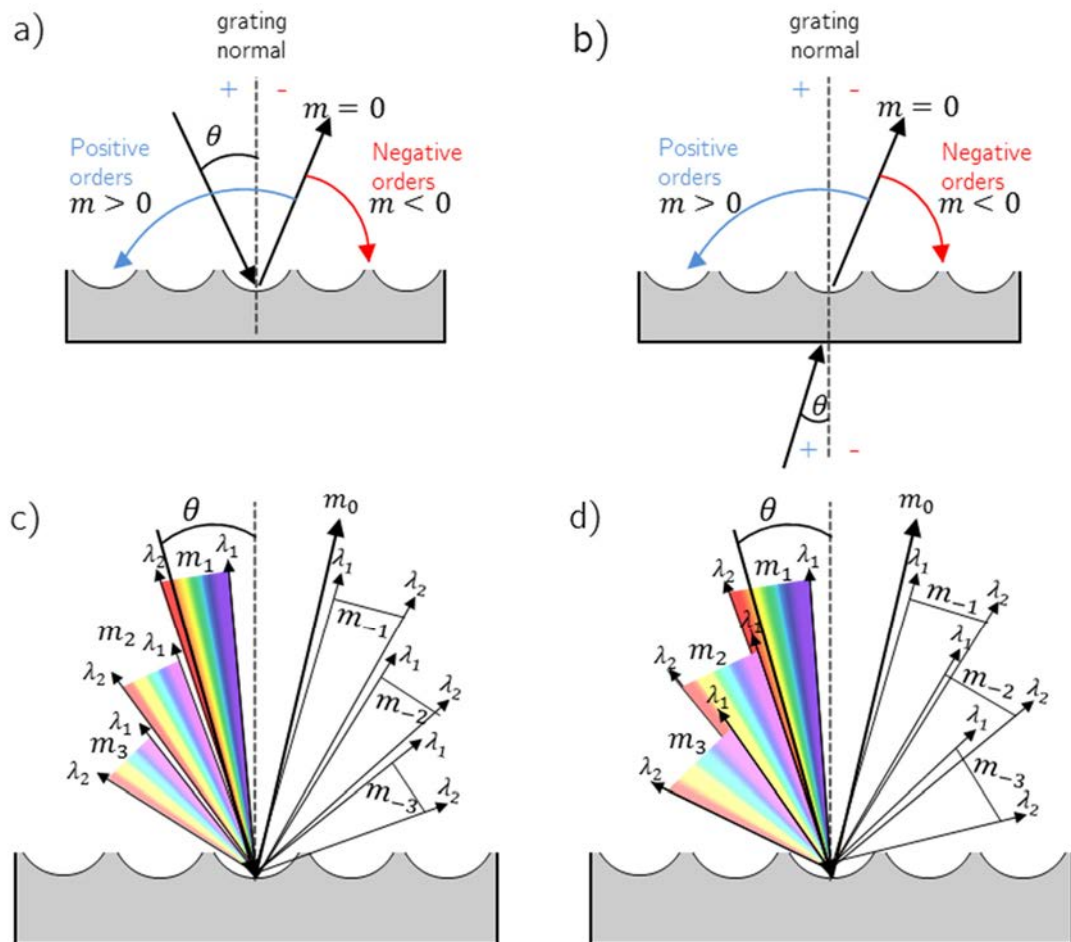
Figure 2.7 Diffraction orders representation by sign, for positive and negative order m for a) reflection and b) transmission. c) Free spectral range, no overlapping between diffraction orders occur. d) Superposition of diffraction orders, a small part of m_2 order is overlapping the first order m_1, and m_2 with m_3 for an incident angle θ. Similar case for negative orders.

When superposition of diffraction orders does not occur as shown in **Figure 2.7c**, the range of wavelengths is called free spectral range (FSR). Here, the range of wavelengths $\Delta\lambda = (\lambda_{2,m+1} - \lambda_{1,m})$ for which the m_{th} of the wavelength λ_2 coincides with the $(m + 1)_{st}$ order of wavelength λ_1 [144]. In this case, the grating equation satisfies each wavelength for each diffraction order m.

2.4.1.2 Resolution

The grating resolution R is defined as the ability to separate adjacent spectral lines of average wavelength λ. It is represented by the dimensionless expression, $R = \lambda/\Delta\lambda$, where $\Delta\lambda$ is limit of resolution (the minimum difference between two wavelengths that can be resolved unambiguously). Using the Rayleigh criterion, the separation R between the primary maximum from neighbouring minimum is represented by $R = |m|M$, where m is the diffraction order, and M is the number of the illuminated groves. A meaningful representation of R is derived from the main diffraction equation (2.30) as [144]:

$$R = \frac{M}{\lambda}\left(sen(\theta) + sen(\beta)\right) \tag{2.31}$$

The maximum resolution of a grating is represented by $R = 2A/\lambda$, where 2 is the maximum value of the angular part (Littrow configuration).

2.4.1.3 Littrow configuration

Littrow configuration is called to specific reflection configuration where incident angle θ and the diffracted angle β have the same sign respect to the normal. This configuration refers to a specific geometry for blazed gratings at which the grating efficiency is maximum. Since $\theta = \beta = \theta_L$, for $m > 0$, the expression derived from the main diffraction equation (2.30) is given by:

$$m\lambda = 2dsen(\theta_L) \tag{2.32}$$

where θ_L (Littrow configuration angle) is dependent of the first order m_1, the wavelength λ, and the pitch d of the grating. For triangular gratings, the θ_L is the same of γ grating angle $\theta_L = \gamma$ (**Figure 2.8**).
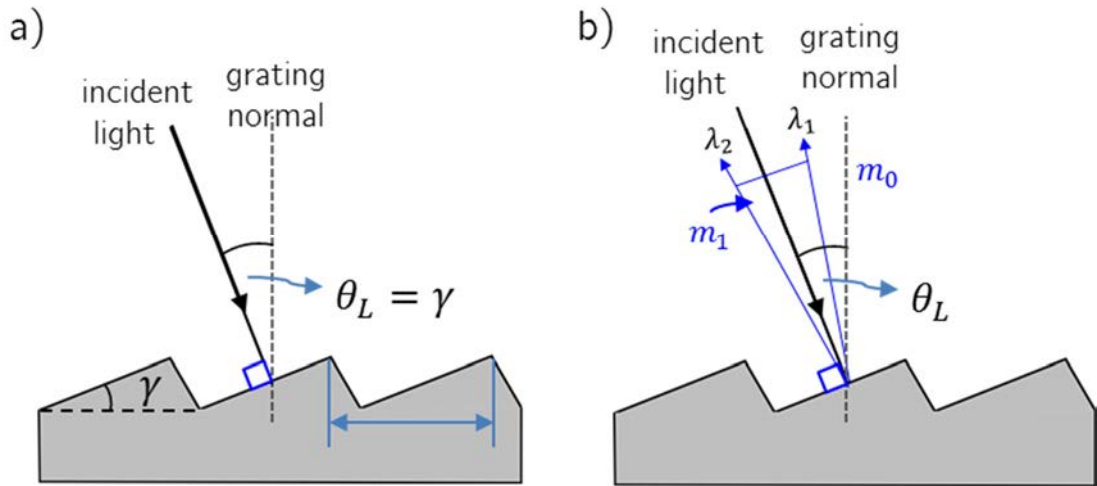
Figure 2.8 Littrow configuration for a triangular grating a) $\theta_L = \gamma$, and d dependence b) First order dependence.

In this configuration, the wavelength is dependent of the angular separation, where it increases as the diffracted order increases for light of normal incidence (for $\theta_L = 0$, θ_m increase as m increases). Using this configuration, the efficiency decreases at higher orders decreasing the FSR (defined as $\Delta\lambda_{FSR} = \lambda/m$).

2.4.1.4 Types of diffraction gratings

There is a wide variety of diffraction gratings commercially available, classified by the grating shape, groove shape, working mode (transmission, reflection), coating material, and more. The general classification for classical **linear diffraction gratings** (1D periodicity) is based in two main groups: holographic and ruled diffraction gratings. The **ruled gratings** generally have a triangular shape. The main characteristic of these gratings is the high efficiency produced in Littrow configuration (**Figure 2.8**) due to the triangular shape of grooves. This kind of gratings operate at a specific wavelength given by the

grating angle γ (**Figure 2.9a**). The **holographic gratings** are mainly identified by their sinusoidal shape of grooves (**Figure 2.9b**). The principal characteristic of these gratings is the minimum capacity for scatter light, giving it good performance in sensitive measurements. These gratings are designed specially to reduce or eliminate periodic errors, such as ghosting. The main drawback of these gratings is the reduced efficiency compared to ruled gratings.
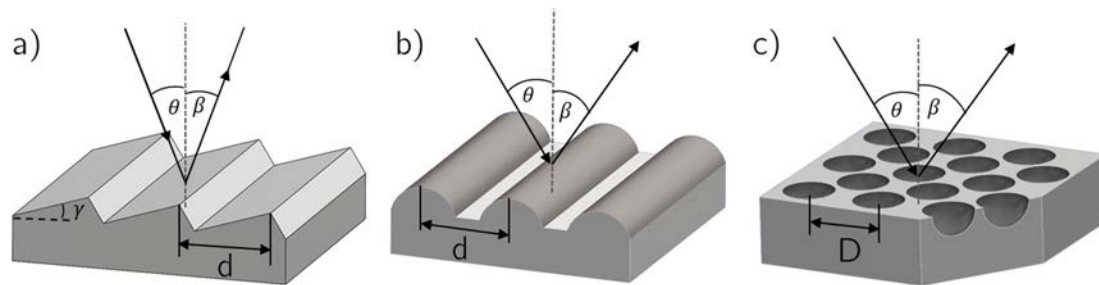
Figure 2.9 a) Ruled grating. b) Holographic grating. c) Two dimensional grating (bi-axial).

In another classification of diffraction gratings are the gratings that are nanostructured in **two dimensional** conformations (2D periodicity). The main characteristic of these gratings is the biaxial diffraction for a given incident angle θ (**Figure 2.9c**) and distance d.

Linear gratings have the same sensitivity than 2D ones, but these present a dependence on the azimuthal angle being more critical the alignment of the light and the grating surface [146]. In the case of 2D, the diffraction depends only of the polar angle due to the grating biaxial orientation.

2.4.2 Photonic crystals

Photonic crystals (PhC's) are defined as graded-index periodic optical structures, which can be defined as any non-absorbing medium which is invariant under the translations of a crystal lattice [96]. Photonic crystals possess a photonic bandgap (PBG) which does not allow the propagation of light with certain wavelengths in certain directions (a band of frequencies in which light propagation in the photonic crystal is forbidden). The origin of the

photonic bandgap is this periodic variation of refractive indexes. The position of the bandgap is determined by the lattice constant and the spectra PBG width by the effective refractive index contrast and filling factor. If materials of sufficiently high refractive index contrast are used in conjunction with materials with low absorption in the desired spectral range, then light with energies located inside the PBG will be reflected from the PhC without absorption [147]. When the PBG is located into visible light range, the PhC can exhibit bright and vivid colours, known as structural colours. PhC's may be regarded as a special case of composite, built from two materials with refractive indices η_1 and η_2. The structural coloration of PhC's can be produced by periodic structures in one dimension (1D), two dimensions (2D), and three dimensions (3D).

One-dimension photonic crystals (1D-PhC's) are structured for a pair of layers with different refractive indices (η) placed in periodical order such a film stack (**Figure 2.10a**). This stack is also called Bragg mirror. For 1D-PhC's considering two layers with η_1 and η_2, and thickness d_1 and d_2, for $\eta_1 > \eta_2$, constructive interference occurs when.

$$2(\eta_1 d_1 \cos\theta_1 + \eta_2 d_2 \cos\theta_2) = m\lambda \tag{2.33}$$

where m is a positive number.

In **two-dimensional photonic crystals** (2D-PhC's) (**Figure 2.10b**), the incident light diffracted can be calculated from the planar grating equation. There are several discrete angles, α, for a given groove spacing, d, where constructive interference occurs between diffracted light,

$$m\lambda = d(sen(\alpha) + sen(\beta)) \tag{2.34}$$

where D is the sphere diameter, α is the angle of incidence, β the angle of diffraction, and d, in the case of a monolayer of colloids, corresponds to $d = \sqrt{3}D/2$ for a hexagonal close-packaging.

For **three dimensional photonic crystals** (3D-PhC's), the colour also depends on the refractive index, tilting angle and distance between the cubic close packing (ccp) (111) planes. The reflected wavelength is expressed by a

combination of the Bragg's law (optical diffraction) with Snell's law (refraction of light between media of dissimilar refractive index)[148].

$$m\lambda = 2d_{111}\sqrt{\eta_{eff}^2 - \sin^2\theta} \qquad (2.35)$$

where λ is the free space wavelength of the incident light, m is a positive integer, d_{111} is the distance between the ccp(111) planes, η_{eff} is the average refractive index and θ is the angle of incidence (**Figure 2.10c**). The colour of the 3D-PhC can be changed by controlling these three parameters (d_{111}, η_{eff} and θ).

For 3D-PhC's based in colloidal structure, the material coloration is produced by the constructive interference of the beam reflected from the different layers. The equation (2.35) expresses the modification of Bragg-Snell's law. Where the effective refractive index of the media, η_{eff}, depends on the relative refractive indices of the spheres and surrounding medium. For this case η_{eff} is calculated by.

$$\eta_{eff} = \sqrt{\eta^2{}_p f_p + \eta^2{}_m(1 - f_p)} \qquad (2.36)$$

Where η_m and η_p are the refractive index of the medium and colloids, respectively, and f_p is the volume fraction of colloids, which for a close packed system is $f_p = 0.74$.
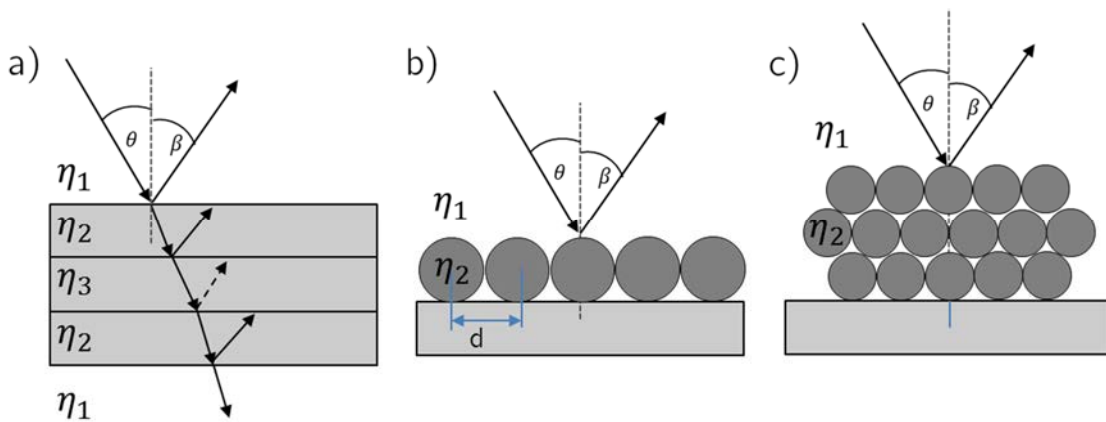
Figure 2.10 Photonic crystals structures: a)1D, b) 2D, c) 3D

Chapter 3: Development of mechanochromic materials: structural coloration

3.1 Introduction

From the early studies in structural colouration of nature, a wide compendium of studies has contributed to the development of materials that mimic the natural colouration [93], [95], [96], [149], [150]. Advances in nanofabrication have promoted the development of structured coloured materials with specific nanostructure size, and shape, with the aim of producing colours on a wide spectral range. Structural colour materials have been fabricated by using top-down processing techniques, such as lithography, and bottom-up methods including controlled self-assembly. Diffraction gratings used currently are usually fabricated with solid materials based on silicon or similar. Other varieties even use polymeric materials with high stiffness, such as thermoplastics [144], [145].

Crystalline colloidal assemblies in two- and three-dimensions (3D) have demonstrated to be a powerful tool for many technological applications such as functional coatings, photonics, plasmonics, solar cells, and strain sensors. These techniques are also attractive due to the low-cost of the materials, simple processing, and excellent control to self-assemble large areas of colloidal nanoparticles, demonstrating the potentiality of fabrication in numerous hierarchical and periodic nanostructure array patterns [151], [152]. Colloidal micro- and nanoparticles of polystyrene (Ps) and silica (SiO_2) have been widely used to fabricate two-dimensional $2D$ assembled monolayers or $3D$ stacks, due to their uniform morphology and good dispersion stability [51]– [55]. These properties have been extensively used in different fabrication methods, including air- and oil-liquid interfaces, drop casting, dispersion, rolling, and other related techniques to create a periodic multilayer or layer-by-layer assemblies [151], [152], [158].

In this chapter, I describe step-by-step the fabrication processes followed for the development of polymeric mechanochromic materials based on two

types of photonic structures: linear gratings and colloidal assemblies. Three essential variables are manipulated to exploit the white light interference and colour tuning: changes in grating period, changes in nanoparticle size, and changes in the angle of interaction of the light. 1D linear polymeric grating was easily prepared by master moulding, by using commercially available gratings. In the case of 2D colloidal structures, I performed an optimisation of the methods to self-assembly polystyrene nanoparticles on substrates, maintaining the periodicity of the assembly and a close-packed configuration. An in-depth study of the morphology of the assemblies was done to analyse their contribution in the material colouration, looking to minimise the imperfections and ensuring uniformity in colouration. The optical responses of the polymeric photonic materials were measured by UV-Visible spectrometry, while their morphology was examined by scanning electron microscopy (SEM). Finally, this chapter includes a brief description of the fabrication of coloured mechanical sensors (membranes and cantilevers) and a proof-of-concept of a wafer-scale fabrication of mechanical sensors with mechanochromic response by using standard microtechnology processes.

3.2   1D linear grating: Replications

For the fabrication of transducers with a periodical structure in one face, a classical method for replication was employed, by using commercial lineal gratings as a master mould. The first step was to manufacture a replica of the commercial grating to be used as a master facilitating the manipulation, machining, cutting or bonding without damaging the original grating (**Figure 3.1**). For this purpose, a **600** grooves/mm diffraction grating was used to reproduce a PDMS replica. In this process, the grating surface was coated with 1H,1H,2H,2H-perfluorooctyl-trichlorosilane (PFTS) silane by gas phase protocol in order to facilitate the PDMS peel-off. A mixture of PDMS-cross-linker (10:2 ratio) was pureed on the grating surface. After the elimination of the bubbles for **20** minutes in a vacuum chamber, the mix was cured for **1** hour at $80\,^oC$ in an oven. The cured PDMS was peeled-off from the grating and immediately bonded to a glass substrate by oxygen plasma achieving a new PDMS master. The surface of the PDMS master was coated by PFTS silane to facilitate the replication. This PDMS master was used to replicate the grating in different materials such as polyimide, SU-8, and PDMS.
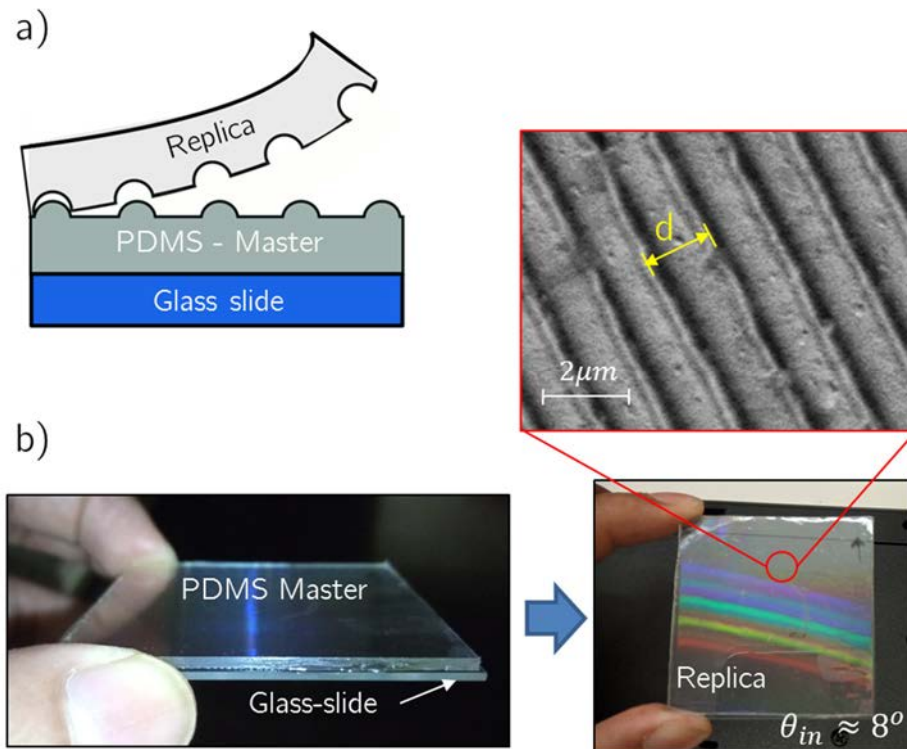
Figure 3.1 a) Schematic replication process. b) PDMS master and its replication illuminated at 8°, and (up) SEM image of the replication surface, $d = 1666\ nm$.

The diffracted colour of the 1D photonic materials was measured by UV-Visible spectrometry (Flame spectrometer from Ocean Optics) and a bundle reflection probe (that emit white light from a central fibre and collect the back-diffracted light with the surrounding set of six fibres), in a Littrow configuration with a spot diameter of about $500\ \mu m$. The experimental angle between the probe and the normal to the membrane was $10^{\,o}$. According to the diffraction equation for Littrow configuration $\Delta\lambda = 2d\text{sen}(\theta_L)$ (described in section 2.4.1.3), there are two parameters that acts as principal contributors to produce changes in diffraction wavelengths, the parameter d and the parameter θ_L. In order to demonstrate this angle dependence in 1D diffraction gratings, a basic setup based on a UV-Visible spectrometer and a reflection bundle fibre in Littrow configuration was implemented (**Figure 3.2a**).

A reflectance spectrum was obtained by measuring the colour change produced when focusing on a 1D replicated on PDMS film by changing the angle of incidence of the bundle reflection probe. A sequential colour change

was found, as shown in **Figure 3.2b**. For higher angles, $\theta_L > 16^o$ a second peak in the lower band ($400 nm$) was captured, that correspond with second diffraction order. The reflectance amplitude decrease as increase the incident angle due to the change of diffraction order.
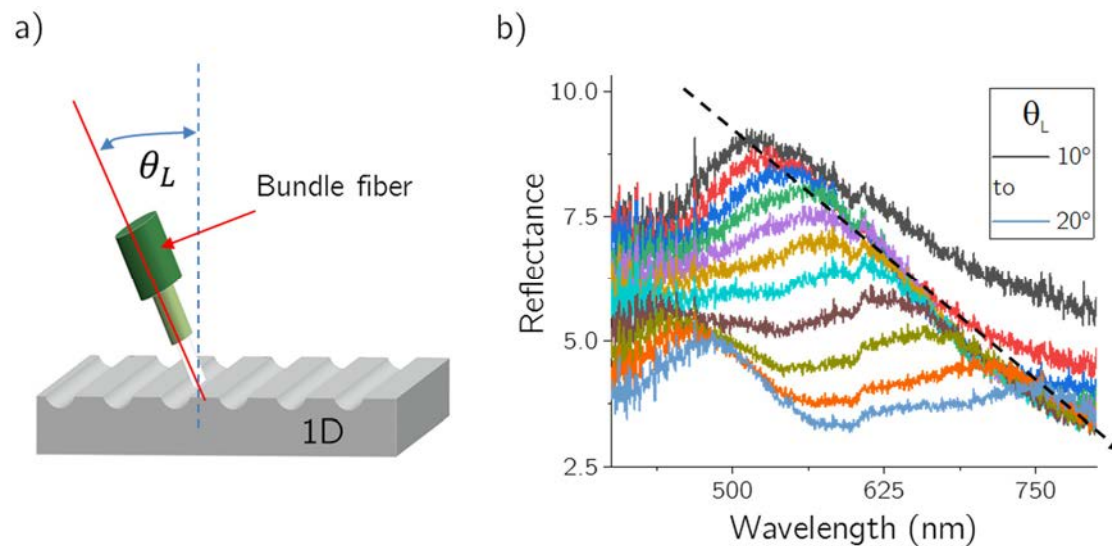
Figure 3.2 1D reflectance at different angles: a) bundle fibre configuration at θ_L respect the normal and, b) reflectance spectra for θ_L from 10° to 20°.

3.3 Photonic materials based on colloidal assemblies

3.3.1 3D photonic crystals

The **3D-PhC's** were obtained by drop casting, by controlling the drying temperature, and the ratio between volume released and the particles concentration in solution for a desired drop size. The particle concentration was chosen to obtain only few layers of ordered PS nanoparticles, to avoid the "leachy" effect. The 3D photonic materials were prepared by using polystyrene (PS) nanoparticles of $300 nm$ diameter embedded in PDMS. First, drops of $5 \mu l$, and $1.25 wt\%$ nanoparticles solution were released over a glass slide creating an array of drops and evaporated during 3 minutes at $95 \,^oC$ in an oven with the attempt to reduce the coffee ring formation (**Figure 3.3a**). Third, a thin layer of PDMS ($17 \mu m$) was spin coated over the dried 3D-PhC, and leaved 15 minutes at room temperature to achieve a fully infiltration, and then

cured at $100\,^oC$ for 30 minutes in an oven. The crystal structure was checked by scanning electron microscopy (SEM). As shown in **Figure 3.3b** high ordered close-packed was achieved for the 3D-PhC.
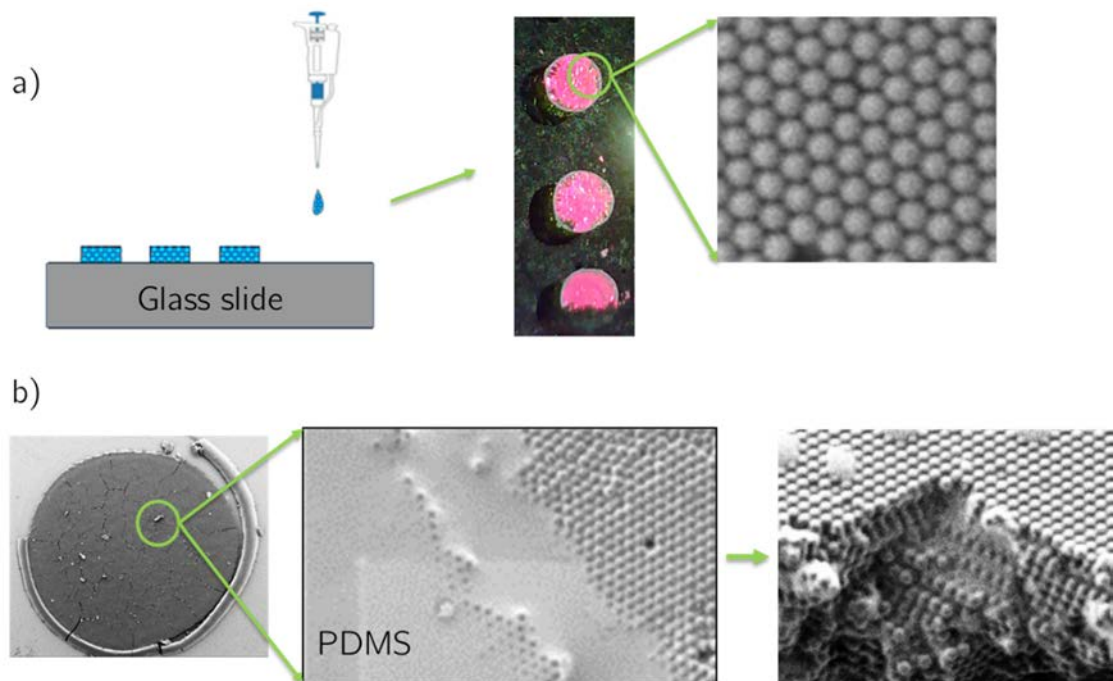
Figure 3.3 a) Fabrication scheme and SEM images of 3D-PhC fabricated by drop casting of $300\,nm$ PS nanoparticles, (centre) coloration of 3D PhC at $0\,^o$, b) SEM images of 3D PhC infiltrated with PDMS and (right) lateral profile of the 3D packaging.

In the infiltration process, the PDMS fills the interparticle spaces of the 3D PhC. Optically, the reflected colour peak, measured by UV-Visible spectrometry at 0° (**Figure 3.4a**), shows a colour change from $\lambda = 670nm$, to $\lambda = 595nm$ in accordance to the change of the packet surrounding media (as described in section 2.4.2). Thus, the colour change is produced from difference in the effective refractive index (η_{eff}) when the PDMS or air, with refractive index of 1,41 and 1, respectively, fills the interspaces (**Figure 3.4b**). Additionally, a white colour covers the infiltrated PhC specially in the border drop. The white colour corresponds to the index contrast and the greater number of layers at the border that gives a milky aspect.

The angle dependence of a 3D-PhC was measured by using two fibres in a mirror reflection mode. The 3D-PhC was placed in-plane and measured from 0° to 75°, these angles were formed by the incident angle θ_{in} and the reflected angle β, where $\theta_{in} = \beta$ (**Figure 3.4c (inset)**). A reflection spectra was obtained for each angle change, where the light striking the 3D-PhC structure reflecting its component colour, being the colour changed in concordance with the angle change. In this way, shorter wavelengths exit with angles distant to the normal than closer ones.
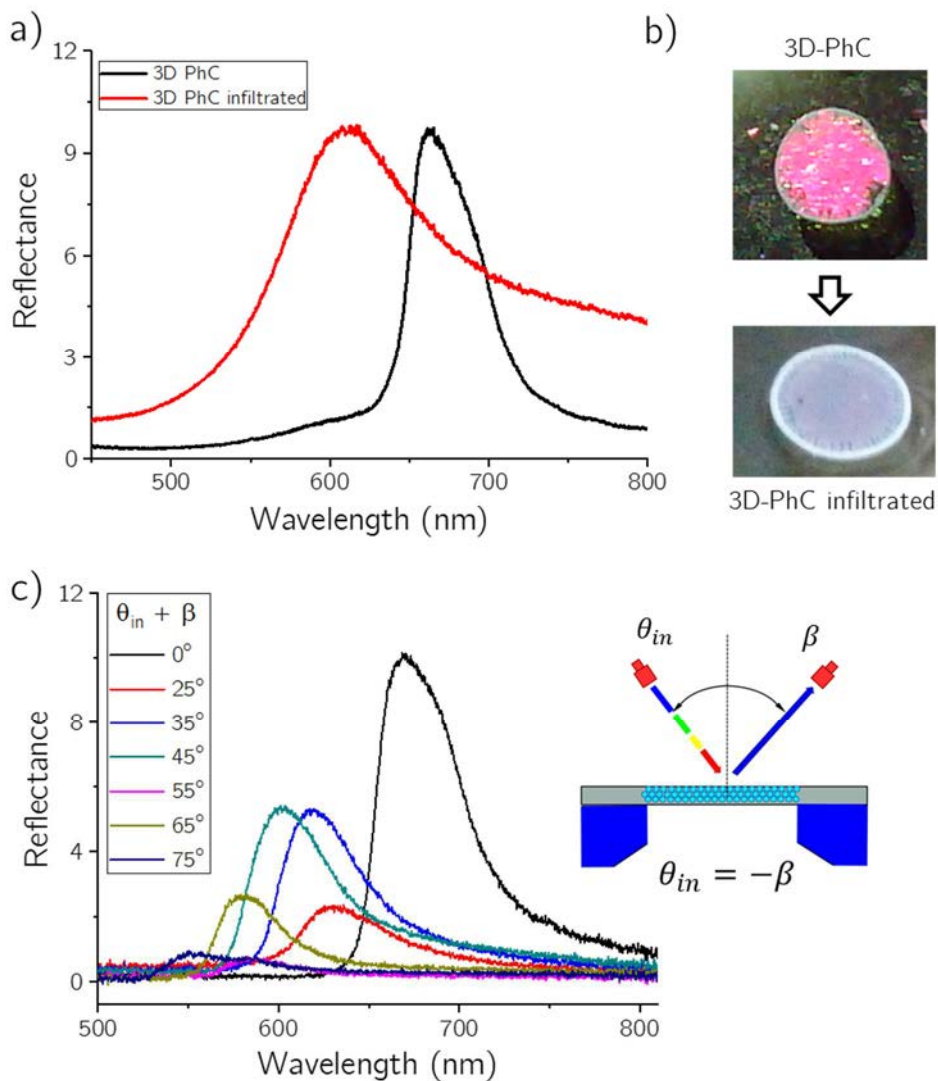
Figure 3.4 a) Reflectance spectra of 3D PhC before and after PDMS infiltration (measured at 0°), b) photography of 3D PhC coloration before and after PDMS infiltration, c) reflectance peak at different angles, (inset) schematic configuration of measure with the 3D-PhC material in plane and mirror reflection mode.

3.3.2 **2D photonic crystals**

The 2D-PhC was prepared by using a classical technique for assembly nanoparticles at the air-liquid interface [159] (Colloidal lithography, **Figure 3.5**). At air-liquid interface, the surface tension of liquid, the evaporation temperature and percentage of surfactant in nanoparticle solution are essential variables to achieve a high order close-packed monolayer. An aqueous suspension of $800\,nm$ polystyrene nanoparticles was diluted in ethanol, to reduce its surface tension, to form $10\,wt\%$ nanoparticles in a 60% ethanol mixture. A nanoparticle monolayer was created at the air-water interface by releasing $200\,\mu l$ of the solution over a partially immersed hydrophilic glass slide with a tilt angle of $20\,°$. A hydrophilic glass slide, previously immersed on the water volume, was used to collect the nanoparticles monolayer by removing the water carefully. Finally, the assembled nanoparticles were dried for 30 minutes at $80\,°C$ to evaporate the water and improve the crystallization.

PDMS ($10{:}1$ ratio) was spin-coated over the dried particles monolayer to achieve a $90\,\mu m$ layer of PDMS, and immediately cured at $100\,^oC$ for 1 hour to obtain only partially infiltrated nanoparticles. The 2D photonic crystal fabricated by using $800\,nm$ nanoparticles deposited over hydrophobic substrate is shown in **Figure 3.5**. The use of hydrophobic substrates allows the preparation of materials with the nanoparticles partially embedded on it, with $\sim 40\,\%$ of the particle out of the PDMS, producing an uniform and periodical diffraction grating with the ability to separate the different wavelengths of light. Completely embedded nanoparticles could be achieved by curing the PDMS infiltrated 2D crystals at room temperature. In this case the composite material would behave as a **1D photonic crystal**.
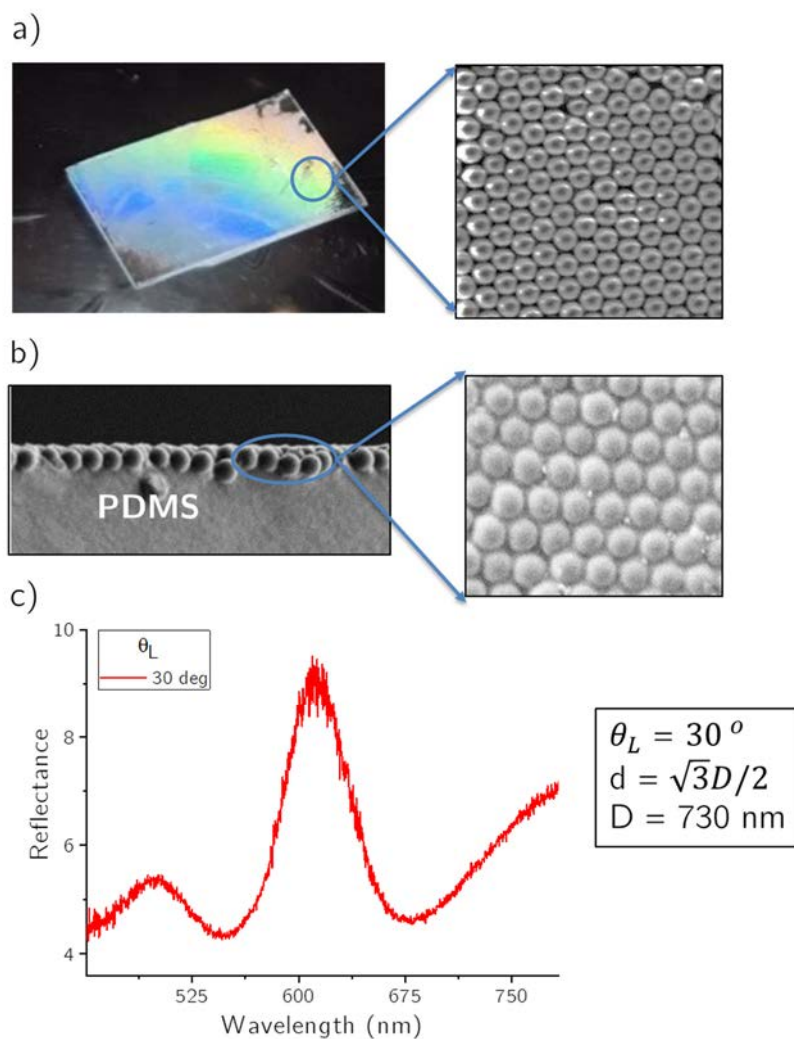
Figure 3.5 a) 2D-PhC fabricated by air-liquid interface, using $800\,nm$ Ps nanoparticles: (left) sample illuminated at certain angle, (right) SEM image of the 2D assembly; b) SEM images of the assembly partially embedded in PDMS, (left) lateral profile, (right) front face, c) reflectance peak captured in Littrow configuration at $30\,^{o}$.

3.3.3 2D diffraction gratings (inverse 2D-PhC)

Nanostructured materials based on assemblies of polymeric nanoparticles, as a two dimensional photonic crystal (2D-PhC), were used as master moulds for the fabrication of periodic 2D diffraction gratings. The 2D colloidal assembly was prepared as described in section 3.3.2. Non-uniform colloidal assembly gives as result a pixelated image with divided and subdued colours, reducing drastically the resolution of the final image. To be able to optimize the resolution of colours given by the mechanochromic material, the

process of colloidal lithography was also optimized by controlling the surface tension of the water. Triton result a useful solution to increase the surface tension of water; small amounts of Triton released in water is enough to reduce the Marangoni effect when the particles are released on the surface of water, helping the particles surf the water surface at the speed that are released on the ramp, producing the self-assembling in a monolayer. The degree of hydrophilicity of the ramp is very important to ensure a periodical and uniform self-assembly. The lack of hydrophilicity increases the creation of small grains, breaking the assembly pattern, changing in consequence the orthogonal direction of the diffraction grating (**see morphology section)**.

A thin layer of PDMS ($10:1$ ratio) was spin-coated over the dried particles monolayer, and immediately cured at $100\,°C$ for 1 hour. During the coating process, the PDMS fills the interparticle gaps while the nanoparticles remain stuck to the substrate. When peeled off from the substrate, the PDMS left an inverse shape into the cured PDMS, **Figure 3.6(right)**.
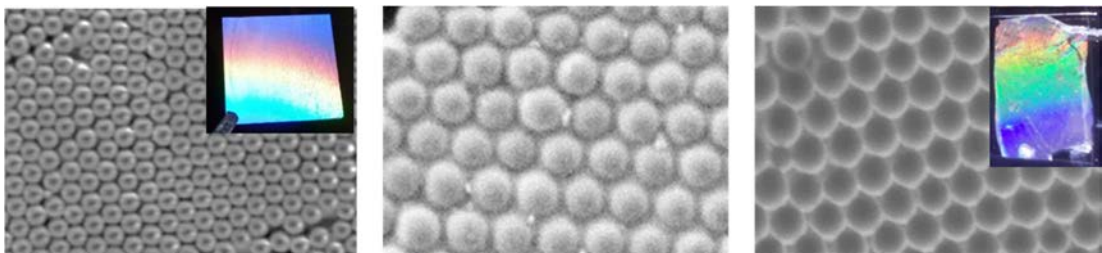
Figure 3.6. (left)Self assembled close packet nanoparticles on a glass substrate (inset)diffraction at $\sim 28^{o}$; (middle) master of colloids with PDMS residues filling the interparticle spaces; (right)PDMS replica with periodical nanovoids, (inset) light diffraction at $30^{\,o}$.

The nanostructured PDMS layer will be used to fabricate the suspended mechanical structures, both cantilevers and membranes, being the PDMS thickness a critical parameter to be controlled. Higher mechanical sensitivities will be achieved by reducing the PDMS thickness. Several thicknesses of PDMS were achieved by controlling the spin coating rate and time as shown in **Figure 3.7**. PDMS with thickness between $100\,\mu m$ and $20\,\mu m$ are easily manipulated. Below $20\,\mu m$ thicknesses the PDMS results very difficult to manipulate manually, being necessary to bond it to another thicker material for peeling-off from the substrate.
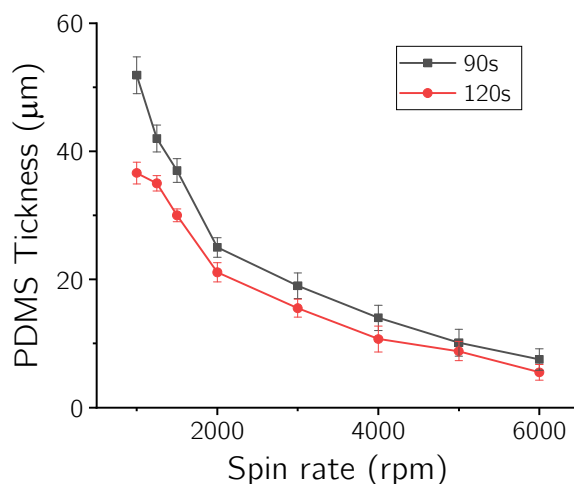
Figure 3.7. Thickness of PDMS when it is spin coated over a 2D colloidal structure, for a hydrophilic glass slice surface.

For spin rates up to $1000 \, rpm$, it is possible to get thicknesses of PDMS below $50 \mu m$ but it is difficult to maintain the periodicity of the close packet. The periodicity is lost because of the adhesion reduction between the nanoparticle assembly and glass slice when the spin rate is increased. To solve this loss of periodicity of the mechanochromic material, the basic fabrication method demonstrated before in **Figure 3.8** (Replication thickness $> 50 \, \mu m$) was modified. In this second approach, a thick PDMS layer is initially deposited over the assembled nanoparticles and peel-off from the substrate leaving a PDMS residue that fix the nanoparticles to the glass slide, as shown in in **Figure 3.8** (Replication thickness $<< 50 \, \mu m$). With this small variation in the fabrication process, and after a silanization treatment of the surface, the master is ready for spin coating at higher rates, being possible to fabricate mechanochromic materials with thickness around $2 \, \mu m$ for PsNp of $800 \, nm$ diameter without alterations in the periodicity of the master.
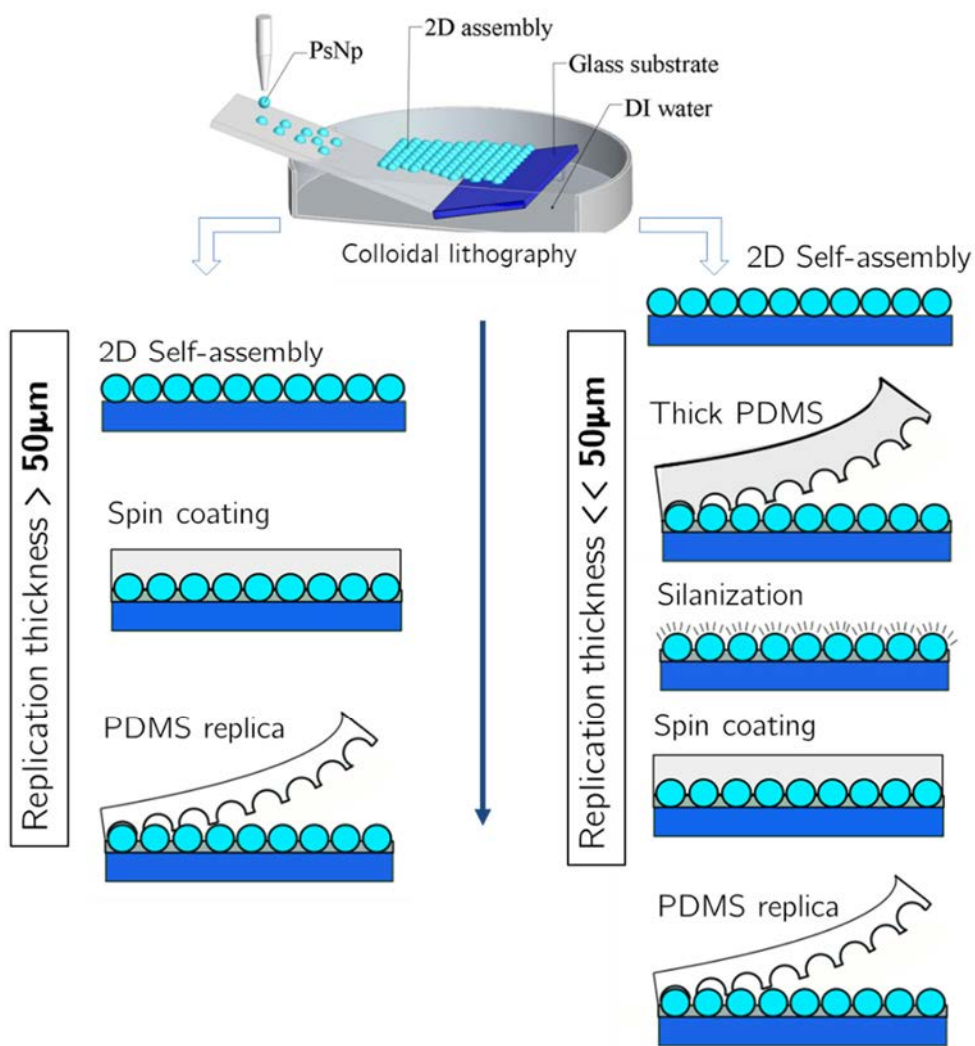
Figure 3.8 Schematic sequence of the fabrication of mechanochromic material based in colloids, (left) for thickness > 50µm, and (right) for thickness << 50µm.

3.3.3.1 Morphology

The morphology of the nanostructured material surface is critical to ensure the diffraction of white light. The surface needs to maintain the periodical nanostructure after master demoulding, with a period size in a range able to produce diffraction in the visible spectrum for colorimetric inspection. The calculation of grating sizes is well described in **Chapter 2:**, with the equation for a planar grating, $m\lambda = d\big(sen(\theta) + sen(\beta)\big)$, where $d = \sqrt{3}\,D/2$ for a close-packed monolayer, and D the sphere diameter. The grating depth has to be enough to produce a diffraction intensity able to be detected by visual inspection, or by a camera. In this way, the morphology of the mechanochromic

material based in an INV-2D diffraction grating has been morphologically characterized by processing of the SEM images, identifying the void size, height, and periodicity of the nanostructure. Image J free software was used to that end.

Some basic steps were followed to identify the void size. First, the SEM image was filtered to remove artefacts obtaining a clean image, then it was threshold in order to partitioning the image into a foreground and background defining the voids shapes, and posterior representation of its outlines (**Figure 3.9a)**. Second, a size distribution analysis of the cleaned image was performed, using the area covering by voids and calculating the diameter size distribution represented by a histogram. Third, the histogram was fitted by a Gaussian curve $y = y_0 + Ae^{-((x-x_c)^2/2w^2)}$, determining the voids average diameter (**Figure 3.9b)**. Bowl-shaped nanovoids with a mean diameter of $691 \pm 21\ nm$, $3.03\ \%$ of polydispersity, and height of about $320\ nm$ were calculated from SEM images analysis (**Figure 3.9d**).
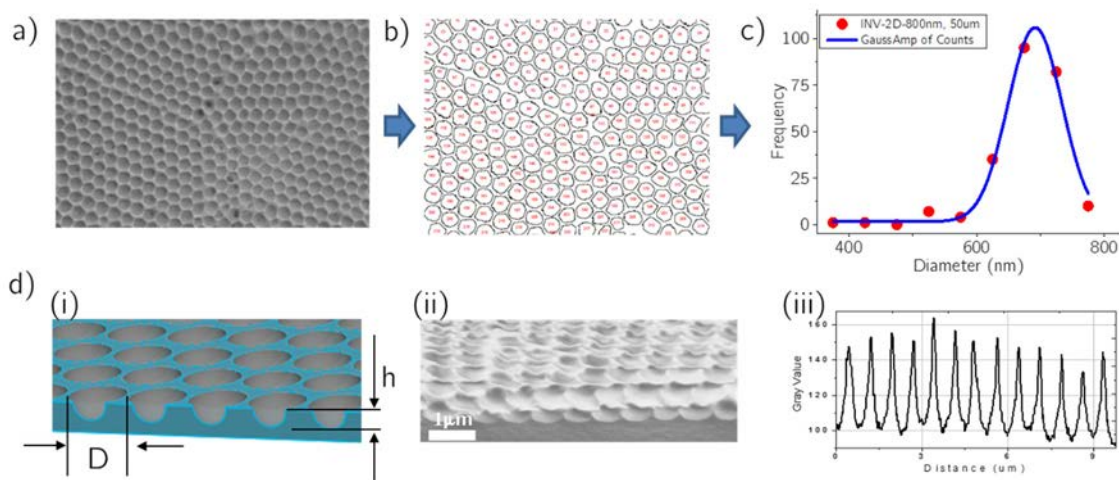
Figure 3.9 a) SEM image of the inverse nanostructure reproduced from a master of $800\ nm$ nanoparticles assembly, b) image after threshold and filtered, c) nanoparticles size distribution analysis, d)(i-ii) void diameter and height represented for calculation from SEM image, (iii) analysis of voids depths distribution by ImageJ (standard deviation of $12.6\ \%$).

These nanovoids are $7\ \%$ smaller than the nanoparticles used to prepare it. This size discrepancy can be attributed to the PDMS expansion after the

peeling process. The 2D PDMS nanostructure pitch was 745 ± 78 nm, in accordance with the PS nanoparticles size used.

Two dimensional Fast Fourier Transformation (FFT) was applied to SEM images in order to visualize the repeating elements of the crystal order, as shown in **Figure 3.10**. Three SEM images acquired from different areas of a single sample were used to calculate the FFT, including a SEM image of 2D array of colloids, **Figure 3.10a**. The bright spots demonstrate the high crystal order achieved. **Figure 3.10** shows the evolution of a 2D colloidal photonic crystal and its replications with long-range order towards a disordered structure by increasing the number of grain directions.

To quantify the effective ordering between spheres the FFT patterns have been analysed, considering only the positions of the nanostructures. The FFT pattern of the ordered nanostructure reveals its hexagonal symmetry, whereas in binary monolayers the FFT pattern is transformed to an ever reducing number of concentric circles, indicating loss of long-range order. These rings indicate some short-range order and correlated average distances between nanostructures. The higher number of rings, the longer the correlation extends in space. In the least disordered sample (**Figure 3.10**, inset), the number of circles substantially exceeds that of samples with more disorder. The distance between the rings of the FFT pattern corresponds to the effective separation of nanostructures in the SEM images.
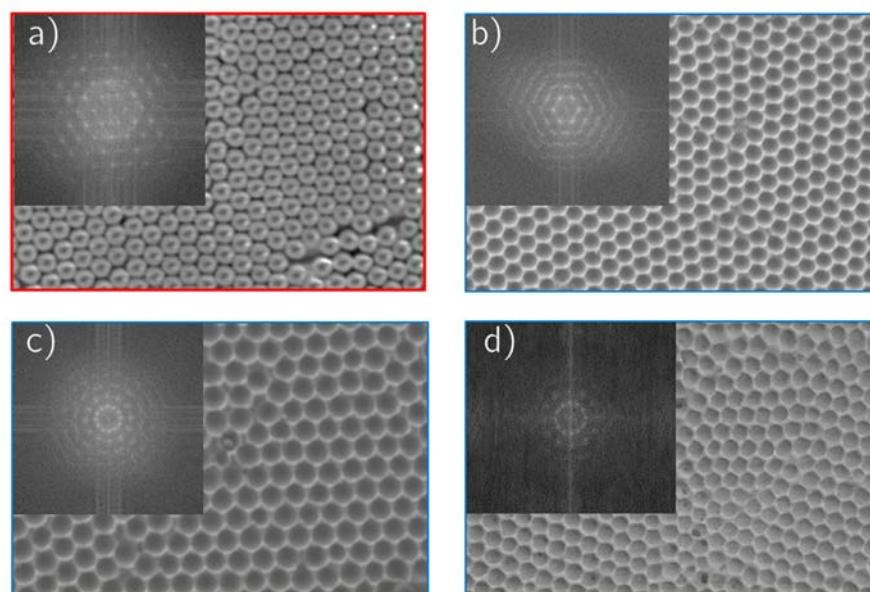
Figure 3.10 SEM images and the corresponding FFT from INV-2D structures: a) 2D array of colloids, b) nanovoids structure distributed in one single grain, c) nanovoids structured in different grain orientations, d) increase in the number of grain orientations and corresponding order reduction.

Having a hexagonal close-packet structure of around 691nm diameter nanovoids, the number of voids inside a $1\,\mu m^2$ area can be obtained by dividing $1\,\mu m^2$ by the surface occupied by a single nanovoid. However, it should be taken into account the free spaces that remain between nanovoids. The nanovoid area $A_{void} = r^2\pi$, for $691\,nm$ diameter, $A_{void} = 0.375\,\mu m^2$. Using geometry and simple calculations, the packing density of the hexagonal close-packet is around $70.2\,\%$. Thus, the real area occupied by nanovoids should be corrected and then the particle coverage calculated. The number of voids is determined by $n(void) = density/A_{void}$, obtaining $1.87\,voids/\mu m^2$, showed in **Figure 3.11a.**

Uniform and periodic assembly of particles will produce grating replication with uniform colour in a planar x and y directions, due to the nature of grating based in colloids (**Figure 3.11b**). Changes in the grain orientation contributed to the pixilation in the image (**Figure 3.11c**). The intensity of diffraction has a direct dependence with the depth of the grating for an inverse 2D, assuming the distribution in depths is uniform, if it is not uniform, the variation in depths increase de scatter of light [144], [145]. The minimum depth to produce diffraction able to be detected by visual inspection is in the order between $250\,nm$ to $300\,nm$ depth. High intense diffraction can be achieved with a depth around $400\,nm$ to $500\,nm$ for diffraction gratings fabricated with $800\,nm$ in diameter, being able to detect rainbows of colour directly with naked eyes as shown in **Figure 3.12**.
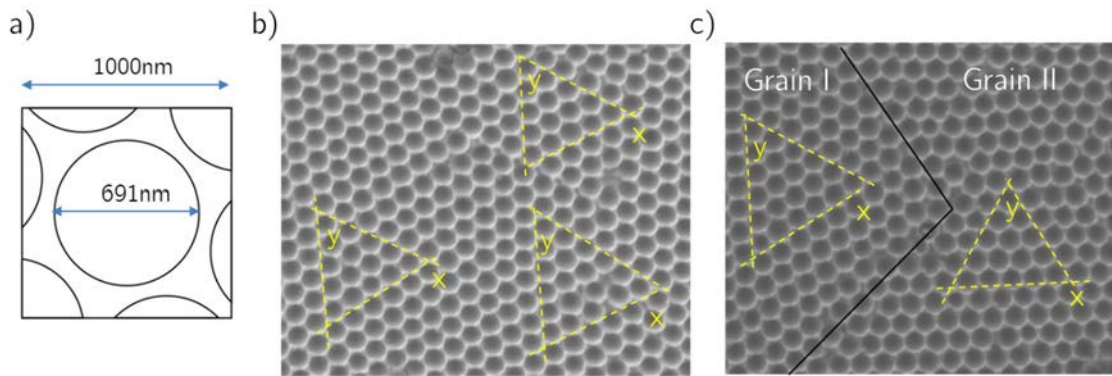
Figure 3.11. 2D diffraction grating morphology, a) nanovoid density per μm^2, calculations for PDMS replicas, b) location of grains orientation on the grating surface, c) ideal hexagonal close-packet in just one single grain plain.

Optical artefacts in inverse colloidal gratings also happen when the master of 2D assembly has double layer, producing irregularities in the planar surface of replication. These irregularities were identified as concave shapes in the surface that diffract at a different angle from the rest of the grating, showing an annoying optical characteristic of all grating surface with the ability of scatter light, illustrated in **Figure 3.12**.
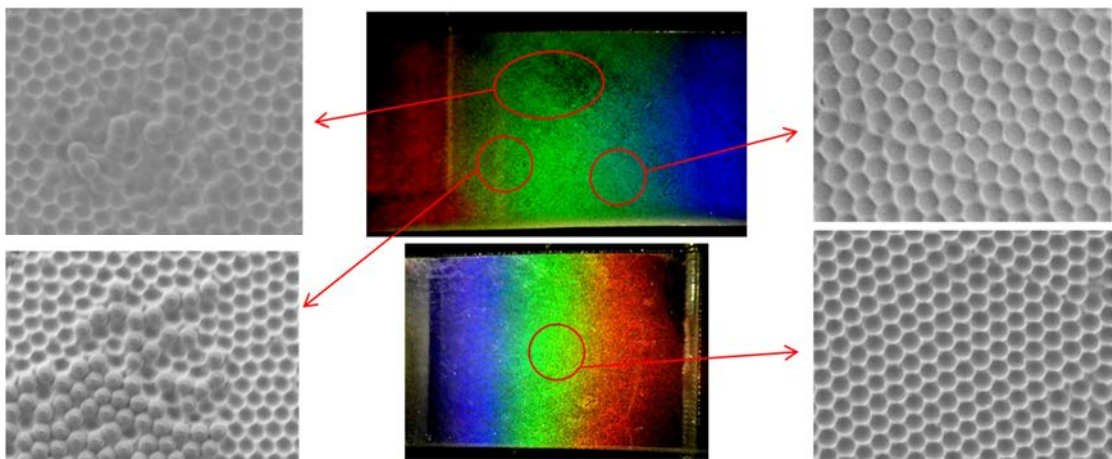
Figure 3.12. Grating imperfections spotted on a coloured surface and their corresponded SEM images.

3.3.3.2 Diffraction by angle dependence (calibration)

The diffracted colour of the 2D photonic materials was measured by using a bundle reflection probe in Littrow configuration, as in the setup implemented for 1D characterization (**Figure 3.2a**). In this case, the experimental angle between the probe and the normal to the membrane was $30\,^o$.

A calibration curve was obtained by measuring the colour change produced when focusing on a nanostructured PDMS film by changing the angle of incidence of the bundle reflection probe. In this case, a linear colour change was found, as shown in **Figure 3.13b**. The experimental data were fitted to the main diffraction equation in Littrow configuration, leaving the particle diameter as a variable parameter. The experimental results were fitted to the equation for a particle diameter of $730 \pm 2\,nm$, giving a wavelength change of around $20\,nm$ per degree.
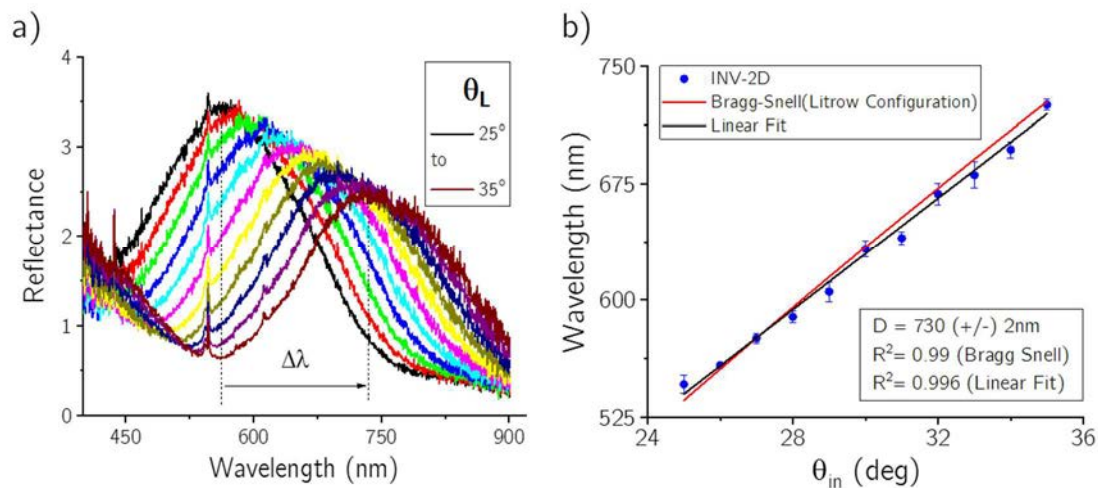
Figure 3.13 a) Wavelength response for angles of incident light, from $25\,^o$ to $35\,^o$, b) experimental diffraction wavelengths fitted by diffraction equation in Littrow configuration.

3.4 Photonic nanostructures fabrication at wafer level

A step further to fabricate the mechanochromic devices in high volume, increasing the yield and the reproducibility, is based in the use of waver scale standard microtechnology processes at the Clean Room. Colloidal lithography

has been demonstrated as a promising tool to nanofabricate in large areas, for their easiness of fabrication and low-cost [155], [160]. The use of these assemblies of nanoparticles as mask for surface patterning results a key tool for nanofabrication of diffraction gratings in large areas. The size and shape of nanoparticles allow manipulating the dimension of the patterning.

Large assemblies of nanoparticles on entire $4\,inches$ silicon wafers (**Figure 3.14**), keeping the hexagonal close-packed and uniformity of the monolayer, were achieved by optimizing the colloidal lithography variables used in previous section to fabricate colloidal assemblies over glass slides (liquid surface tension, percentage of surfactant, volume of nanoparticles released, and even dimensions of the liquid container).
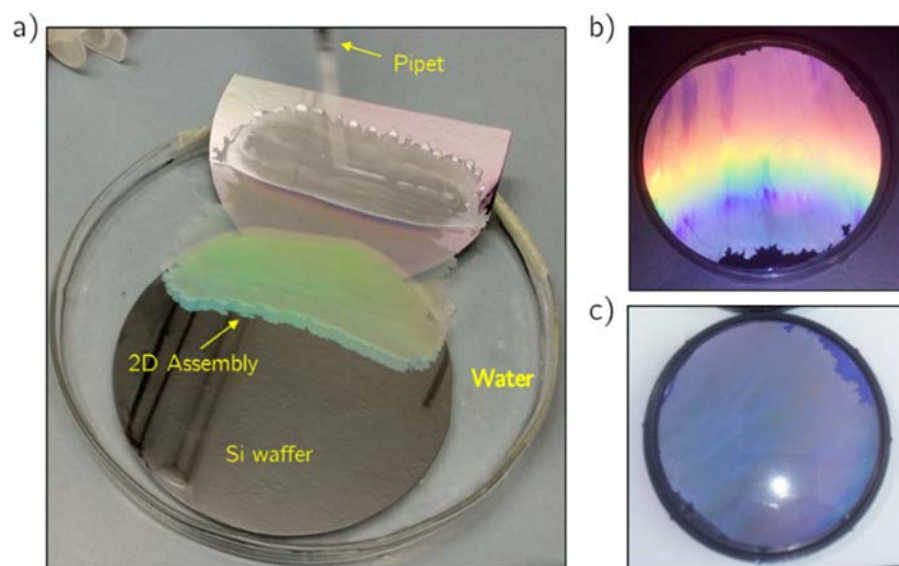
Figure 3.14. a) Colloidal lithography on a Si wafer; b) coloured wafer with 2D assembly illuminating at 30 degrees; c) 2D assembly illuminating at zero degrees.

The monolayer assembly deposited over the silicon substrate was used as mask to define the nanostructures on silicon; the interstices left between the particles allow the etching of the substrate by reactive ions (RIE) in order to create patterns of pores on the substrate. Dimensions of the interstices left by particles can be widened by a previous etching of the nanoparticles, controlling consequently the pore dimensions on the substrate. Two different approaches of nanofabrication based on colloidal nanopatterning has been done for the fabrication of mechanochromic materials based in 2D diffraction gratings. The

first one is the use of the nanoparticles monolayer to create a master of nanoholes for nanopillars replication in polymeric materials, as shown in **Figure 3.15a**. The second approach is based in a two steps fabrication of nanopores in silicon wafers for nanoholes replication in polymeric materials (**Figure 3.15b**). For these two methods, polystyrene nanoparticles and silicon wafers without any previous treatment were used.
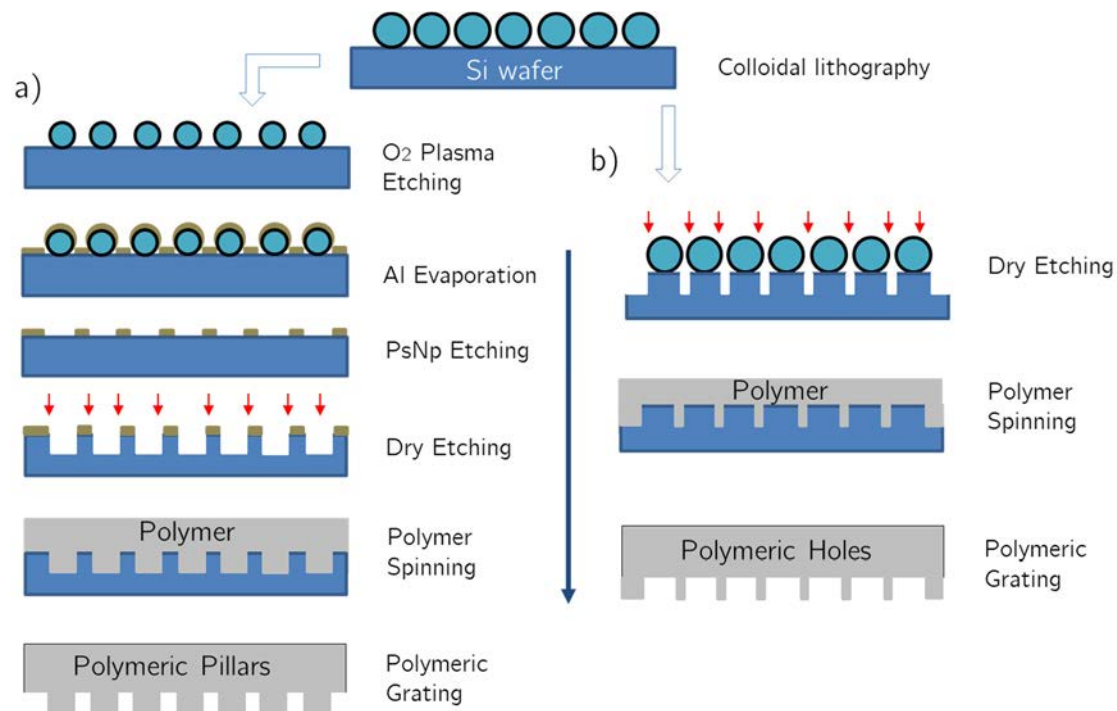
Figure 3.15. Top-down fabrication of polymeric diffraction gratings based on a) nanopillars, b) nanoholes

Polymeric Pillars

Diffraction gratings based on polymeric nanopillars were fabricated following the sequential process displayed in **Figure 3.15a.** Using colloidal lithography (explained in detail in **section** 3.3.2) nanoparticles with $800\,nm$ in diameter were self-assembled on a $4\,inches$ silicon wafer, after dried in an oven for a few minutes, the nanoparticles were etched by RIE O_2 plasma treatment for around two minutes at $500W$, obtaining a reduction of nanoparticles diameter in a range of $10\,\%$ to $15\,\%$. For etching proposes, a thin aluminium layer of $40\,nm$ was evaporated over the assembly in order to have a mask with

nanoparticles shape. With the aluminium over the silicon surface, the wafer was cleaned of nanoparticles by acetone bath, rinsed with ethanol and dried with nitrogen. The wafer was dry etched by RIE by an effective combination of two gases SF_6 pulsed at $150\,sccm$ for $1\,s$, and C_4F_8 pulsed at $100\,sccm$ for periods of $2\,s$, at $500\,W$ power, and $-10\,{}^oC$ temperature, for 2 minutes etching time. This process was able to etch nanoholes in silicon with around $400\,nm$ in depth. Finally, the aluminium layer was removed from the wafer by a hydrofluoric acid bath, leaving well-defined perforations with the periodicity of nanoparticle assembly (**Figure 3.16a** second image). For polymeric replicas based on PDMS, the wafer was silanized with PFTS to ensure the easiness in demoulding.

A critical point of diffraction gratings fabricated in large areas is to keep the periodicity of nanostructure after etching process. Several techniques have been used to fix nanoparticles to silicon wafer such as: treating the substrate with O_2 plasma previous colloidal lithography, heating the assembly of nanoparticles near the polystyrene melting point temperature, or immobilizing polyelectrolytes with positive charge on the substrate previous colloidal lithography. All these technics help in any way to keep the particles immobilized to the substrate, but during O_2 plasma process used to reduce the diameter of nanoparticles, the assembly loses its periodicity as much as increase the etching time. For etching times used to reduce until $5\,\%$ of nanoparticle diameters, the periodicity lost would be not considered, for diameters reduction higher than $5\,\%$, the imperfections are detectable as light scattering and ghosting in the final diffraction grating.

Polymeric Holes

In comparison with the nanopillars fabrication protocol, a shorter protocol was used to fabricate polymeric nanoholes. After colloidal lithography on a Si wafer, the colloidal assembly was used as mask to perform a controlled silicon etching. In the same way, the process used for pillars fabrication, an effective combination of two gases SF_6 and C_4F_8, for $2-3$ minutes etching time, was used to etches the non-covered silicon (**Figure 3.16b**, middle). With this etching process it was possible to reach depths between $500\,\mu m$ to $800\,\mu m$ respectively. The Si wafer was cleaned of nanoparticles by an acetone bath,

then rinsed with ethanol and DI water, and finally dried with nitrogen. To fabricate polymeric replicas based in PDMS, the Si wafer must silanized with PFTS, to avoid the bonding between silicon and PDMS. The thickness of PDMS is controlled increasing or decreasing the spinner speed rate, as shown in **Figure 3.7**. For replicas based in polyimide, the Si surface needs to be hydrophilic to achieve a uniform distribution of the polymer on it, as shown in **Figure 3.16b** (down).

3.4.1 Optical response

SEM images of nanopillars and nanoholes where used to evaluate the grating morphology, including the images acquired for each step of fabrication. In the same way than diffraction gratings based in nanovoids, the periodicity of the nanostructure is a key characteristic for diffraction. Materials used to replicate the silicon masters are also important to have a high quality of replication and optical response.

As shown in **Figure 3.16a (down)** the nanopillars replicated in PDMS tend to interact with each other after lift-off from the master, losing the periodicity of the nanostructure. The interaction increase when pillars are taller than $400\,nm$ for $800\,nm$ diameter. For nanopillars smaller than $400\,nm$ the interaction is minimum, but the intensity in diffraction is reduced close to $30\,\%$ for pillars around $280\,nm$ to $330\,nm$ (experimental tested), in consequence, PDMS result not to be the best material to fabricate nanopillars in these conditions. Other materials such as SU-8 or polyimide (PI) result in better alternative for nanopillars fabrication.
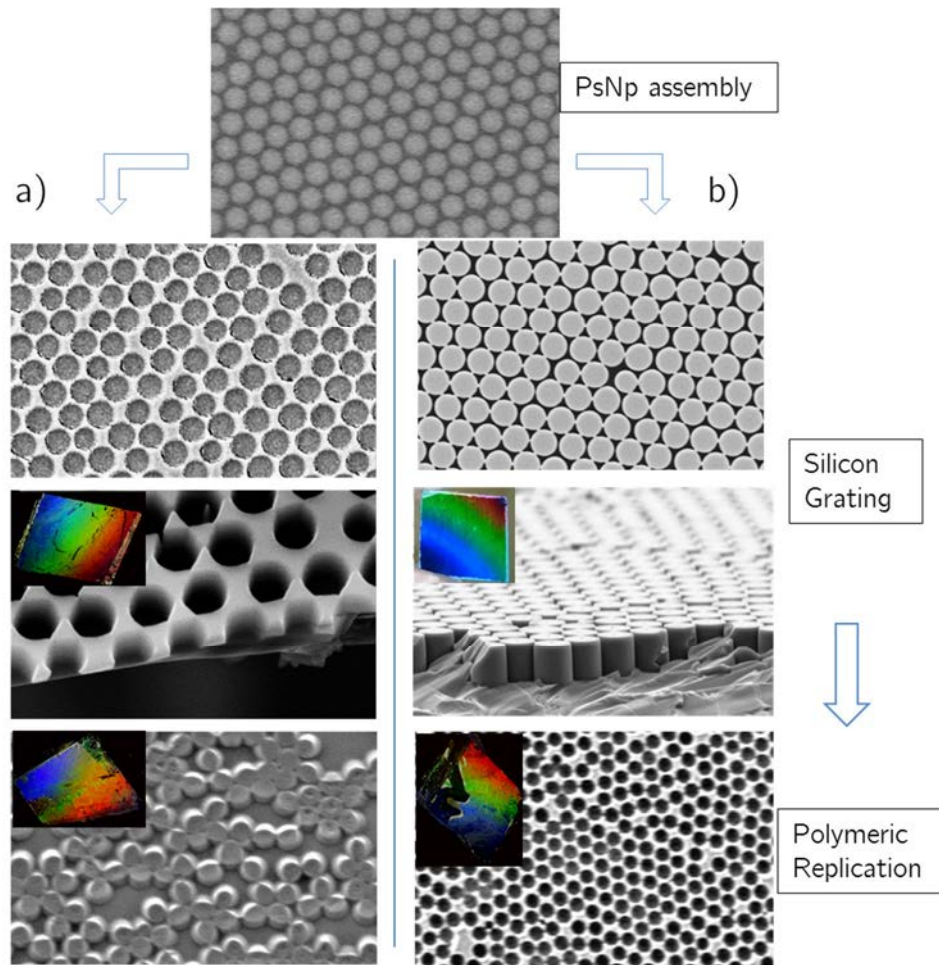
Figure 3.16. Morphology nanostructure inspection for each step of fabrication; a) nanoholes grating and its corresponding replicated PDMS nanopillars and, b) pillar grating and its corresponding polyimide nanoholes replication; (inset) diffraction of nanostructure at a certain angle of illumination and colour capture.

The diffracted colour of both structures, nanopillars and nanoholes, was measured by using the setup implement for 1D characterization in section 3.2. In this case, the experimental angle between the probe and the normal to the material was 25° and increased until 35° in steps of 1° (**Figure 3.17**). In similar way, a calibration curve was obtained by measuring the colour change produced when focusing on the nanostructured material. A linear colour change was found, as shown in **Figure 3.17a,b (right)**. The experimental data were fitted to the main diffraction equation in Littrow configuration, leaving the particle diameter as a variable parameter.

For PDMS nanopillars, the calculated pillar diameter was $768 \pm 6\,nm$, giving a wavelength change of around $20\,nm/^o$ with $R = 0.95$, as shown in **Figure 3.17a (right).**

For polyimide nanoholes, the calculated hole diameter was $744 \pm 2\,nm$, for a wavelength change of $20\,nm/^o$ and $R = 0.99$ similar to nanopillars (**Figure 3.17b (right)**).

In both cases, nanopillars and nanoholes, the fitting R decrease and increase in accordance to the periodicity of the nanostructure. The fitting to the PDMS nanopillars is worst due to the deformation and interaction between nanopillars.
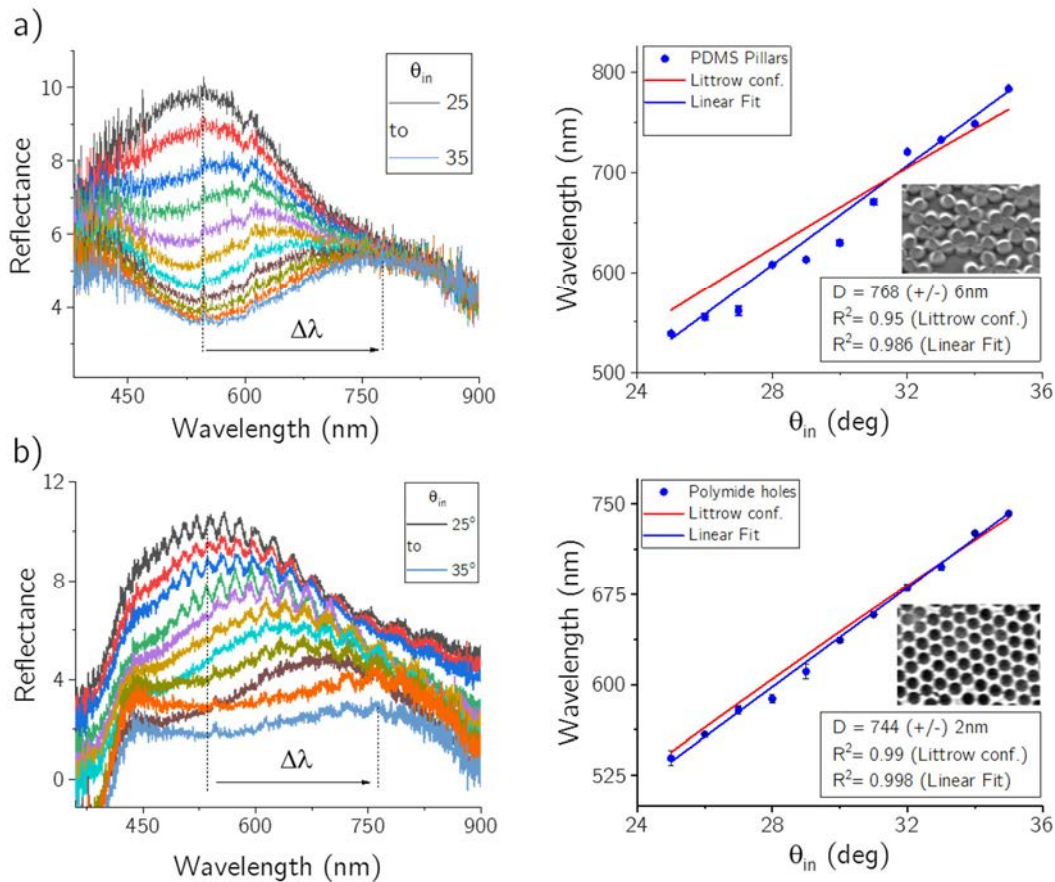
Figure 3.17 Reflectance measured in Littrow configuration and the calibration curve of wavelength peaks (linear fitting, and Littrow equation fitting) for: a) PDMS nanopillars, and b) nanoholes; (inset) nanostructured material SEM image.

3.5 Fabrication of suspended mechanical sensors with structural coloration

After the fabrication of the structural colour materials, the next step was the fabrication of suspended mechanical sensors with this property: circular membranes and microcantilevers. Rapid prototyping techniques were used to define the dimensions of the sensors. Microcantilevers were directly defined by cutting the nanostructured thin PDMS with a laser, while the membranes were fabricated by bonding the nanostructured PDMS to a hard and thin substrate with perforated holes (made by laser cutting or micromilling). A detailed explanation of the fabrication process and integration into microfluidics channels is completed in following chapters.

As a proof-of-concept, I have as well performed the first fabrication of microcantilevers at wafer scale. In this case, instead of PDMS, polyimide was spin coated over the nanostructured silicon wafer and cured at $350\,^oC$ (see section 3.4.1). Polyimide was chosen instead of PDMS because it's higher refractive index and easy implementation into Clean Room microfabrication techniques. Polyimide Young's modulus is three orders of magnitude higher than PDMS, which will reduce the sensor sensitivity. However, it is possible to fabricate thinness layers of material due to its low viscosity compared with PDMS, resulting in microcantilevers with similar bending behaviours (similar stiffness).

An array of cantilevers was replicated in polyimide with the nanoholes structuration in one face of cantilevers. For this process, a thin layer of polyimide was spin coated over the master wafer. Polyimide thickness of $1.4\pm0.1\,\mu m$ were achieved after the curing process. Next, the arrays of microcantilevers were fabricated by standard photolithography with a predesigned photomask, followed by an etching process. The dimensions of cantilevers were $1500\,\mu m$ length per $500\,\mu m$ width, disposed in 3 separated channels of 9 cantilevers each one, as illustrated in **Figure 3.18**.

Finally, the cantilevers were lit-off from the wafer. For this process, the wafer was deep in a petri dish with DI water at $60\,^oC$ for 30 minutes. After drying with nitrogen the cantilevers were peeled-off carefully with the help of an adhesive, leaving the cantilevers suspended.
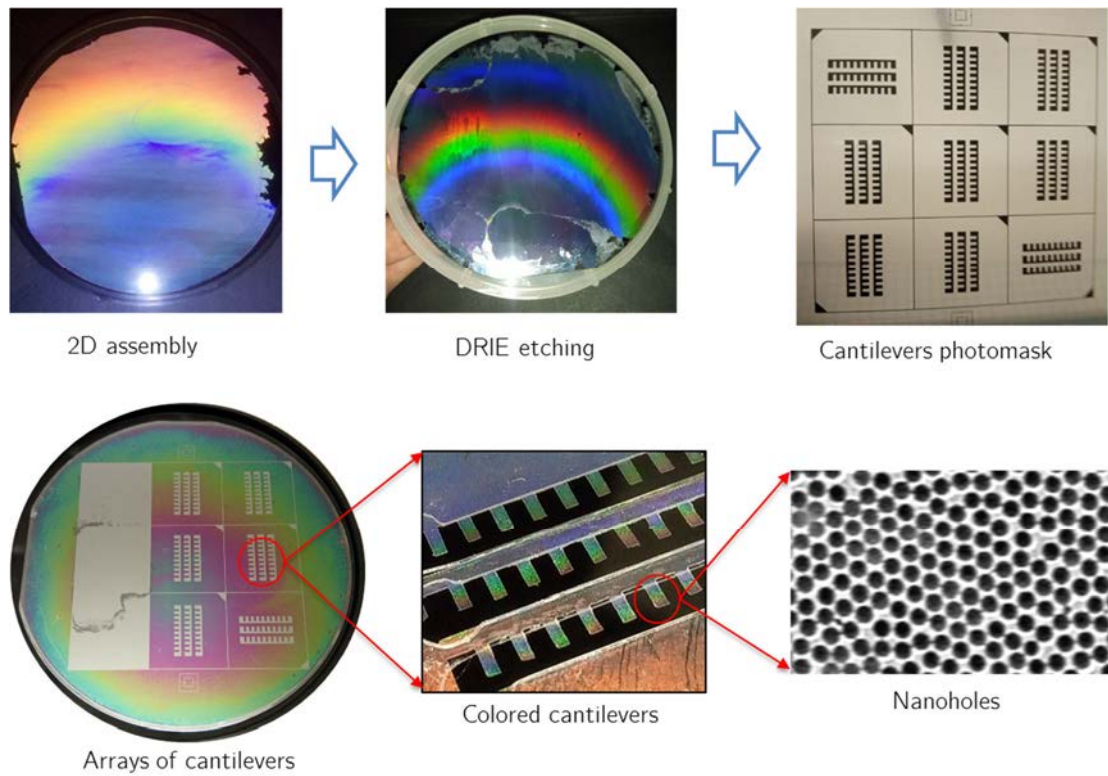
Figure 3.18 Referential sequence of fabrication of coloured cantilevers. First, 2D assembly is performed in a silicon wafer. Second, the silicon wafer is etched by DRIE (master for nanoholes replications). Third, a thin layer of polyimide is spin coated over the grating, next, it is etched by standard lithography with a predesigned photomask achieving arrays of coloured cantilevers; (right) SEM image of nanoholes.

Further work must be done to optimize the colloidal packaging, preferably by using spin coating techniques, to achieve an error free 2D grating mask, and total compatible process with standard microtechnologies processes. These tasks will be part of future work, and all the studies presented in next chapters were done by using rapid prototyping techniques to fabricate the mechanical sensors.

Chapter 4: Opto-mechanical analysis of structural colour materials

4.1 Introduction

In the attempts to get a real multidetection capability in a lab-on-a-chip or point-of-care device, the colorimetric sensors have become a promising route due to the lack of sophisticated instrumentation, and the possibility to perform a reading of the signal by visual inspection, or by using a smartphone camera to quantify the signal. Periodically structured polymeric photonic materials are particularly interesting to that aim, because its demonstrated sensitivity to mechanical stimulation [102], [107], [161], [162]. Fudoizi *et al.* fabricate opals-type photonic crystal infiltrated with elastomeric materials and demonstrate the colour tuning when applying linear strain deformations [107], [108]. Ito *et al.* demonstrate as well the strain-responsivity of interpenetrated polymer structured coloured network [163], which shows a Poisson's ratio close to that for an incompressible material, suggesting that the obtained elastomer deforms like a usual rubbery elastic material, in contrast to using hard colloids [107], [164]. Pressure-sensitivity has been as well demonstrated by using inverse opals-type photonic crystals, which produce photonic porous membranes with high sensitivity for force recording [165], and high sensitive reconfigurable shape-memory polymers [166].

In this chapter, I describe the opto-mechanical response of the fabricated structured colour materials, both under linear and bi-axial strain. For the bi-axial strain study, arrays of mechanochromic suspended membranes were fabricated.

4.2 Membranes fabrication and integration

Arrays of photonic membranes were fabricated by infiltrating colloidal PhC of polystyrene (PS) nanoparticles with PDMS, as described in Chapter 3:.

Array of 3D-PhC membranes. The **3D photonic crystals** were initially obtained according the drop casting method described in section 3.3.1, controlling the desired drop size which will define the circular membrane diameter. The particle concentration was chosen to obtain only few layers of ordered PS nanoparticles, to avoid the "leachy" effect and larger increase of the final Young's modulus of the membrane. The 3D photonic materials were prepared in a sandwich configuration. First, a $50\,\mu m$ layer of PDMS $(10\!:\!1$ polymer curing agent ratio) was spin coated on glass substrate and cured at $100\,^oC$ for 1 hour. Second, fifteen drops of $50\,\mu l$, and $1.25\,wt\%$ nanoparticles solution were released over the cured PDMS creating a $3\,x\,5$ array of drops and evaporated during 3 minutes at $95\,^oC$. Third, a thin layer of PDMS $(17\,\mu m)$ was spin coated over the dried 3D PhC, and leaved 15 minutes at room temperature to achieve a fully infiltration, and then cured at $100\,^oC$ for 30 minutes in an oven.

After the photonic crystals infiltration with the PDMS (**Figure 4.1** steps: **1-3**), the integration of membranes was performed (**Figure 4.1** steps: **4-6**). Oxygen plasma was used to bond the thin nanostructured PDMS to another thick PDMS with perforated holes to achieve the final array of suspended clamped membranes. After that, the membranes system was integrated to the microfluidic channels fabricated in PDMS by master moulding, again by using an oxygen plasma bonding. The master mould was fabricated in SU8 by standard photolithography process, and the PDMS was prepared in a $10\!:\!2$ ratio and cured at $100\,^oC$ for 1 hour in an oven.
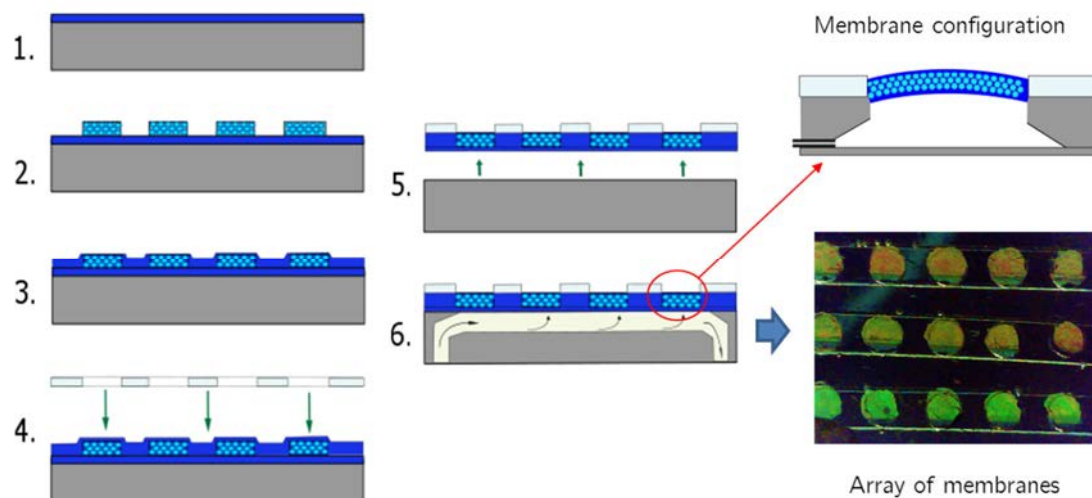
Array of membranes

Figure 4.1 3D-PhC membranes fabrication and integration sequential process: (1-3) 3D-PhC infiltration with PDMS, (4) bonding to o-rings, (5) lit-off from substrate and, (6) microfluidic integration.

Array of 2D-PhC and inverse 2D-PhC membranes. 2D photonic crystals were prepared by the air-liquid interface and infiltrated with a thin layer of PDMS (as described in section 3.3.2 for 2D-PhC and section 3.3.3. for inverse materials). In similar way than 3D-PhC materials, the 2D materials (PhC and inverse) were bonded to the microfluidic system by oxygen plasma treatment. After lit-off from the substrate, the PDMS (Microfluidics – 2D structured materials) was bonded to a thin Poly(methyl methacrylate)(PMMA), Cyclic olefin polymer (COP) or glass substrate with 15 perforated holes in order to clamp the membranes (**Figure 4.2**).
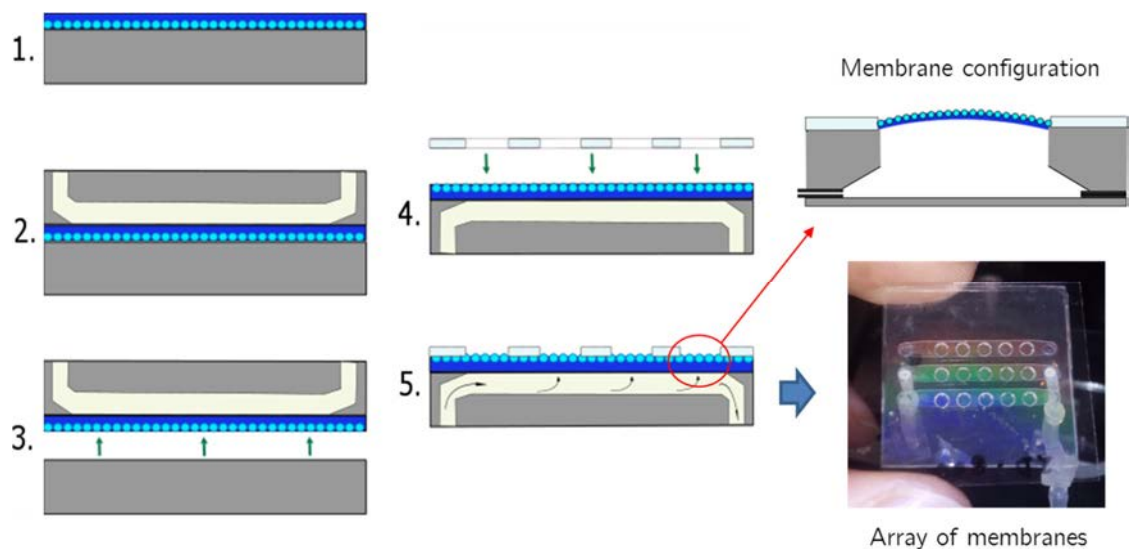
Figure 4.2 2D-Phd fabrication and integration sequential process: 1) 2D-PhC, 2) integration to the microfluidic system, 3) Lit-off from substrate, 4) o-ring array ($200 \, \mu m$ thickness PMMA with perforated holes, $1.5 \, mm$ diameter), 5) Array of membranes integrated to microfluidic system, (right) coloration at 30° and membrane profile.

4.3   Colour-strain relation

Experimentally, the colour response due to the applied strain was evaluated by UV-Visible spectrometry (Flame spectrometer from Ocean Optics)

and a bundle reflection probe (that emit white light from a central fibre and collect the back-diffracted light with the surrounding set of six fibres). Lineal strain was performed by clamping a rectangular nanostructured material in its two extremes to two micrometric screws disposed as shown in **Figure 4.8a**). Controlled lineal elongations were performed with this set-up in order to analyse the change of the material coloration for each step of deformation. The colour change was analysed by spectroscopy and by image analysis (Image J software).

For analysing the colour of the suspended membranes, the integrated device was mounted on a two-dimensional linear stage to select the membrane and the measurement position at the membrane. Membranes out-of-plane deformations (bi-axial strains) were produced by injecting a pneumatic pressure into the microchannels. A commercial pressure sensor (DP-101A-E-P), connected at the microchannel output, was used to measure the applied pneumatic pressure.

4.3.1 Photonic membranes based on 3D PhC

The colour reflected by 3D photonic membranes depends on the incident and reflection angles and the effective refractive index. As shown previously in **Figure 3.4**, an intense peak at the red region was measured for an incident and reflection angle of $0\,^o$. A shift to lower values of the reflected wavelength was observed when the PhC was infiltrated with PDMS (photonic membranes), due to a variation on the effective refractive index. An initial study on the effect of a linear (mono-axial) strain deformation on the fabricated composite materials was performed, before being bonded to the clamping support. In this case, a strip of the photonic polymeric material was fixed between two linear stages (**Figure 4.3a)**. Two fibbers were used to illuminated and collect the reflection from the material. The incident light angle was $\theta = 10\,^o$ respect to the normal surface, and the second fiber to collect the specular reflection was placed at $\beta = -10\,^o$. The spectrum was recorded for incremental strains ($50\,\mu m$ steps), showing a decrease on the reflected wavelength when increasing the strain (see **Figure 4.3b**). When increasing the mechanical strain, defined as $\varepsilon_x = \Delta L/L$, the material will elongate on the x direction, and will contract on the z direction, producing a decrease in the grating periodicity in the perpendicular direction $\Delta\Lambda=\lambda\varepsilon_{\perp}$, and therefore, a decrease in the reflected lambda. A maximum colour

change of $2\,nm$ was measured for an elongation of $600\,\mu m$, comparable to previous publications [167]. In **Figure 4.3b** is observable an hysteresis between the loading and unloading phases, due to the amount of energy dissipated in the material upon the loading-unloading cycle [168]. The system is recovered after the unloading phase, reaching the same initial value.

By using the integrated devices with the circular-clamped membranes, the membrane out-of-plane deformation was studied by UV-Visible spectrometry at specular reflection ($10\,^o$) and applying incremental constant pneumatic pressures. When applying an in-plane mechanical strain the material will elongate on the x and y direction, and will contract on the z direction, producing a decrease in the interplanar distance directly proportional to the vertical strain $\Delta d = \lambda \varepsilon_\perp$, and therefore, a decrease in the reflected wavelength. The perpendicular strain, $\varepsilon_\perp$, is determined by the mechanical properties of the material, by the ratio between the Young's modulus and Poisson's coefficient and the produced stress in plane, σ_x and σ_y, and has the form $\varepsilon_\perp = v/E(\sigma_x + \sigma_y)$.

The **Figure 4.3c** shows a small shift on the peak position for positive pressures, being impossible to measure the deformation for negative pressures. A colour change of $\Delta\lambda/\Delta p = 2\,nm/kPa$ was measured for 3D-PhC membrane with a PDMS thickness of $67\,\mu m$. Looking at the equation that describe the membrane deformation (equation (2.10)), one possibility to increase the produced shift and therefore the sensitivity to measure strain deformations would consist in reducing the thickness of the membrane or increase its radius, which could increase as well the buckling effect. The other parameters that affects the device sensitivity are the Poisson's coefficient and the Young's modulus. When the colloidal photonic crystal is embedded into the PDMS, the effective Poisson's coefficient is reduced while the Young's modulus increase, reducing the maximum deflection respect to pure PDMS membranes. An alternative would consist in the fabrication of inverse 3D opals, which could solve this drawback. However, our attempts to obtain inverse 3D membranes have been unsuccessful.
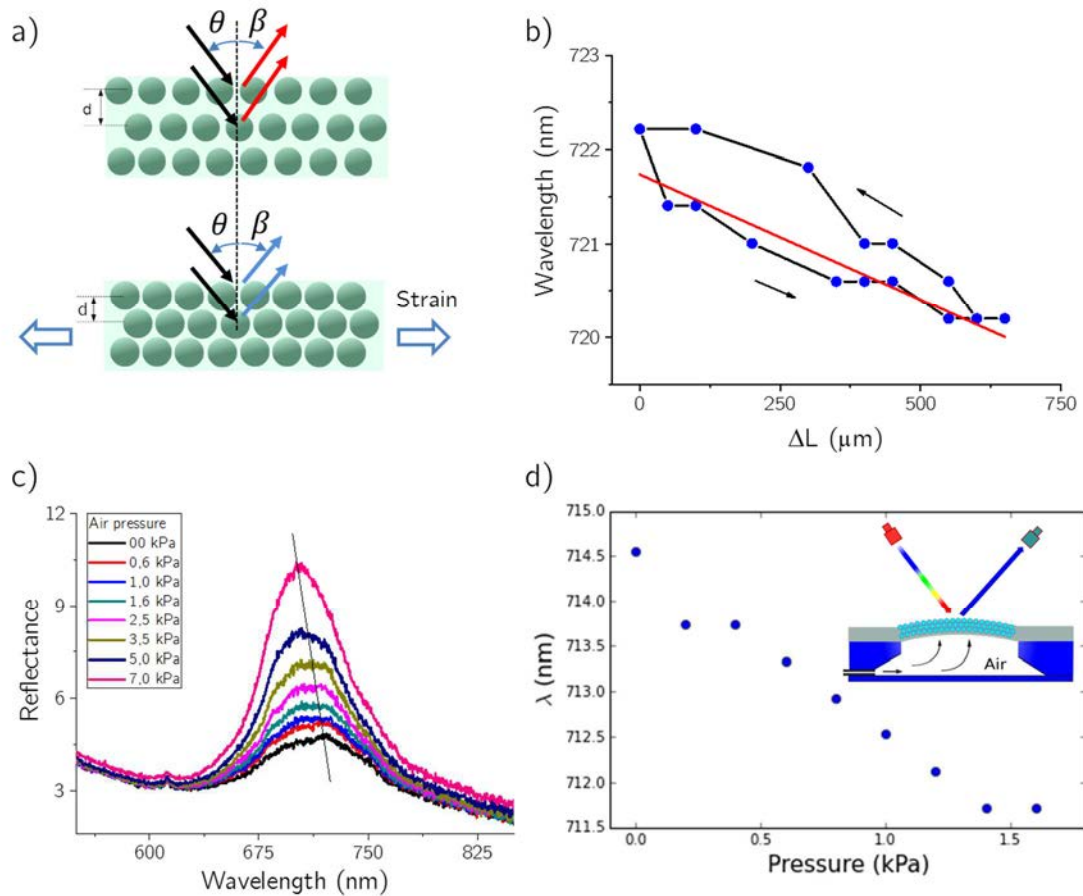
Figure 4.3 a) 3D PhC interlayer distance change by lineal strain, b) experimental wavelength response under linear strain stimulation and hysteresis behaviour during the load and un-load test, c) reflectance spectra dependency with applied pressure for circular clamped membranes and, d) experimental wavelength relation with the applied pressure (clamped membranes).

4.3.2 Photonic membranes based on 2D PhC

The diffracted colour of the 2D photonic materials was measured by using a bundle reflection probe in Littrow configuration (section 2.4.1.3), with a spot diameter of about $500\,\mu m$ over the membranes. Measuring in Littrow configuration, $\theta = -\beta$, and $m\lambda = 2dsen(\theta)$, for $m > 0$. The experimental angle between the probe and the normal to the membrane was $30\,^o$. The measured peak intensities were quite low compared with the 3D photonic membranes, due to the material transparency and the low difference in the materials refraction indexes.

The material colour tuning due to the application of a linear mechanical strain is shown in **Figure 4.4a**. The reflected wavelength increases when increasing the strain (due to larger distance between the nanoparticles), as expected. When increasing the strain, the grating periodicity change, increasing the reflected lambda. During the elongation process, two different elastic behaviours can be observed, with different slopes, and therefore different sensitivities. Larger colour variations are observed for smaller deformations ($\Delta\lambda = 7\,\text{nm}$ for an elongation of $750\,\mu\text{m}$, with an experimental slope of $\Delta\lambda/\Delta\text{L} = 0.5$), while lower variations are observed for linear elongations larger than $750\,\mu\text{m}$ ($\Delta\lambda = 2\,\text{nm}$ for an elongation until $1500\,\mu\text{m}$). As in the 3D-PhC composite materials, a hysteresis loop is observed during the loading and unloading process.
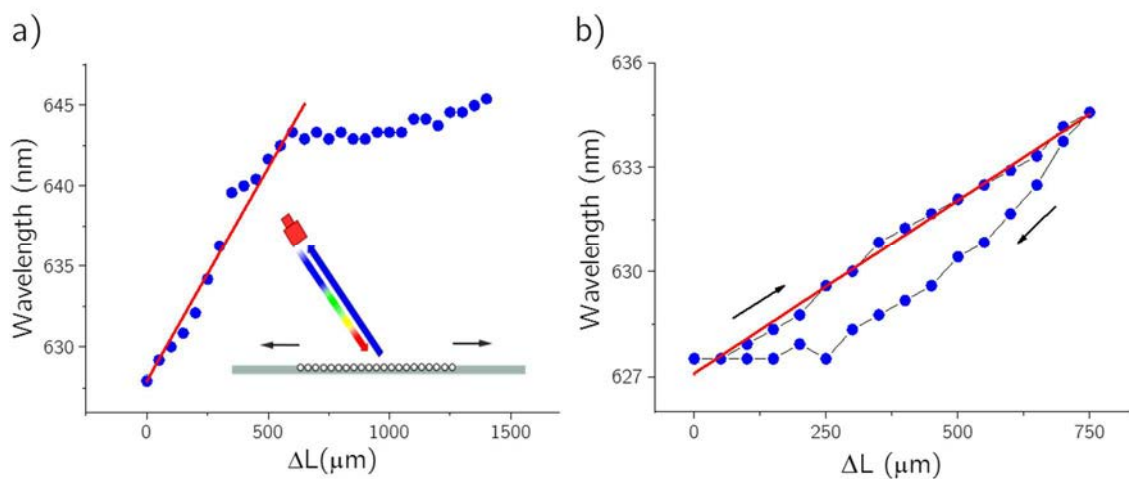
Figure 4.4 Experimental wavelength change with the applied linear strain (a), and wavelength recovery after the loading and un-loading experiment (b).

In the case of the circular-clamped membrane, the out-of-plane deformation produce wavelength changes in opposite directions, when applying positive or negative pressures. Depending on the position of focus inside the membrane, the reflected wavelength would increase or decrease for positive pressures, and vice versa. This effect is due to the change in the effective angle of incident when the membrane is deformed. This effect of the membrane curvature on the reflected wavelength can be observed in **Figure 4.5a**, where for an applied constant pressure, the reflected peak change when focusing at the centre, or in two opposite points of the membrane. Focusing out of the center

of the membrane, the reflected wavelength decrease when applying positive pressures, and increase for negative pressures, due to a positive variation on the effective angle of incident (**Figure 4.5b,c**). A Lambda change of $40\,nm$ was measured when applying $1\,kPa$ pressure to a $90\,\mu m$ tick membrane, which produces a maximum displacement of the centre of the membrane of $90\,\mu m$ with and angle α of 10° (measured optically) (see **Figure 4.7** for $1kPa$ pressure).
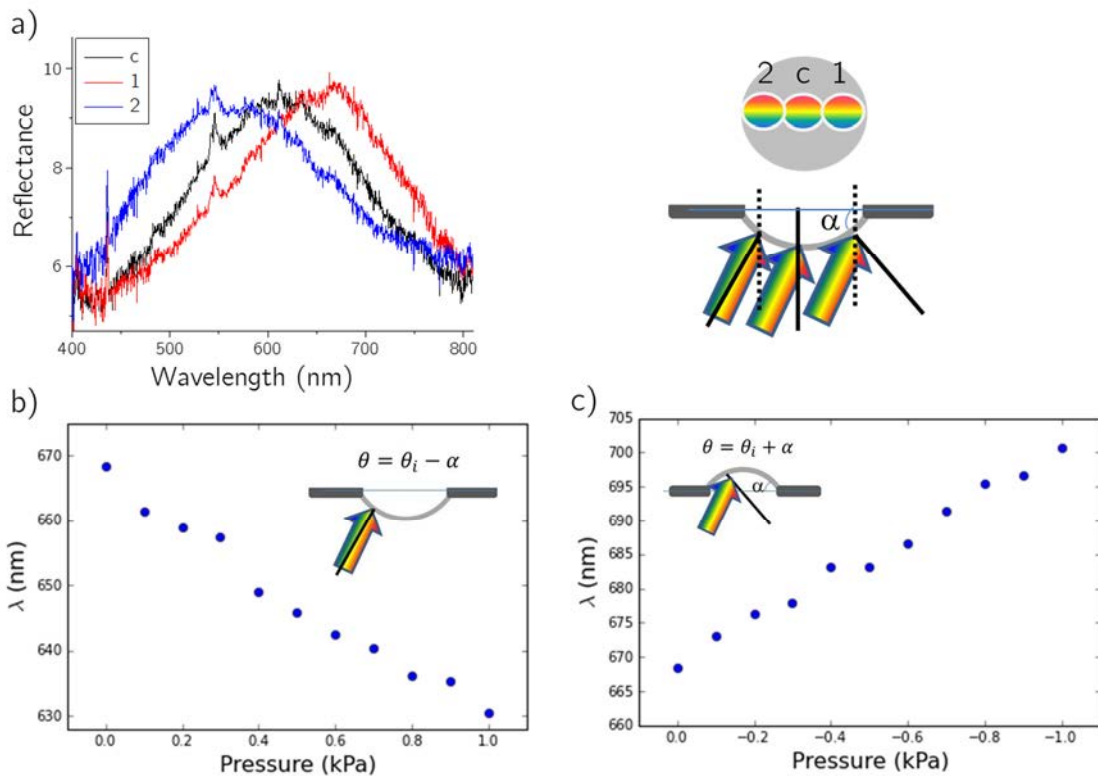
Figure 4.5 a) Experimental reflectance spectra measured at different positions of the clamped membranes. Reflected wavelength dependency for: b) positive and c) negative pressures.

In order to analyse the colour change of the membranes, a setup based in a Dino-Lite camera was implemented. For this propose, a $30\,W$ halogen white light source, which was collimated in order to minimize the spreading of light, was used. The incident angle θ_{in} of the light source fibre was placed at $30^{\,o}$, emitting at $9\,W$ of brightness. The camera was placed a 0° respect to the normal surface.
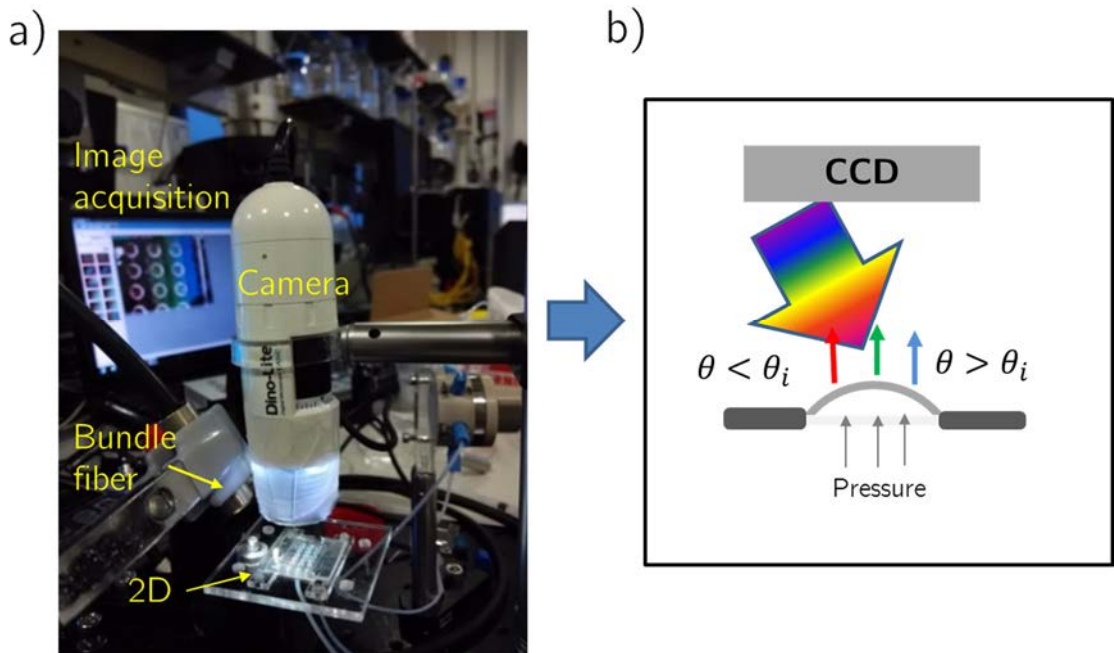
Figure 4.6 a) Image acquisition setup, b) configuration profile for membrane under deformation and colour changes captured by camera.

Small pressures from 0 to $3kPa$ were induced into the membrane system. With the help of a second camera, the lateral profile of a single membrane under deformation was captured as shown in **Figure 4.7**. Image sequences were acquired for each pressure applied into membranes evaluating the colour change due to the curvature effect.

Figure 4.7 shows the colour associated to initial unstressed membranes at $0 \, kPa$ of pressure, and the change in membrane coloration after $3 \, kPa$ of pressure. The deflection was measured at the centre of the membrane by image analysis (ImageJ software). The maximum deflection for $3 \, kPa$ pressure was $145 \, \mu m$, for a membrane of $1500 \, \mu m$ diameter and $90 \, \mu m$ thickness.
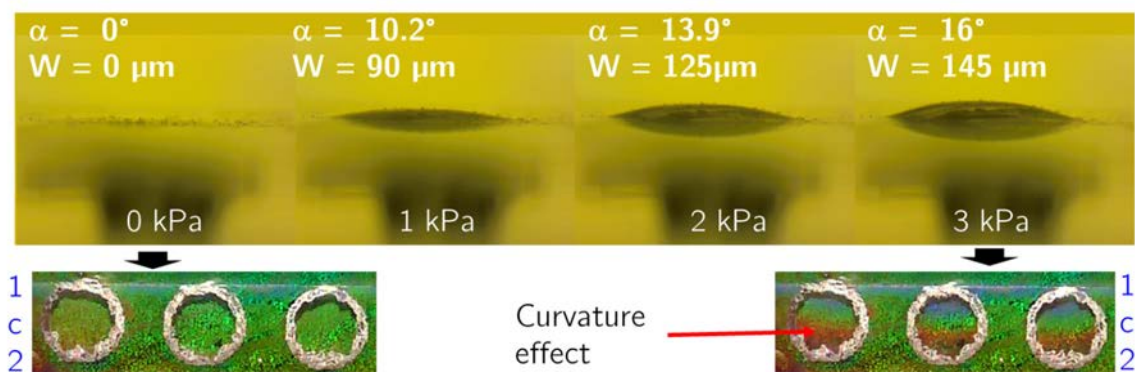
Figure 4.7 Lateral profile of a membrane under deformation by pressure, (down) colour associated for initial flat membrane and colour change due to the curvature effect.

4.3.2.1 Opto-mechanical response of inverse 2D-PhC

According to the main diffraction equation, changes in the periodicity of the nanostructure will produce changes in the diffraction wavelength. If the strain is produced in x direction the grating period suffers an elongation proportional to the variation of material length, while the period is being stretched in y direction, with a maximum stretching in the centre of the material. That relation is represented by Poison coefficient. At this stage, the simple stretching of a few percent of the material in one direction is used to induce strong variations in the period between particles (**Figure 4.8b**).

PDMS has a Poisson ratio of about $\nu = 0.5$, thus stretching the sample $20\,\%$ in one direction leads to a compression of $10\,\%$ in the orthogonal direction. As a first example of nanovoids size calculation after elongation, the SEM image illustrated in **Figure 4.8b** was used. From this image, it is possible to estimate the deformation of each nanovoid in the planar x and y direction for the stretching and elongation respectively. The linear elongation (**Figure 4.8b**) is about $22\,\%$ in x direction, for a void size D around $691 \pm 21\,nm$ (calculated from SEM images described in section 3.3.3.1), after elongation the size of each void is calculated as following, $D_x + 22\% = 843$ nm, and $D_y - 11\% = 615\,nm$.

In order to approximate the diffraction produced for the calculated void size $D_{x,y}$, the equation (2.32) for Littrow configuration was used for θ at $30\,^o$, $\lambda_x = 729\,nm$, and $\lambda_y = 532\,nm$. In consequence, the $\Delta\lambda_{x,y}$ calculated was $\Delta\lambda_x = 131\,nm$ and $\Delta\lambda_y = 66\,nm$ for a linear elongation of 22 %.
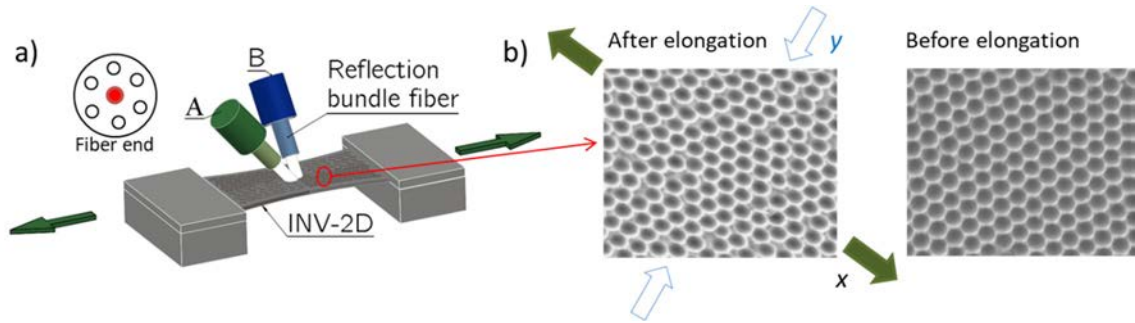
Figure 4.8 a) Schematic of the linear strain experiment, where the mechanochromic material is clamped in two extremes, and it's experiment controlled elongations in order to analyse its opto-mechanical response (Fiber (A) Points white light in the direction of elongation (x axis) and Fiber (B) is pointing white light in the orthogonal coordinate (y axis), at 30° for both fibers, (inset) reflection bundle fiber end), b) SEM image of the inverse 2D grating under linear deformation in an orthogonal plane (left), and before deformation (right).

Experimentally, the diffracted colour of the inverse 2D material was measured by UV-Visible spectroscopy as previously described (**Figure 4.8a**). A sequence of twenty steps was captured for each orthogonal direction (**Figure 4.9**).

For this experimental assay, a piece of material of $17.25\,mm$ long and $7.76\,mm$ width was mounted in a setup to produce controlled elongations in steps of $100\,\mu m$, until a final length increase of $\Delta L \approx 2000\,\mu m$. The maximum elongation corresponds to $10.78\,\%$ in the x direction, and $5.67\,\%$ in compression in the orthogonal direction. The $\Delta\lambda_{x,y}$ achieved after linear strain was $\Delta\lambda_x = 95\,nm$ and $\Delta\lambda_y = 30\,nm$ (**Figure 4.9a,b**).

The fitting of the reflection curves releases a pitch of $718 \pm 2\,nm$ for elongations from 0 to $2000\,\mu m$ (**Figure 4.9ab** down). For the orthogonal direction x, the spectra was fitted fixing the void size D and leaving the angle θ as an adjustable parameter. The fitting release a small variation in the angle θ, from $30\,^o$ to $31.5\,^o$. In both cases, $\lambda_{x,y}$, for elongation and it's orthogonal fits

the diffraction equation for littrow configuration, with a $R_x^2 = 0.909$ and $R_y^2 = 0.771$ (**Figure 4.9ab** down). The $\lambda_{x,y}$ points at the first steps of strain and the points of maximum strain are identified as small variations between the grains of nanostructured surface, and an optomechanical effect produced when the void is under elongation in the x plane and compression in its orthogonal y plane. In both cases, the wavelength response shows hysteresis behaviour during the load and un-load strain test, as shown in **Figure 4.9**.
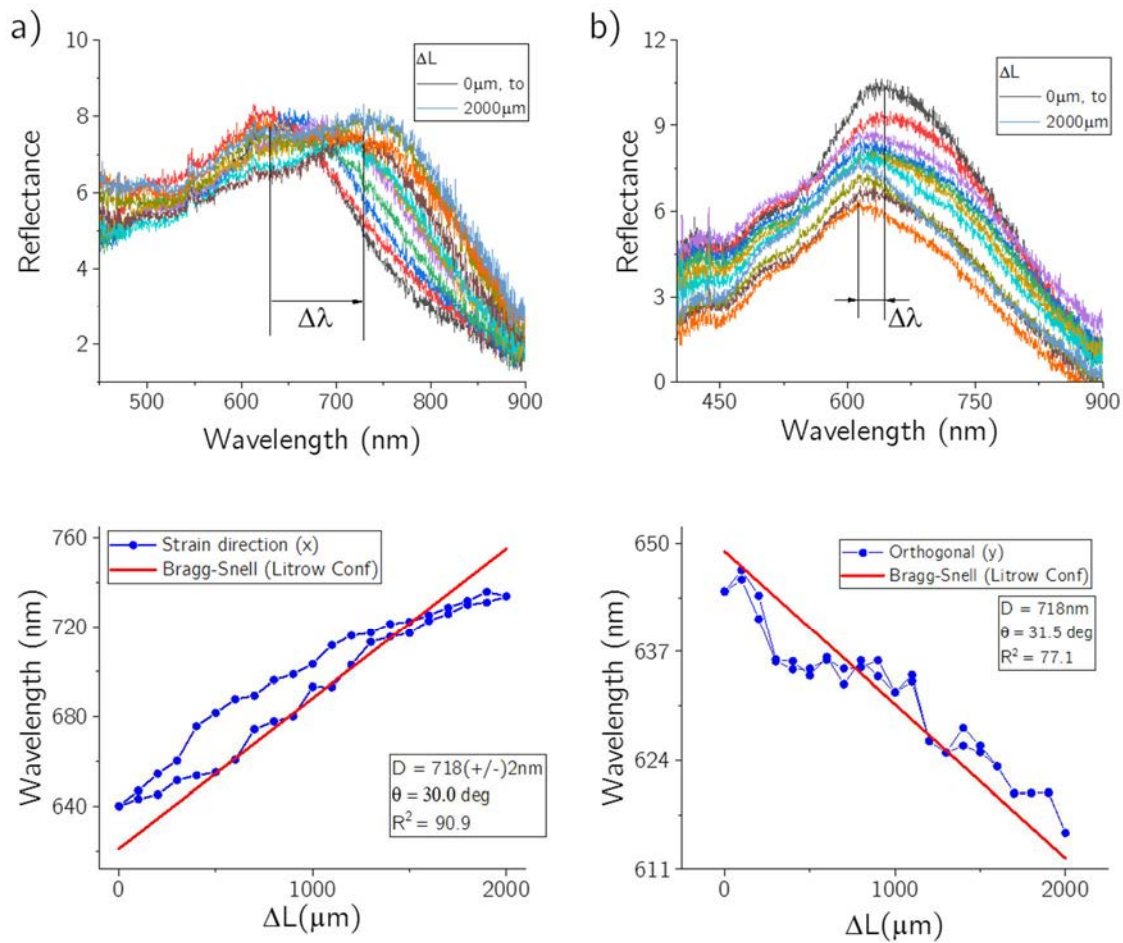
Figure 4.9 Wavelength spectra obtained experimentally by lineal strain test, a) red-shifting measured by pointing the fibre in the strain direction x, and (down) hysteresis behaviour during the load and un-load test, and, b) blue-shifting measured by pointing the fibre in the orthogonal direction y and (down) hysteresis captured during the load and un-load test.

The setup illustrated in **Figure 4.10a** shows the configuration used to measure the colour diffracted by nanostructured materials by image analysis.

For this propose, a $30\,W$ halogen white light source, which was collimated in order to minimize the spreading of light, was used. For this test, the incident angle θ_{in} of the light source fibre was placed at $-50^{\,o}$, emitting at $18\,W$ of brightness. A Dino-Lite camera was used to collect the diffracted light at 0°. A piece of nanostructured material (INV-2D) of $17.25\,mm$ long and $7.76\,mm$ width was mounted in a setup to produce controlled elongations in steps of $200\,\mu m$, reaching a final length increase $\Delta L \approx 2000\,\mu m$. The material was elongated from $0\,\%$ to $11\,\%$, ΔL, capturing images for each step of elongation.

For this experimental test, the colour change was measured at the centre of the sample where the maximum deformation was produced. The colour at the centre of the sample change from green to red after $11\,\%$ of linear elongation (**Figure 4.10b**). In this case, the approximation of $\Delta\lambda$ was $100\,nm$. This $\Delta\lambda$ obtained by image analysis is in the same range of the $\Delta\lambda$ achieved by spectroscopy (**Figure 4.10**) as a first comparison test.

A basic colour evaluation was as well done by analysing the change of the Hue value (from the HSV colour space, were the H value represent the colour) at the central section of each image. A $\Delta Hue = 64^{\,o}$ was obtained for a lineal elongation of $2000\,\mu m$ (as illustrated in **Figure 4.10c**).
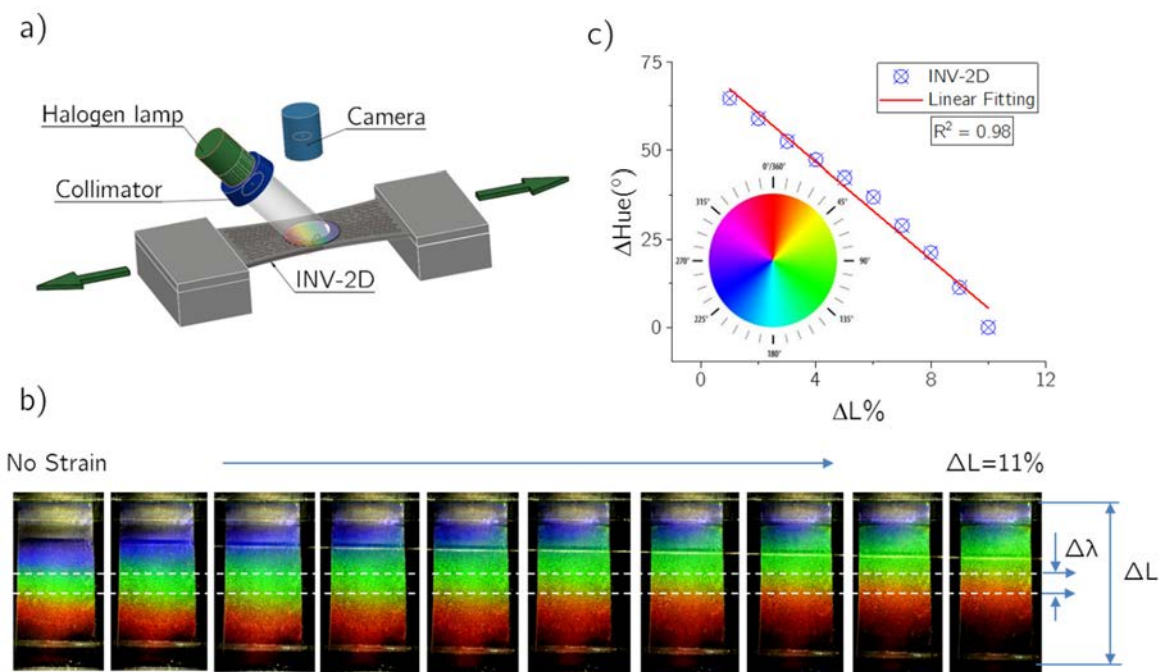
Figure 4.10. a) Set-up scheme showing the angle of incident of light and camera configuration during the linear strain test b) sequential images acquired for a range of linear strain (0 % to 11 %) and, c) calibration curve for linear strain (linear fitting with slope $= -6.86\,^{o}$ and $R^2 = 0.98$), (inset) Hue scale for visible spectrum.

In the same case than 2D membranes, inverse 2D membranes were characterized by pneumatic small pressures and colour analysis by spectroscopy. The membranes change their colour in opposite directions for positive or negative pressures **Figure 4.11**. These membranes are also sensitive to the focus position, increasing or decreasing the reflected wavelength according the variation on the effective angle of incident. In this case, a Lambda change of ~90 nm was measured when applying $\pm 1\,kPa$ pressure on a membrane of 45 μm thickness and measuring close to the clamping region. Looking at **Figure 4.11**, a reduction on the peak intensity when applying positive pressures can be observed. This is probably due to the reflectance dependency on groove depth. When applying a positive pressure, a reduction on the groove depth would be produced, reducing as well the diffraction efficiency. On the other side, the diffraction efficiency is constant when applying negative pressures, where the deformation maintains the depth and shape of the grooves.
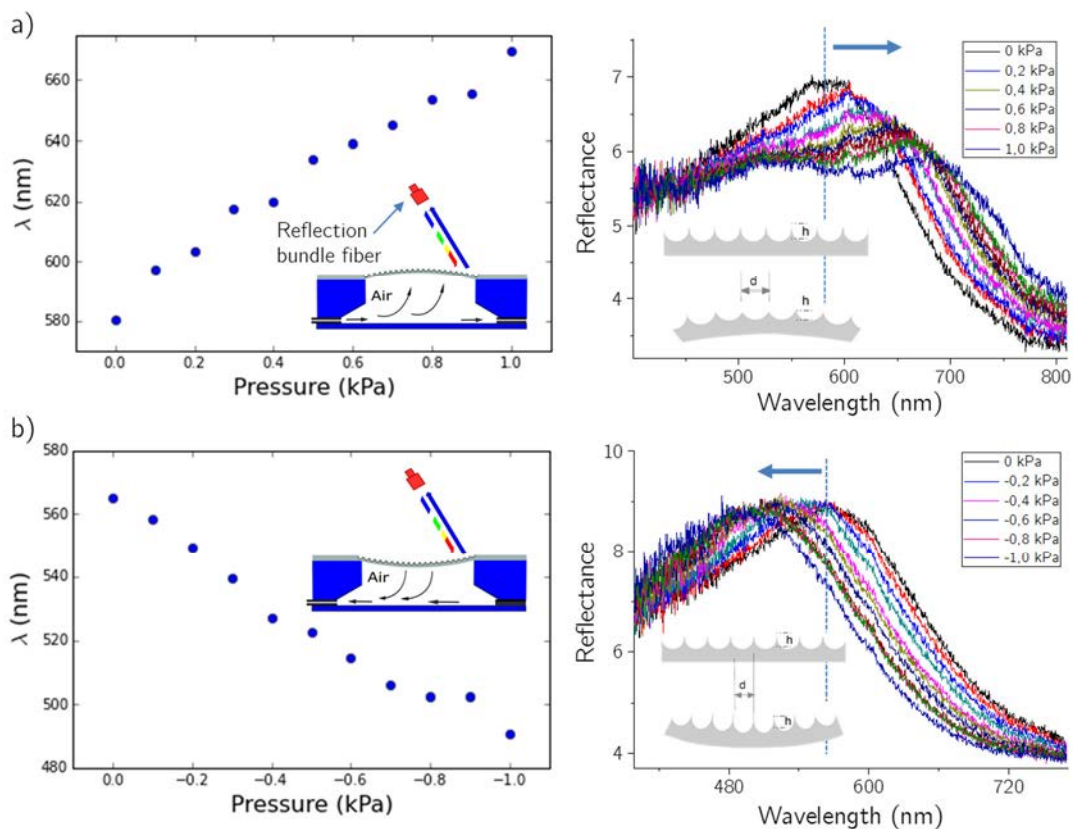
Figure 4.11. Characterization of inverse 2D membranes by applying small pneumatic pressures: a) membrane red-shifting wavelength for positive pressures, b) membrane blue-shifting for negative pressures; (inset a, b) membrane profile and light focus position during the measures.

The fabricated inverse 2D membranes are more sensitive than the 2D ones with embedded nanoparticles due to two main factors: possibility to fabricate thicknesses membranes without losing the nanoparticle order, and differences in the Young's modulus. The 2D Young's modulus is a combination of PDMS and polystyrene, in comparison with inverse 2D where the Young's modulus is given only by the PDMS. In consequence, the same pressure induced into 2D membranes will produce smaller deflections than into inverse 2D ones.

Due to the high sensitivity of inverse 2D membranes, a deeper optimization and characterization of this kind of membranes was done. Next chapter include a complete characterization and evaluation of an array of colorimetric membranes as a pressure sensor.

Chapter 5: Colorimetric array of nanostructured membranes as a pressure sensor for optofluidics applications

5.1 Introduction

The use of elastomeric materials, such as polydimethylsiloxane (PDMS), for the development of membrane-based optofluidic platforms has been widely reported in the literature [169] . An extended method for tuning membrane based optofluidic devices is through the internal gas or liquid pressure. For example, the fabrication of focus tunable lenses, by changing the membrane deformation, has become an extended method for the development of adaptive optics [170]–[172]. Different optical detection methods have been applied for measuring the integrated membrane deformation [173]–[175]. Song *et al.* propose the use of integrated optofluidic membrane interferometers to measure the on-chip microfluidic pressure and flow rate simultaneously, by analysing the interferometric patterns created [176]. Pressure-sensitive paints (PSP), which use luminescence emitted from air pressure-sensitive molecules, have been as well applied for the pressure detection in microfluidics [177]. As an example, pressure sensing inside microfluidic channels bonded to glass chips was achieved by integrating an oxygen sensitive luminescent sensor layer inside of an air-filled cavity [178]. Other approaches are based on the deformation of embedded optical microstructures (e.g. diffraction gratings), modifying the optical boundary conditions and how the lights interacts with it [179], [180]. In these cases, the optical detection schemes are mainly based on the diffraction of a transmitted laser beam and how the diffraction pattern change after deformation [181], [182].

In this chapter, I explore the white light diffraction on 2D nanostructured flexible photonic materials to achieve a power-free array of membranes that tune their reflective colour depending on the pneumatic or fluidic pressure inside a microfluidic channel. With this approach, the use of a high refractive index layer is avoided, simplifying the fabrication process and suppressing the effect of this layer on the stiffness of the membrane. 2D inverse colloidal photonic

structures were chosen because its colour dependency on the angle of incidence and reflection of the light, and its easy and low cost fabrication (transferable to wafer scale production). At the same time, unlike 1D grating whose colour depends on the detection angles (both polar and azimuth) under transverse electric or magnetic polarization, the colour of 2D gratings depends only on the polar angle, simplifying the alignment of the system, improving the reproducibility and reducing the error derived from the in-plane position of the device. Elastomeric nanostructured membranes were fabricated by infiltrating a close-packed layer of polystyrene nanoparticles with PDMS. The morphology, mechanical properties and colour tuning of the fabricated membranes were studied when exposed to bi-axial strains by applying pneumatic pressures. The suitability of white light interrogation to measure the fluid pressure is also demonstrated at the end of this chapter.

5.2   Platform design and working principle

The colour tuneable pressure sensing platform consists in an array of circular-clamped one-side nanostructured elastomeric (PDMS) membranes, integrated into microfluidics channels, as shown in **Figure 5.1a.** The working principle is based in the reflected colour change of the membranes, when illuminated with white light, under a uniform load stimulation [183].

The wavelength change during the membrane deformation has two main possible contributions, as shown in **Figure 5.1b i)** an increase in the nanostructures pitch, d, which would produce a red shift on the diffracted wavelength, and **ii)** a change in the angle of incidence and reflection of the white light $(\theta \pm \alpha)$, due to the curvature of the membrane, which would produce a red or blue shift of the wavelength depending on the position of the membrane and the direction of the mechanical deformation.

$2D$ inverse colloidal photonic nanostructuration was selected, instead of $3D$ photonic structures, for taking advantage of the associated angle change (due to the pressure induced membrane curvature) and maximize the shift in the reflected colour during the out-of-plane membrane deformation. $1D$ linear grating have the same sensitivity than $2D$ ones, but with a restriction in the

azimuth angle (angle in the membrane plane), being more critical the alignment of the light and the sample, and requiring more expensive fabrication process (top-down) especially for large fabrication areas. For $2D$ colloidal photonic structures, the incident diffracted light can be calculated from the planar grating equation [184] (equation (2.30) described in Chapter 2:). For a specific angle of incident and detection, the membranes will display a specific colour that can be easily measured by visual inspection or by using a camera (smartphone). Looking at the grating equation, the shift in the reflected colour during the out-of-plane membrane deformation can be maximized by measuring in Littrow configuration (equation (2.32)). For working in the visible range of the spectrum, colloidal spheres of $800\ nm$ and initial incidence angle of 30° were selected.

To increase the membrane deformation for a specific applied pressure, an elastomeric polymer such as PDMS was used for the fabrication of the membranes (low Young's modulus). The PDMS is a hyperelastic polymer (it supports large deformations without deteriorating), with good biocompatibility, non-porous to the liquids, nontoxic, optically transparent and easily fabricated. Some authors use an incompressible isotropic hyperelastic constitutive model (neo-Hookean) to describe the mechanical response of PDMS membranes [185]. However, for small loadings, the complex hyperelastic model can be replaced by a linear elastic model (equation (2.10),

$$P = \frac{16t^3 E}{3(1-v^2)a^4} w_0 + 4\frac{t\sigma_0}{a^2} w_0 + 2.43\frac{Et}{(1-v^2)a^4} w_0^3$$

where the behaviour and sensitivity of elastomeric membranes present a large dependency on the membrane thickness t. In the case of thick membranes (maximum deflection is much smaller than its thickness) the shape of the deflection is determined by the bending moments acting especially at the rim where the membrane is clamped. When the membrane is deflected, its neutral axis is stretched, generating some stress according to Hooke's law. For thin membranes (maximum deflection is larger than its thickness), the bending moments could be neglected, and the membrane deformation adopts a parabolic profile. A thick membrane would change its behaviour to a thin one as the pressure rises and the deflection is increased. In general, both bending

moments and stress could affect the membrane behaviour depending on the pressure applied.
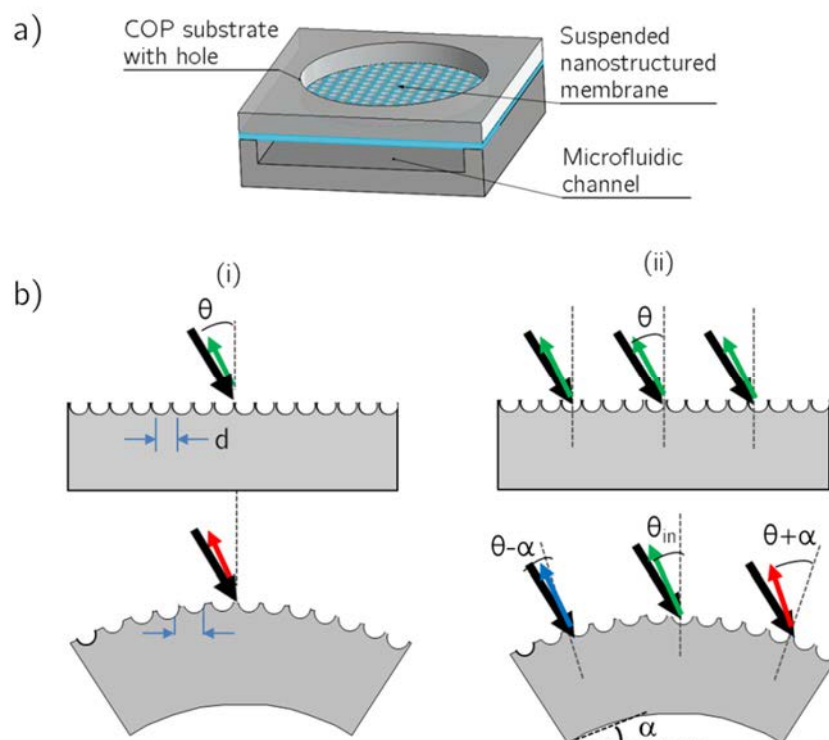
Figure 5.1. a) Scheme of the device ensemble, and b) schematics representation of the membrane bending and the two possible contributions to the change of the reflective colour.

5.3 Device fabrication

The pressure sensing platform was fabricated using a multilayer approach, as previously described in section 4.2. An initial one-side nanostructured elastomeric thin layer was prepared over a hard substrate (prepared using 2D CPhC as master moulds, as described in detail in **Chapter 3:**), (**Figure 5.2a**), which define the thickness of the suspended membranes. In this case, a PDMS thin layer of $50 \pm 2\,\mu m$ was prepared. Next, the elastomeric photonic thin layer was sandwiched between two substrates: one with perforated holes to define the suspended membranes dimensions (**1.5** mm in diameter), and another one with straight microfluidics channels (as shown in **Figure 5.2b**). Before peeling-off the one-side nanostructured PDMS layer, a PDMS substrate with the

microfluidic network was bonded to it. The ensemble was then peeled-off from the glass substrate, and the nanostructured side was bonded to a COP substrate with perforated holes that define the array of membranes. The membrane shape and size was designed using a computer aided design program (Vcarve). The PDMS microfluidic network were fabricated by master moulding, using SU8 master moulds fabricated by standard photolithographic process, and bonded to the nanostructured membrane by oxygen plasma treatment. The COP substrates ($188\mu m$ thickness) were prepared using rapid prototyping techniques (drilling and rasterization micromachining), and silanized with 3-(aminopropyl)triethoxysilane (AMPTS), previous to the bonding with the oxygen plasma treated photonic membrane. The integrated chip constituted of fifteen suspended membranes arranged in three independent channels.
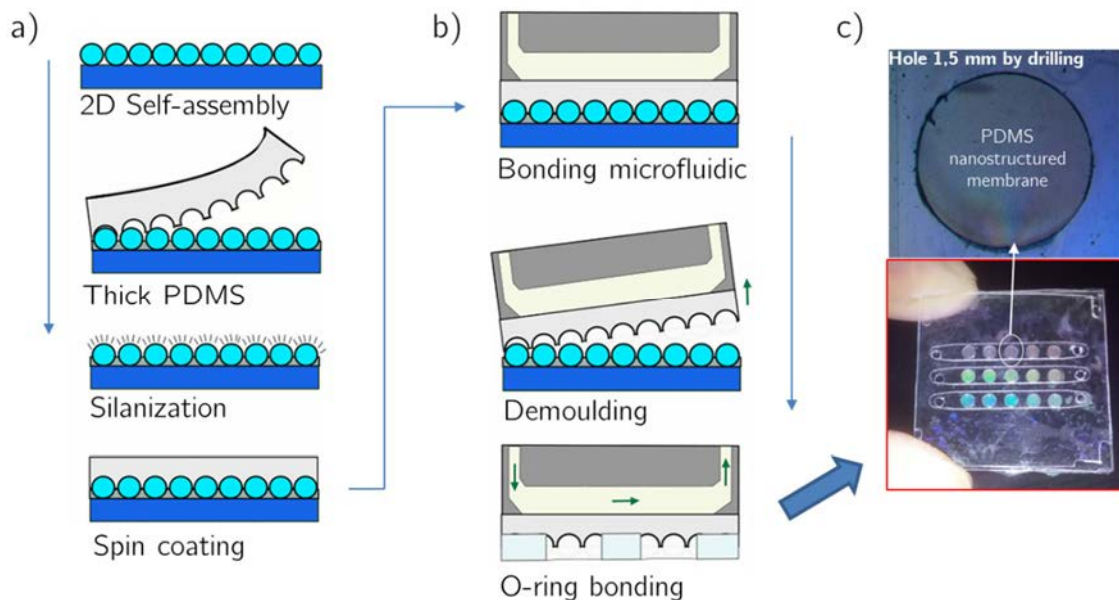
Figure 5.2. a) Schematic for INV-2D fabrication, b) chip integration by O_2 plasma bonding, c) (down) coloured array of membranes with microfluidic system, and (up) shape of individual membrane.

5.4   Characterization and Discussion

During the fabrication of the elastomeric photonic membranes, scanning electron microscopy (SEM) was used to evaluate the packaging of the self-assembled latex nanoparticles, the PDMS infiltration, and the voids left after the peeling process. **Figure 5.3b (right)** shows the high ordered 2D inverse

shape left into the PDMS after the peeling process which will work as diffractive surface with the ability to separate the different wavelengths of light. The bowl-shaped nanovoids have a mean diameter of $691 \pm 21 \, nm$, calculated from SEM images by using ImageJ software, and a height of about $320 \, nm$. The morphology characterization is explained in detail previously in section 3.3.3.1.

After the integration and packaging process, the final device is completely transparent, while the membranes exhibit a strong coloration at specific angles of diffraction, as shown in **Figure 5.3**. The lack of colour of the device out of the membranes is due to the squash of the nanostructures when bonded to the plastic substrate that supports them.
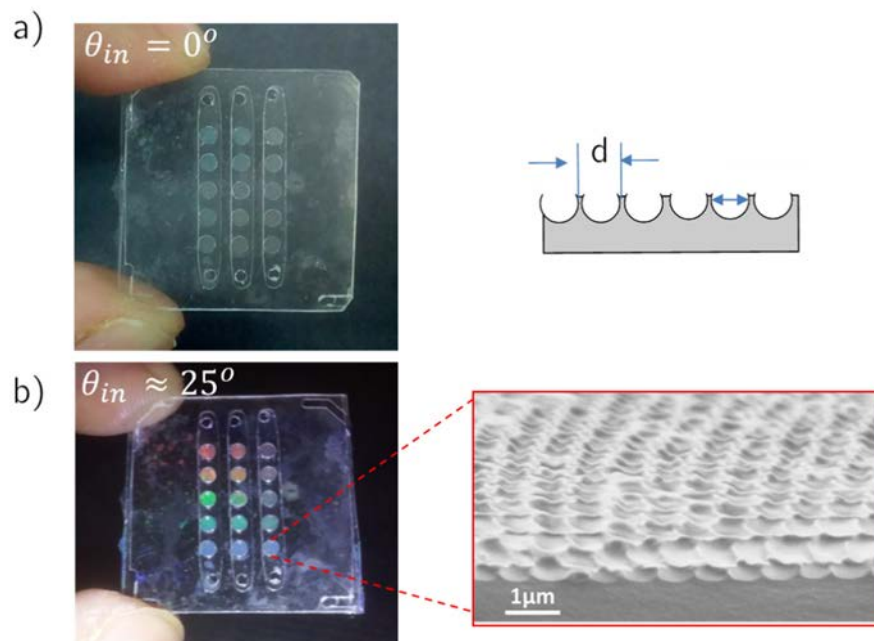
Figure 5.3. Photograph of the final integrated device at two different angles, a) $0\,^o$, b) $25\,^o$, and SEM images of the voids leaved on the PDMS.

5.4.1 Mechanical characterization of the membranes

The membranes behaviour under pneumatic deformations where experimentally characterized via confocal microscopy. **Figure 5.4** shows the measured deflection at the centre of the membrane for a range of pneumatic

pressures of $\pm 3\,kPa$, and the fitting to the theoretical membrane deflection model described by equation (2.10).

For a pressure range of $\pm 3\,KPa$, equation (2.10) fits well the experimental data, suggesting that the fabricated suspended membranes behave as a thin membrane for this range. Young's modulus and residual stress values of $1\,MPa$ and $0.02\,MPa$, respectively, were found from the fitting when considering a Poisson ratio of 0.5, membrane thickness of $50\,\mu m$ and membrane radio of $0.75\,mm$, which are in the range of the reported values for PDMS membranes [136]. In the low pressure range, between -1 and $1\,kPa$, the measured membrane deflection is smaller or in the order of the membrane thickness. In this case, the experimental data can be fitted to the first two terms of equation (2.10). For the same fixed conditions than before, the found Young's modulus and residual stress values were $1.3\,MPa$ and $0.02\,MPa$, respectively, in accordance with the values found when fitting to the whole equation. This behaviour suggests that for small loadings the use of the linear elastic model is suitable.
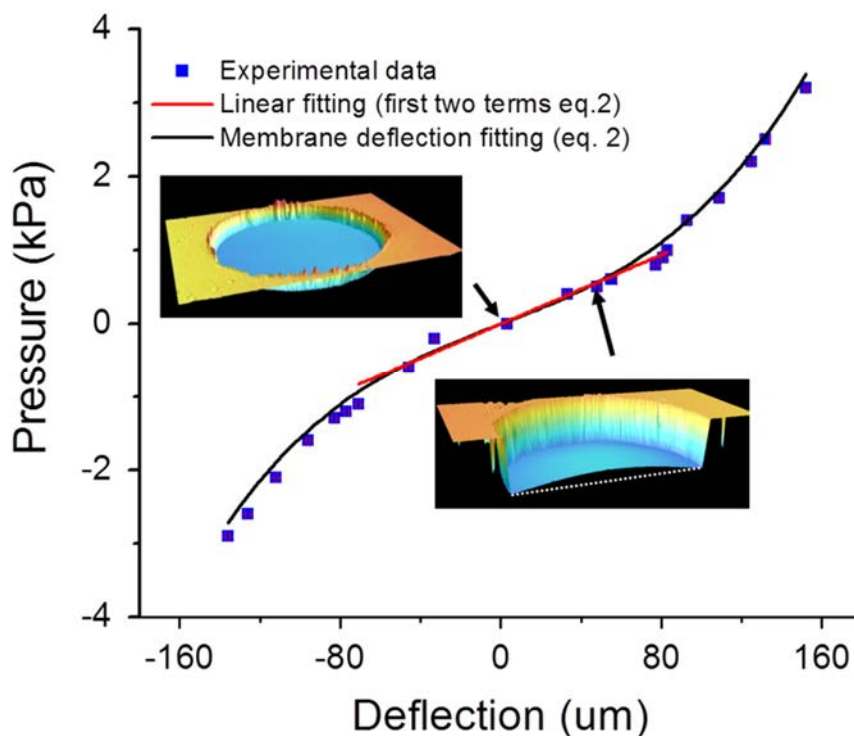
Figure 5.4. Pressure-deflection curve obtained by confocal microscopy for a $50\,\mu m$ thickness nanostructured membrane, and fitting of the experimental values to equation

(2.10) (in black, $R = 0.989$) and to the first two terms of equation (2.10), (in red, $R = 0.965$).

5.4.2 Membrane sensitivity characterization: position dependency.

UV-Visible reflection spectrometry was used to characterize the colour response of the photonic membranes by applying incremental constant pressures.

The colour response of the membrane under pressure deformations were analyzed for a low pressure range of $\pm 1\,kPa$, focusing at different positions of the membrane. **Figure 5.5** shows a scheme of the positions of focus analysed, and the pressure-wavelength curves obtained in each case. The maximum wavelength change is different depending on the region of focus, being higher when focusing near the border of the membrane, in positions 1 and 5, where the angle changes are larger. The minimum induced wavelength change was measured when focusing at the center of the membrane. In this position, the angle contribution to the wavelength change is smaller, but still not negligible due to the size of the spot, and the contribution of the period change.
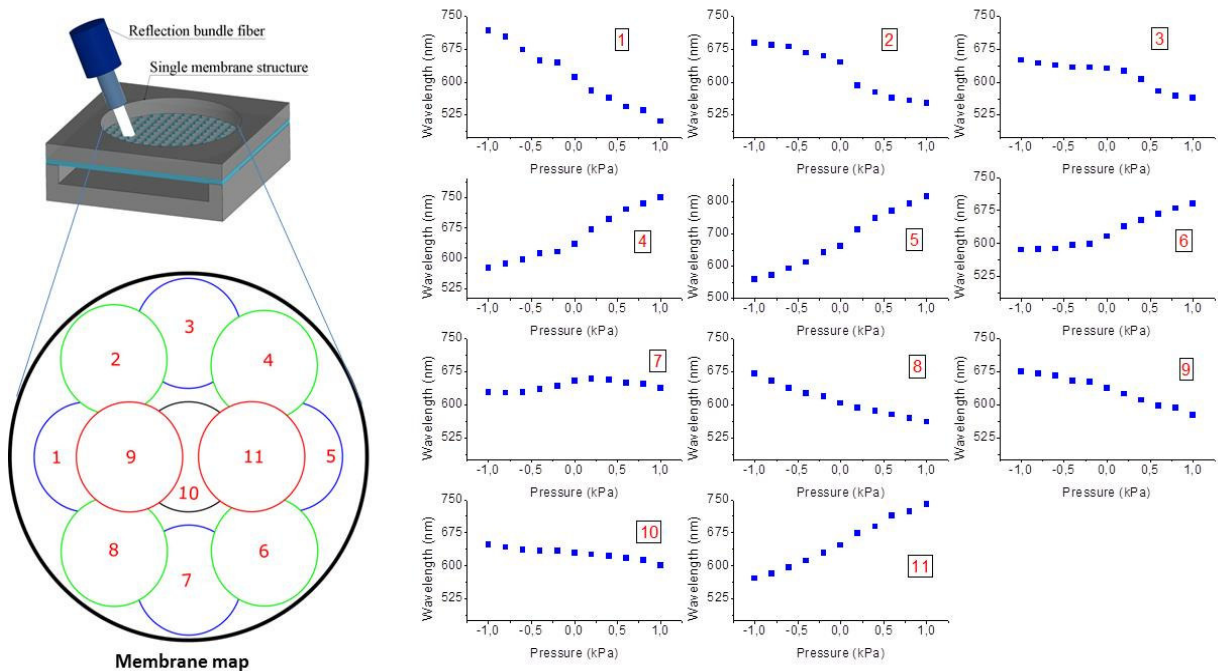
Figure 5.5 UV-Visible characterization curves performed at different positions of the membranes, for a range of pressure between $-1\,kPa$ and $1\,kPa$.

5.4.3 Pressure sensitivity analysis by UV-Visible spectroscopy

A customized UV-Visible set-up and custom software based in Python language [186] was developed to simultaneously monitor the spectra, find the wavelength peak and measure the pressure. The pressure sensing platform was mounted on a two dimensional lineal stage to select the membrane and the measurement position. Out-of-plane deformations (bi-axial strains) were produced in the membranes by a controlled pneumatic pressure injection into the microchannels. A pressure sensor (DP-101A-E-P), connected at the microchannel output, was used to measure the applied pressure. A syringe was used to control the pressure.

The diffracted colour was measured by using a bundle reflection probe in a Littrow configuration [187], with an angle between the probe and the normal to the membrane of 30°. At this configuration, the expected theoretical diffraction wavelength considering the mean pitch value of $745\,nm$ obtained from the SEM images is $645\,nm$. The experimentally measured diffracted colour of flat membranes was $647 \pm 4\,nm$, as shown in **Figure 5.5a**, in accordance with the expected theoretical value. If the membranes are initially buckled, a change in the reflection wavelength is expected depending on the position of focus, due to the dependency of the angle of incidence and reflection of the white light with the curvature of the membrane, as previously shown in **Figure 5.1b**. A scan of the probe along the membranes shows that the membranes are initially flat and do not suffer from initial bending. Similarly, the reflected measured wavelength would increase or decrease for positive pressures, depending on the position of focus in the membrane, and vice versa for negative pressures.

The colour response of the membranes under pressure deformations were analysed for a low pressure range of $\pm 1\,kPa$. The obtained spectral peaks when focusing close to the left border of the membrane are shown in **Figure 5.7d**. The small variations observed on the spectral intensity are due to changes

in the distance between the reflection probe and the membrane during the deformation process: negative pressures increases the probe-membrane distance (decreasing of the light collected by the reflection probe), while positive pressures reduce this distance. The photonic membranes show a linear behaviour (see **Figure 5.7e**) for the range of applied pressures (linear fitting with $R = 0988$). Maximum experimental wavelength change of $117\,nm$ was measured when applying $1\,kPa$ pressure. This maximum wavelength change is different depending on the region of focus, being higher when focusing close to the border of the membrane where the angle changes are larger as shown in **Figure 5.5**. This result suggest that the main contributor to the diffracted colour shift is the change of the membrane curvature (change in the effective angle of incident and reflection), as described in **Figure 5.3c**. For a fixed position of the fibre (close to the border), the devices show a long-term stability as shown in **Figure 5.6** .
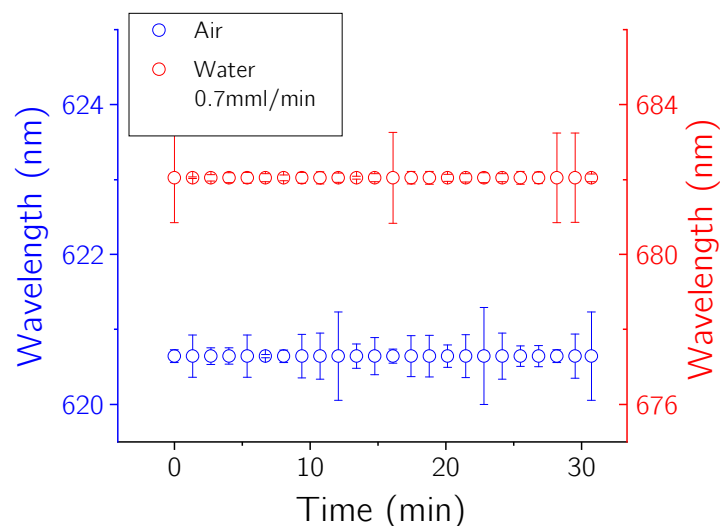
Figure 5.6. Long-term stability of our signal (mean value of 3 different measurements in different days), both in air and liquid at $0.7\,mmlmin^{-1}$.

In an independent series of experiments, the colour change produced when focusing in a flat nanostructured PDMS was measured by changing the angle of incidence (see **Figure 3.2a**). In this case, a linear colour change that fits the Littrow configuration equation (2.32) for a particle diameter of $720\,nm$ was obtained, which matches the values calculated from the SEM images. A mean shift of around $20\,nm$ per degree was found.

Analysing the membrane profile, the vertical displacement at the centre of the membrane is $83\,\mu m$ when applying $1\,kPa$ pressure (obtained from the confocal measurements from **Figure 5.4**), which corresponds to an angle change of $6.5\,^o$ measured close to the border of the membrane. Considering a wavelength change of $20\,nm/^o$, the estimated change in the reflected wavelength is $120\,nm$ when applying a pressure of $1\,kPa$, which is very close to the experimentally measured value ($117\,nm/kPa$). This confirms that the contribution from the nanostructure deformation is negligible respect to the contribution from the angle change, for the low pressure regime.

The sensitivity of the pressure sensor, S, can be defined as the slope of the relative wavelength change-pressure curve in **Figure 5.7e**: $S = \delta(\Delta\lambda/\lambda_0)/\delta P$, where $\Delta\lambda = \lambda_f - \lambda_0$, λ_f and λ_0 denote the wavelength with the applied pressure and the wavelength at cero pressure, respectively, and P denotes the applied pressure. The sensor shows a sensitivity of $0.17\,kPa^{-1}$ for the low pressure regime (-1 to $1\,kPa$). Higher sensitivities can be achieved by adjusting the diameter and thickness of the membrane. Considering only the elastic model (first term in equation (2.10)), larger deformations of the membrane would be obtained by increasing the ratio a^4/t^3.
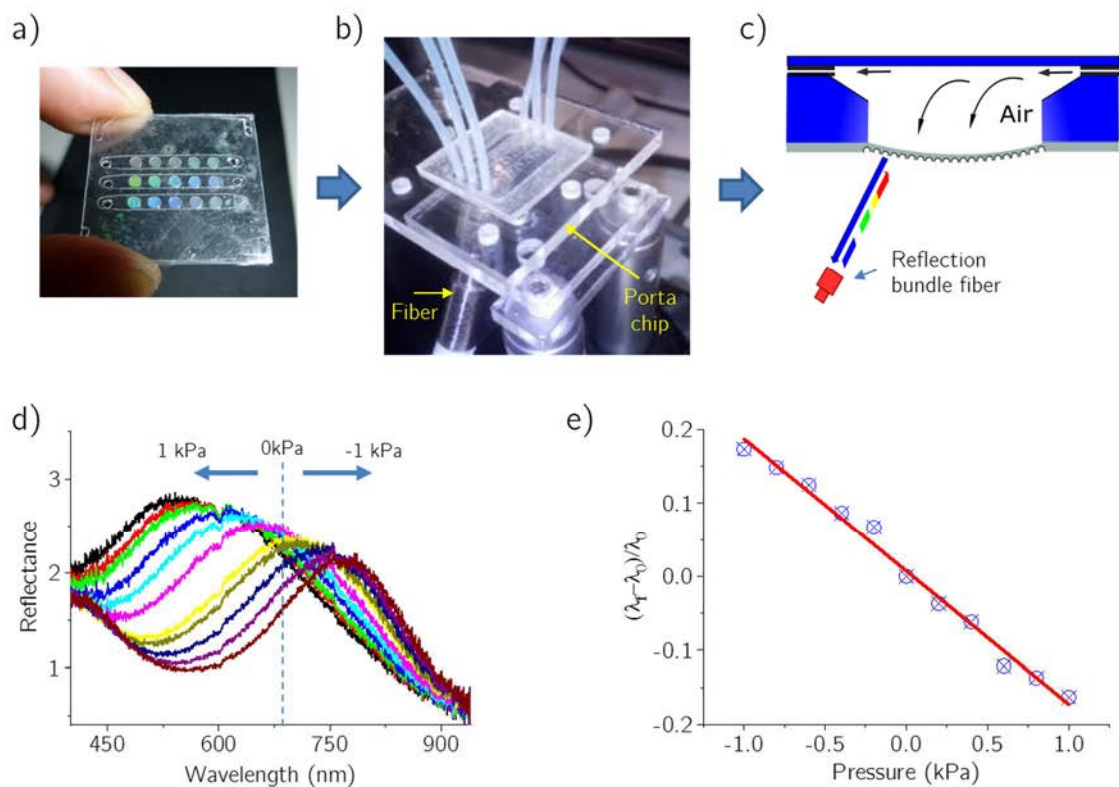
Figure 5.7. a-c) Photographs and scheme of the fabricated pressure sensing platform and experimental set-up for UV-Visible spectrometry, d) colour response of a single membrane for pressure ranges between $-1 \, kPa$ and $1 \, kPa$; e) calibration curve for positive and negative pressures (linear fitting with $slope = 0.17 \, KPa^{-1}$ and $R = 0.988$).

5.4.4 Membrane sensitivity analysis by flow rate

With the same channel configuration, the detection of the in-channel flow rates for different solutions was assessed. The pressure-flow characteristic of Newtonian incompressible fluid flow through a rigid rectangular microchannel with high aspect ratio (length/width) is given by Poisseuille's law: $\Delta P = 12\mu Q/h^3 w$, where ΔP is the pressure drop along the channel, Q is the flow rate, h and w are the length and width of the channel, respectively, and μ is the viscosity of the fluid. This relation shows the dependency of the pressure with the viscosity of the solution inside the channel. However, because of the low aspect ratio of our channels and the deformation of the membranes when injecting the flow, the relation between the pressure drop along the channel and the flow rate is not-linear, unlike the rigid channel. Several authors have propose different models (depending on the channels dimensions) to explain the non-linear behaviour of microfluidics channels with flexible walls, demonstrating smaller pressure drop for a specific flow velocity than in the case of rigid channels [188]. For example, Gervais *et al.*'s model for flexible microchannel demonstrated that the flow rate is a quartic polynomial of the pressure drop [189], while for Christov *et al.* the flow rate is a cubic polynomial of the pressure[159].

Experimentally, the chip was connected to a high precision syringe pump, which pumped the solutions through the channel at rates from 0 to $1 \, mmlmin^{-1}$. A scheme of the set-up configuration is shown in **Figure 5.8a**, where the commercial pressure sensor used to calibrate the system was connected between the syringe pump and the chip. Three water-glycerol solutions with different dynamic viscosity and density were prepared. The generated pressure increased non-linearly with the flow rate, and with the solution viscosity, as expected considering that the array of membranes inside the channel deform when applying a flow rate (**Figure 5.8b**). The experimentally

measured pressure is much lower than the expected from a rigid channel (dot curves in **Figure 5.8b**), in accordance with the behaviour of flexible channels [189]–[191] even though this models do not properly fit our experimental behaviour (data do not shown) due to the added complexity of having an array of flexible membranes along the rigid channel (instead of a continuous flexible wall). This non-linear behaviour is very clear when measuring the corresponding wavelength shift produced when increasing the flow rate and the fluid viscosity, due to the induced pressure change and the resultant deformation of the membrane (**Figure 5.8b**). In fact, the induced wavelength change increases with the flow rate following a third order polynomial. For flow rates larger than $0.3\ ml/mm$, which would produce pressures changes higher than $\pm 1\ kPa$, the wavelength-flow rate characteristic curve would exhibit a more complex relation due to the additional non-linear mechanical response of the membranes. For a specific flow rate, the wavelength change increases linearly with the fluid viscosity, and the viscous sensitivity increases for larger flow rates (shown in **Figure 5.8c**), as expected from Poisseuille's law and compliant PDMS channels models (higher viscosity produce higher pressure changes, and therefore in our case, higher membrane deformation).
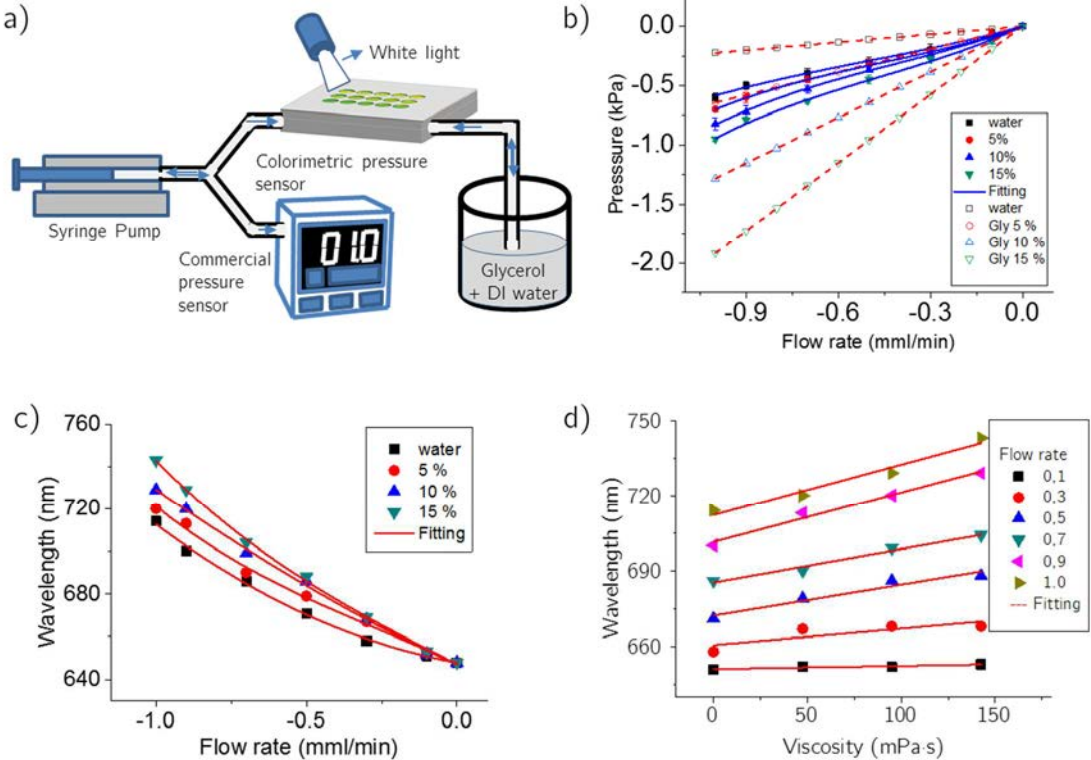
Figure 5.8. a) Scheme of the set-up configuration. b) Pressure-flow rate curve: experimental (continuous line) and theoretical expected values (dot lines) from Poisseuille's law (rigid channels). c) Wavelength-flow rate calibration curve for solutions with different percentage of glycerol (four different viscosities). d) Wavelength dependency with the fluid viscosity for different flow rates.

5.4.5 Image evaluation

5.4.5.1 Smartphone-based set-up for image acquisition

A prototype accessory was developed to convert a smartphone into a real-time imaging platform based on white light interrogation mechanism. The accessory was designed using a computer aided design program (Vcarve) and the different parts were fabricated out of black PMMA by laser engraving (Epilog Laser Mini 24). The accessory fixes the angle between the sensing platform and the smartphone to 30°. The smartphone flash LED is used as light source, illuminating the whole platform. Light reflecting off the pressure sensor surface is focused on the smartphone's camera sensor by an external plastic imaging lens ($focal\ length\ =\ 24\ mm$).

As a proof of concept, the chromatic response of the membranes under pressure stimulation was also evaluated by image colour analysis. **Figure 5.9a** shows a smartphone-based set-up developed to that effect. This methodology allows the simultaneous analysis of the whole array of membranes without the necessity of complex instrumentation. When applying an external pressure, the bending of the membrane produced a gradient of colours along the membrane (**Figure 5.9b**), due to the change on the effective angle of incidence and reflection of the light along the membrane profile, as previously observed by UV-Visible spectrometry.

Figure 5.9b shows a sequence of images of a single array of membranes inside a channel when applying different pressures. The membranes show a large colour change when applying low pressures (-1 to $1\ kPa$), displaying colours strips (blue, green yellow and red) that correspond to the reflected light at different parts of the membranes with different local surface angle as a consequence of the curvature, as schematized in **Figure 5.9c**. A blue-shift and

red-shift is shown depending on the side of the membrane (named as up or down in **Figure 5.9b**) respect to the central part, where there is no effect of the curvature on the angle of incidence or reflection. Positive pressures produce an inflation of the membranes, as shown in **Figure 5.9c**. In this case, the bottom half of the membrane have incidence and reflected angles (respect to the normal to the membrane surface) that are smaller than the initial angle of $30°$ (respect to the flat membrane), which produce a blue-shift of the reflected colour. In opposition, the upper half of the membrane presents an increase in the incident and reflected angle, producing a shift towards infrared values which are filtered-out in our conventional phone camera. When applying negative pressures, the behaviour is the contrary, showing the blue-shift in the upper half of the membrane. It can be observed that pressures change of $0.2\ kPa$ are clearly distinguishable by naked eye.
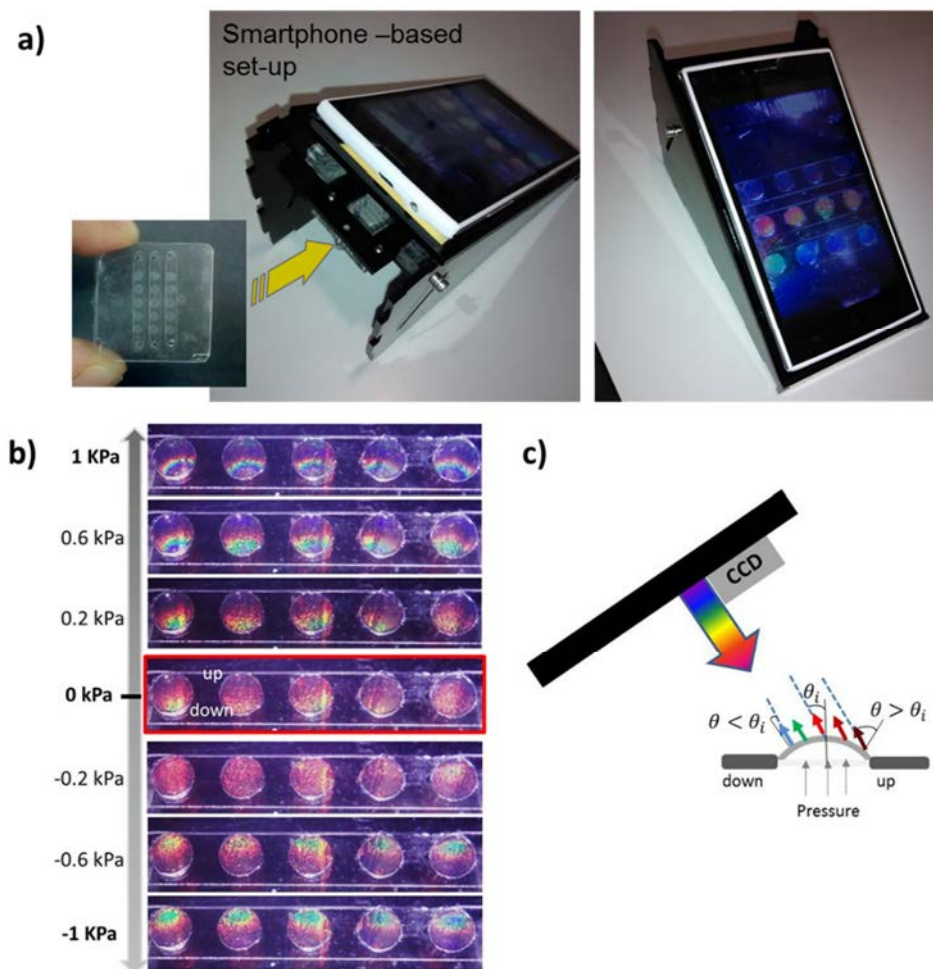

Figure 5.9. a) Smartphone-based image acquisition set-up. b) Sequential images acquired for a range of applied pressures ($-1kPa$ to $1kPa$). c) Image set-up scheme showing the angle change during membrane deformation and the associated colour pattern along the membrane profile.

Chapter 6: Surface-stress colorimetric sensors based in cantilevers.

6.1 Introduction

Surface stress sensors have been widely reported for many applications including detection of conformational changes of molecules, swelling, changes in temperature, or photo actuation [31], [192], [193]. Photothermal bimorph actuators have been used for many applications, including actuation [194], soft robotics [195], light mills [196], and frequency switches [197]. The photo-sensitive material absorbs a specific or a broad spectrum of light and convert it to heat, producing a thermal expansion of the materials and a induced deformation [196]. Among the different photo sensitive materials used, molecules that support photoinduced molecular conformational changes is one of them. These materials allow the conversion of photoinduced effects at the nano scale into macroscopic deformation including bending, expansion, contraction, twisting, or rotation depending of the photostructural design and molecular photoreactions. Derivatives of azobenzene have been historically used to undergo photoisomerization and these have been widely studied as efficient photoisomers [198], [199]. Azobenzene and its derivatives undergo trans-cis isomerization upon UV irradiation, and cis-trans back isomerization by visible light irradiation producing large molecular conformation changes. Taking advantage of the isomerisation process, azobenzene derivatives has been used for many application including photo-control of biological systems [198], photomechanically responsive materials [200], [201], [32], [202], [203], and microfluidics [204], [205], among others.

In this chapter, I describe a theoretical study of a surface stress colorimetric nanomechanical sensor based in cantilevers and demonstrate its performance for the detection of photo-induced molecular conformational changes. In this sensor, a diffraction grating is designed into one microcantilever surface, to produce a change in coloration when the cantilever deflects (acting as detection surface). With this focus, I analyse the colorimetric method (capabilities and limitations) when the cantilever deflects by surface stress. In the same way, the search of the optimum transducers parameters to maximize

both the mechanical response and the colour change associated is included. Parameters such as thickness of cantilevers, materials Young's modulus, dimensions, refractive index, and pitch size of diffraction grating play an important role in the improvement of sensitivity of cantilevers. In the final part of this chapter, the cantilever colour changes due to the surface stress produced by a thin layer of photosensitive molecules disposed on the cantilever flat surface is analysed depending on the power of light.

6.2 Working principle and sensor design

The working principle of a colorimetric sensor is based on the sensor – cantilever- structural coloration change associated to the cantilever bending induced by surface stress changes (i.e. during biorecognition processes). The mechanochromic cantilever (MC) consists on a one-side periodically nanostructured suspended material layer, fixed at one end (as shown in **Figure 6.1**). The periodic nanostructuration works as 1D or 2D diffraction grating, producing a structural coloration of the cantilever under white light illumination (**Figure 6.1a**). The structural coloration observed depends on the grating pitch, and the angles of incidence and diffraction of the light. Changes in the cantilever curvature produce a change in the coloration observed, especially at the cantilever free end, being possible to detect the cantilever displacement generated by changes in the cantilever surface stress by analysing the structural colour by image analysis. The main advantage of this approach is the capability to detect many transducers by using a single while light source and a single camera (i.e. smartphone).
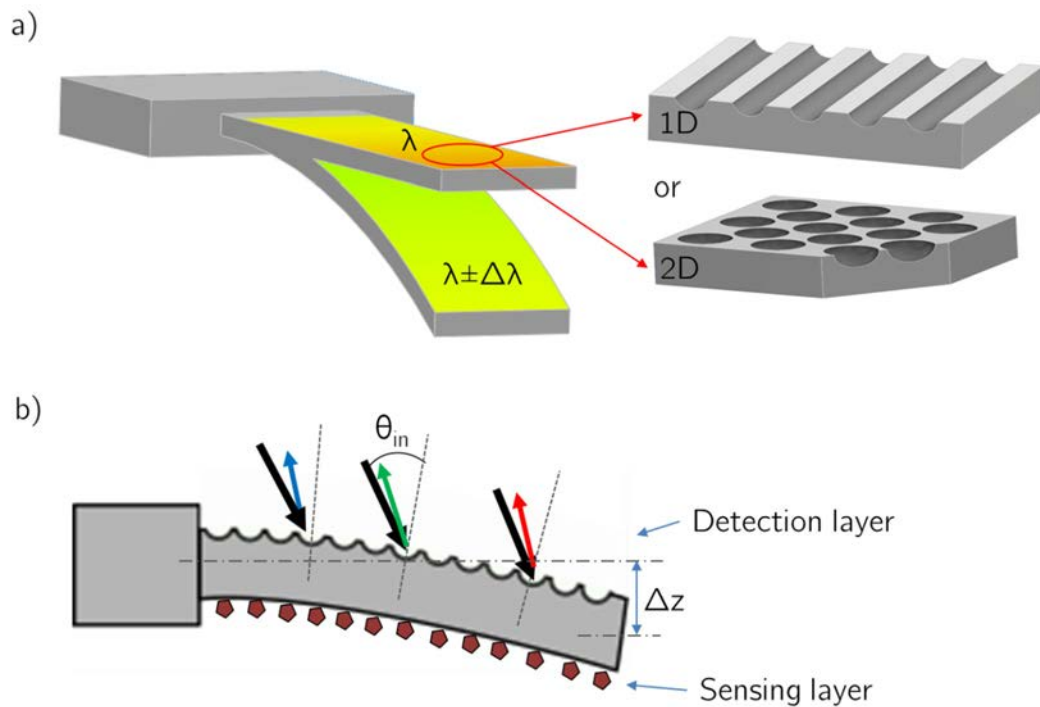
Figure 6.1 Working principle of surface stress colorimetric cantilevers: a) changes in cantilever coloration due to the system curvature (nanostructure can be 1D or 2D diffraction gratings), b) lateral profile of nanostructured cantilever under bending by the action of surface stress induced in the sensing layer.

6.2.1 Materials: optomechanical properties for cantilevers development.

Silicon-based materials have been historically used for cantilever fabrication for their optical and mechanical properties. With aim of development a low-cost sensor, the main drawback of silicon materials based cantilevers is the cost of the material and the needed of microfabrication processes, which increase the total cost. Polymeric materials offer a good alternative to develop low-cost cantilevers based sensors. Due to the high Young's modulus of silicon based cantilever, the deflection reported are in the nanometric order. On the other hand, polymeric materials offer a wide possibility to be used to fabricate cantilevers in different sizes and thicknesses. The low Young's modulus of polymeric materials compared with silicon-based materials allows to increase the bending's to micrometric orders. Polymeric materials, besides being cheap are easily nanostructured (Demonstrated in Chapter 3:). In comparison to their low cost and good mechanical performance,

the polymeric materials exhibit refractive indexes (η) below 2, which reduce their applicability for some optical applications where high refractive index contrasts are required. Diffraction of white light can be achieved by using a nanostructured polymeric material in air ($\eta_{air} = 1$), or even in water ($\eta_{water} = 1.33$) for materials with $\eta_{water} < \eta > \eta_{air}$. Higher refractive indexes are preferred to increase the index contrast and increase the diffraction efficiency. **Table 6.1** shows the Young's modulus and refractive index of potential materials to develop nanostructured cantilevers.

Material	E (Pa)	η
PDMS	1.8×10^6	1.41
Polyimide	2.5×10^9	1.70
PMMA	3.0×10^9	1.49
PS	3.4×10^9	1.57
PEEK	3.6×10^9	1.70
SU-8	6.0×10^9	1.59
Silicon	1.79×10^{11}	3.97

Table 6.1 Materials Young's modulus (E), and refractive index (η).

6.2.2 Optomechanical transduction

During a biosensing assay, the target molecules interact with the receptor film (antibodies, probe DNA, polymers, metal film, etc.) deposited over one side of the cantilever structure, generating a surface stress induced bending of the cantilever free end. The origin of this local stress is owed to the cantilever surface reconstruction due to: the covalent bonding of surface atoms and the linker molecule, intermolecular forces between absorbed molecules (van der Waals, steric hindrance, hydrogen bonding or electrostatic), configurational entropy or change of electronic charge density, etc. The resulting surface stress can be compressive or tensile, depending on the surface energy. The relation between the surface stress and the resulting cantilever bending is described using Stoney's equation (Eq.(2.9) described in section 2.2). The resulting cantilever bending, and therefore the cantilever sensitivity to detect surface stress changes associated to molecular adsorption depends on the cantilever material and shape.

For the case of a nanostructured cantilever, the diffracted light from each corrugation of a diffraction grating interfere constructively for a set of discrete angles for a given spacing, d, between corrugations, represented by the grating equation (eq. (2.30), described in section 2.4.1). Another property of the polymeric materials, not mentioned before, is their transparency. The high transparency of polymers makes them ideal for working in the transmission configuration, reducing the reflected percentage of light. For that reason, both transmission and reflection diffraction, are studied in this section. Following the grating equation, either for reflection or transmission, the algebraic signs of the two angles differ if they are measured from opposite sides of the grating normal. A particular case is that in which the light is diffracted back toward the direction from which it came, Littrow configuration (Equation (2.32), described in section 2.4.1).

For a particular set of values of d, and the angles θ and β, the grating equation is satisfied by more than one wavelength. For that reason, white light striking the grating is decomposed into its component colours, being each colour diffracted along different direction in such a way that shorter wavelengths exit with an angle closer to the normal than longer ones (**Figure 6.5**). The observed colour would therefore depend on the corrugation pitch, angle of incidence of the light, and the observer distance and position from the grating, due to the angular dispersion of the diffracted light.

When considering the grating on top of the cantilever surface, the observed colour will be affected by the cantilever curvature radio, which induces a change in the effective angle of incidence and diffraction of the light respect to the normal to the cantilever surface. The grating equation (Eq. (2.30)) is modified as:

$$m\lambda = d\big(sen(\theta + \alpha) + sen(\beta + \alpha)\big) \qquad (6.1)$$

where α is the angle deflected by the cantilever free end, which can be positive or negative depending of the tensile or compressive generated stress. **Figure 6.2** shows the different light diffraction-cantilever for **reflection configuration** and sign convention for a cantilever under bending.
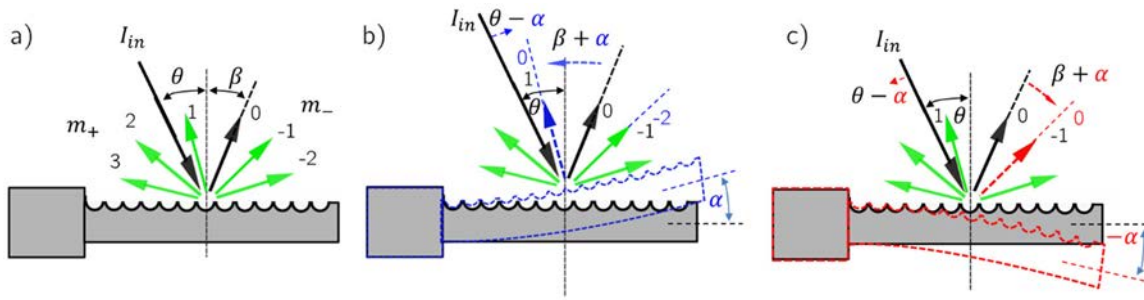
Figure 6.2 Diffraction of nanostructured cantilever for an incident angle θ, and diffracted angle β, in reflection: a) unstressed cantilever, b) sensing layer under tensile stress (positive deflection), c) sensing layer under compressive stress (negative deflection).

For positive and negative deflections (**Figure 6.2bc)**, the specular order m_0 and m_{th} diffracted orders shift by twice the α angle.

In the case of **transmission** (**Figure 6.3**), the specular order m_0 goes straight through the grating surface and it is not affected by α angles. Since higher orders of diffraction follow the m_0 order, the m_{th} order of diffraction is almost unaffected when the cantilever is under bending at $\pm\alpha$ angles for positive and negative deflections.
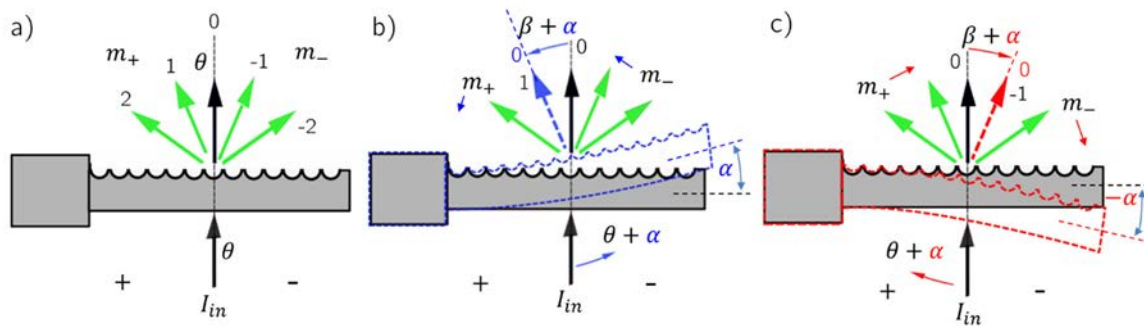
Figure 6.3 Cantilever in transmission: a) diffraction orders for an unstressed cantilever, b) shift anticlockwise m_{th} orders for tensile stress, c) shift clockwise m_{th} orders for compressive stress.

Analysing the relationship between deflection and surface stress, the equation (2.8) can be modified to represent the α angle changes as $\alpha = 2\Delta z/L$. Including this expression in the modified grating equation (Eq. (6.1)), the

expression used to calculate the colour change due to surface stress can be expressed by:

$$m\lambda = d\big(sen(\theta + 2\Delta z/L) + sen(\beta + 2\Delta z/L)\big) \qquad (6.2)$$

where Δz can be calculated by Stoney's equation (Eq. (2.4)) including the sign convention for reflection and transmission configuration.

In the case of **Littrow-configuration**, the orders shift is similar to the reflection case. In this case, the limit of Litrow-configuration occurs when $\theta_L = \alpha$ for positive deflections. In the case of negative deflections, when the α angle exceeds the first order angle range, an overlapping with m_{th+1} would be produced.

For cantilevers based on 1D or 2D diffraction gratings (**Figure 6.1**), the Littrow-configuration would satisfy the condition at different angles (Section 2.4.1.3) due to the round groove shape. With this assumption, it's possible to achieve a uniform shift in coloration at different α angles with a minimum intensity change (**Figure 3.13a**).
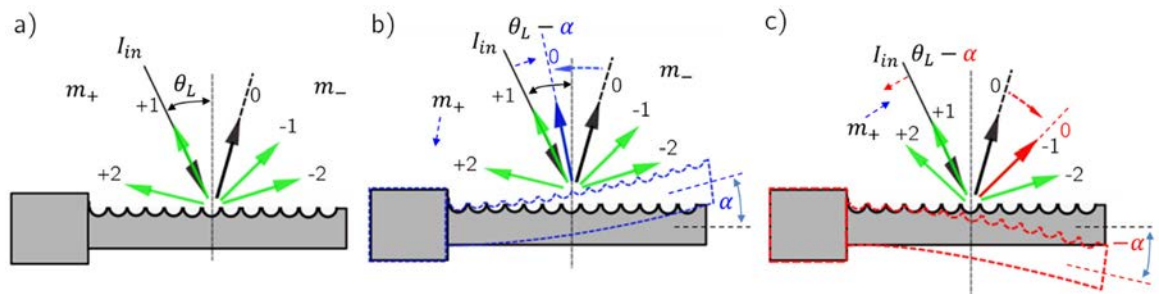
Figure 6.4 Cantilever in Littrow-configuration, a) m_{th} diffraction orders for unstressed cantilever, b) m_{th} shift by tensile stress and, c) compressive stress.

The expression used to calculate the colour change associated to the cantilever deflection for Littrow configuration is derived from the modified equation (6.2) and summarized as follow:

$$m\lambda = 2d\big(sen(\theta_L \pm 2\Delta z/L)\big) \qquad (6.3)$$

Where the sign is defined by α for positive or negative deflections (**Figure 6.4bc**).

6.3 Cantilever colour change by surface stress: Analytical study

6.3.1 Grating spacing dependence

According to the main diffraction equation, the colour change associated to the cantilever bending depends directly of the grating spacing. In this way, for higher values of d, small changes of θ are required to achieve larger changes in colour under the visible band. **Figure 6.5** shows the spectra calculated for d values from $400\ nm$ to $1600\ nm$ for Littrow configuration. A range of values of d and θ_L are valid to achieve a reflected wavelength in the visible range of the spectrum. Increasing the grating spacing force to work at smaller angles, which could be a limitation to set-up the image detention system (cameras and light source).
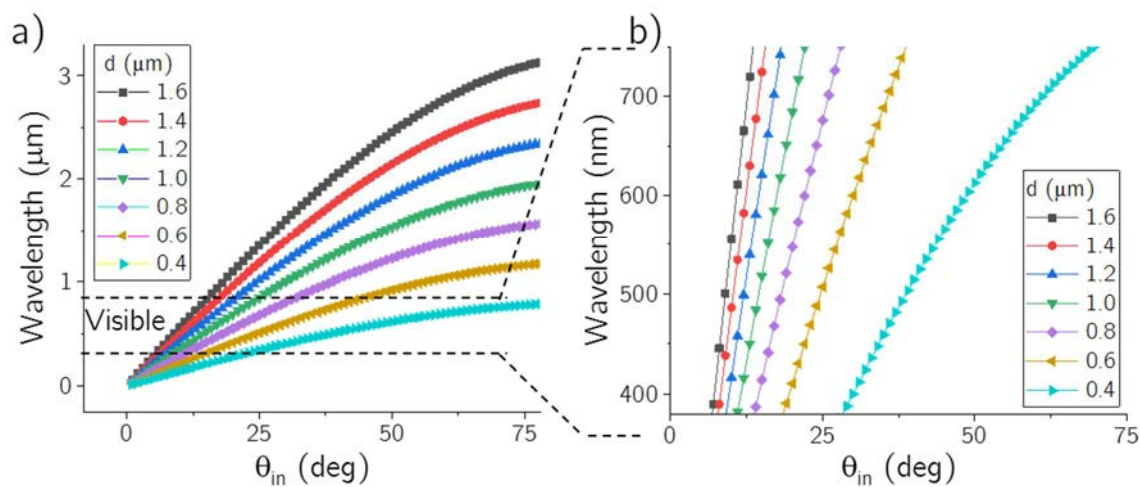
Figure 6.5 Spectra calculated for 1D-grating in Littrow configuration for grating spacing, d, from $0.4\mu m$ to $1.6\ \mu m$, and incident angles from $0\ ^o$ to $75\ ^o$, a) visible range section, b) zoom of the visible range, (shorter wavelengths exit with an angle closer to the normal than longer ones).

6.3.2 Mechanical bending

According to Stoney's equation. the cantilever deflection (Δz) increase for higher length (L) to thickness (h) ratio. The expected cantilever deflection for different materials and L/h ratio is represented in **Figure 6.6a** by assuming a surface stress change of $0.1\,N/m$. In the case of PDMS cantilevers, higher deflections are achieved due to its low Young's modulus in comparison with other polymers and silicon materials (**Table 6.1**). However, PDMS is an elastomeric material difficult to manipulate to fabricate suspended structures with a high aspect ratio. In opposition, other polymers such as SU-8 or polyimide allows the fabrication of very thing and long structures, which make possible the fabrication of cantilevers with similar sensitivity to PDMS cantilevers. **Figure 6.6b** shows the cantilever deflection of different polymers and PDMS for two L/h ratios, **3000** and **100** respectively. A referential range of surface stress from $10\,mN/m$ to $1\,N/m$ was used to calculate the deflection (the referential range was obtained from surface stress measured by biosensors based on cantilever [206]–[208]).
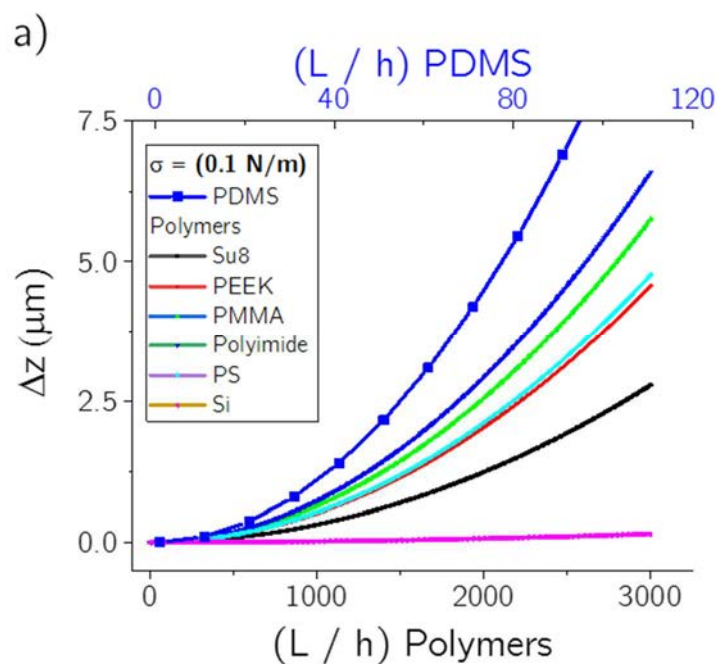
b)
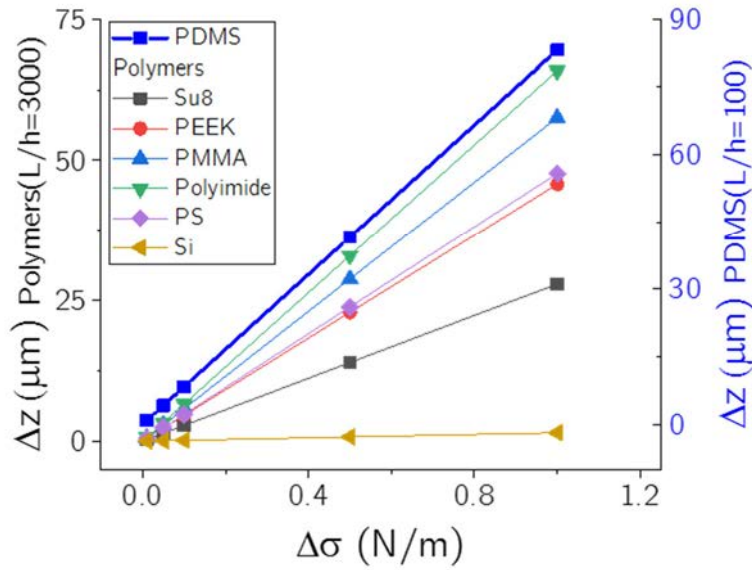
Figure 6.6 a) Cantilever deflections considering a surface stress $\sigma = 0.1 \, N/m$. b) Detection limits for a fixed L/h ratio ($L/h = 100$, PDMS, and $L/h = 3000$, polymers and silicon), and different σ. The cantilever deflection increase proportionally as surface stress increase.

For a PDMS cantilever with $L = 1500 \mu m$ and $h = 20 \, \mu m$, the length and thickness relation will be $L/h = 75$. For a surface stress $\sigma \approx 0.1 \, N/m$ [207], the deflection of the cantilever will be $\Delta z = 4.8 \, \mu m$. In order to achieve a similar deflection with other polymers, the relation L/h should be much higher. As example, L/h will be around **2571** for polyimide cantilevers. This relation represents to have a cantilever with $L = 1500 \, \mu m$ and $h = 0.6 \, \mu m$, which is technological limited for polyimide.

6.3.3 Colour change

The colour change associated to the deflections induced by surface stress changes showed previously in **Figure 6.6** was calculated for silicon, PDMS, and polymeric nanostructured cantilevers. For this propose, the angles θ and β where fixed leaving free α as a surface stress depended variable. The grating spacing d was fixed to $1600 \, nm$ expecting to have high $\Delta\lambda$ for small angle

changes (see the grating spacing dependence in **Figure 6.5**). $\Delta\lambda$ was calculated for a range of L/h values taking the maximum value for polymers and silicon $L/h = 1500$, and $L/h = 50$ for PDMS.

The relation $L/h = 1500$, can be the equivalence to have a cantilever with $1500\,\mu m$ and $1\,\mu m$ for length and thickness respectively. For PDMS, the relation $L/h = 50$ would be the equivalence to $L = 1500$ and $h = 30\,\mu m$. This thickness can be easily achieved by spin-coating process.

Reflection configuration

Figure 6.7 shows the change in colour associated to positive deflections measured in reflection configuration for a grating pitch of $1600\,nm$. In this case, the angle of incident light was fixed to $\theta = 20\,^o$, the outer diffraction angle to $\beta = 0^o$, and the angle α was calculated from the deflections Δz showed in **Figure 6.6**. For this angle configuration, the initial colour for an unstressed cantilever is $\lambda = 547\,\text{nm}$. Using the equation (6.2), the $\Delta\lambda$ was calculated taking into account the sign convention.
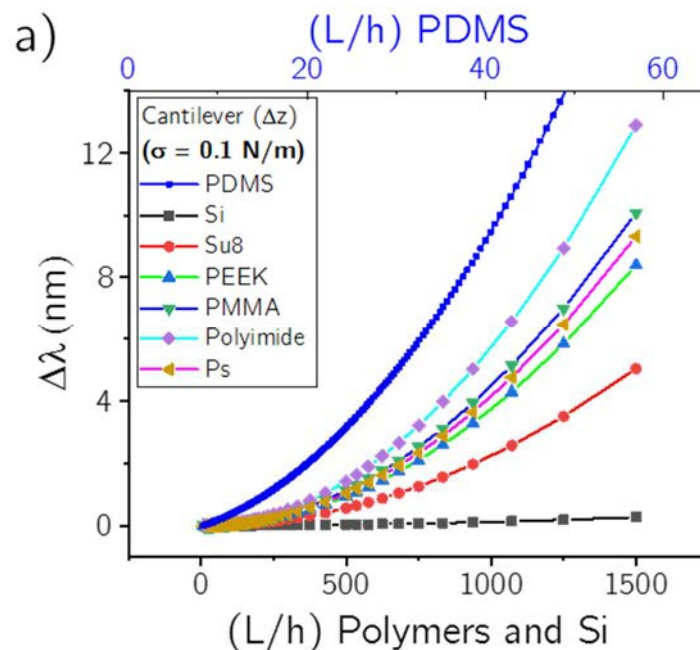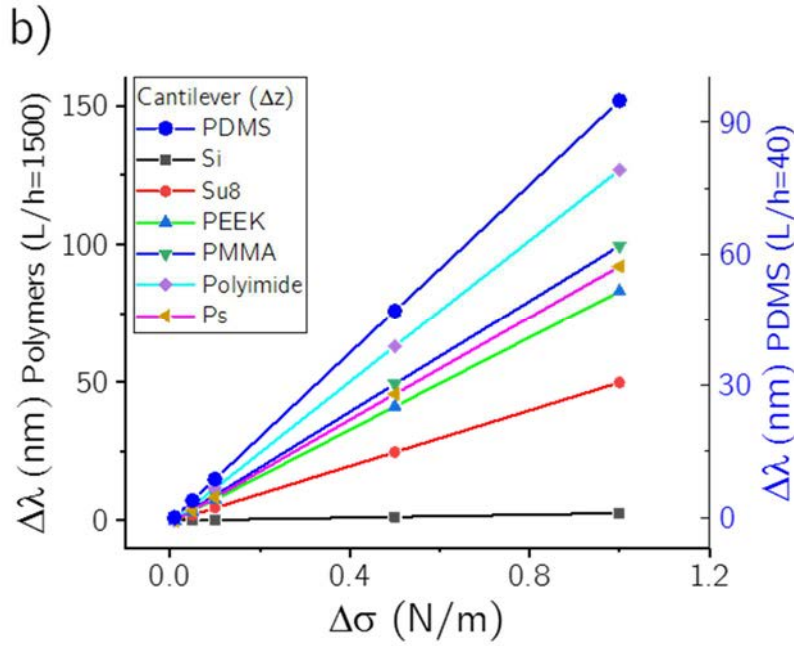
Figure 6.7 a) Colour change associated to $\sigma = 0.1\,N/m$ for polymers, silicon and PDMS, b) colour change calculated for a referential surface stress range; from $10\,mN/m$ to $1\,N/m$.

For L/h from 0 to 1500, the $\Delta\lambda$ calculated for cantilever deflections gives a colour change from $5nm$ for SU-8 to $12\,nm$ in the case of PMMA. For PDMS cantilevers, the colour change reaches $14\,nm$ for L/h from 0 to 50, and for silicon less than $1nm$ (**Figure 6.7a**). Larger surface stress changes would produce higher colour changes (**Figure 6.7b**). For $\sigma = 1\,N/m$, the $\Delta\lambda$ reaches $50\,nm$ for SU-8 and $126\,nm$ for PMMA, $2{,}6\,nm$ for silicon, and $94\,nm$ for PDMS.

Transmission configuration

For transmission configuration, the colour associated to deflections are calculated for positive deflections. Again, the equation (6.2) was used taking into account the sign convention.

In this case, the angle of incident light was fixed to $\theta = 0^{o}$, and the outer diffraction angle to $\beta = 20^{o}$. For this angle configuration, the diffracted

wavelength is $547\ nm$ for an unstressed cantilever. From this initial wavelength, the colour change is close to $1\ nm$ for a surface stress of $0.1\ N/m$ in the case of polymers and PDMS cantilevers as shown in **Figure 6.8a**.

By increasing the surface stress until $1\ N/m$, the $\Delta\lambda$ reaches values from $4nm$ to $10\ nm$ in the case of polymers, and $12\ nm$ for PDMS cantilevers as sown in **Figure 6.8b**. These small changes in coloration satisfy the condition for transmission configuration, where the diffraction is minimally affected by the cantilever deflections.
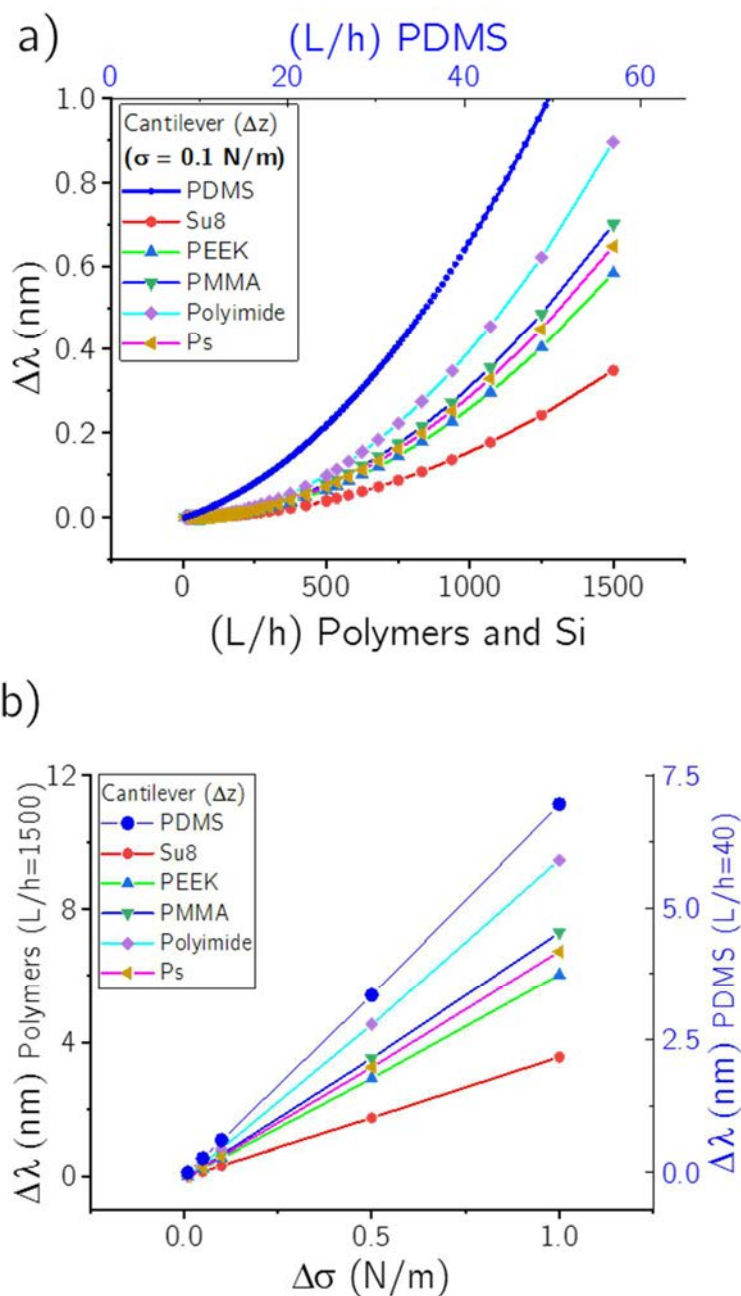
Figure 6.8 Colour change in transmission configuration for: a) $\sigma = 0.1\,N/m$, b) from $10\,mN/m$ to $1\,N/m$. (Silicon cantilever is not included in this calculation due to its low transparency).

Littrow configuration

For the case of Littrow configuration, θ_L was fixed at 10°. Using the equation (6.3), changes in coloration associated to positive deflections were calculated. The initial λ calculated for an unstressed cantilever was $555\,nm$. The $\Delta\lambda$ calculated for a surface stress of $0.1\,N/m$ where from $5\,nm$ to $14\,nm$ for polymers, and $15\,nm$ for PDMS cantilever. For silicon-based cantilever $\Delta\lambda$ is less than $1nm$ (**Figure 6.9a**). For $\sigma = 1\,N/m$, the colour change calculated was from $50\,nm$ to $130\,nm$ for polymers and $97\,nm$ for PDMS cantilevers. In the case of silicon-based cantilever the calculated $\Delta\lambda$ was $2\,nm$ (**Figure 6.9b**).
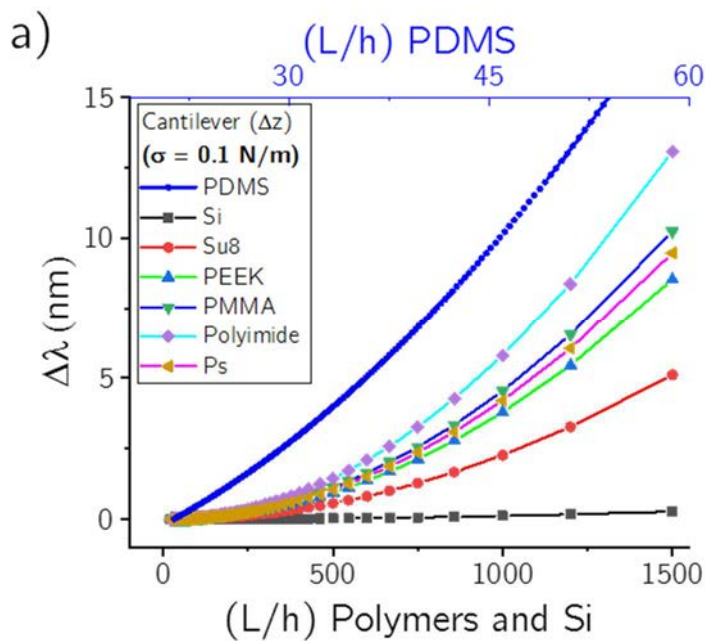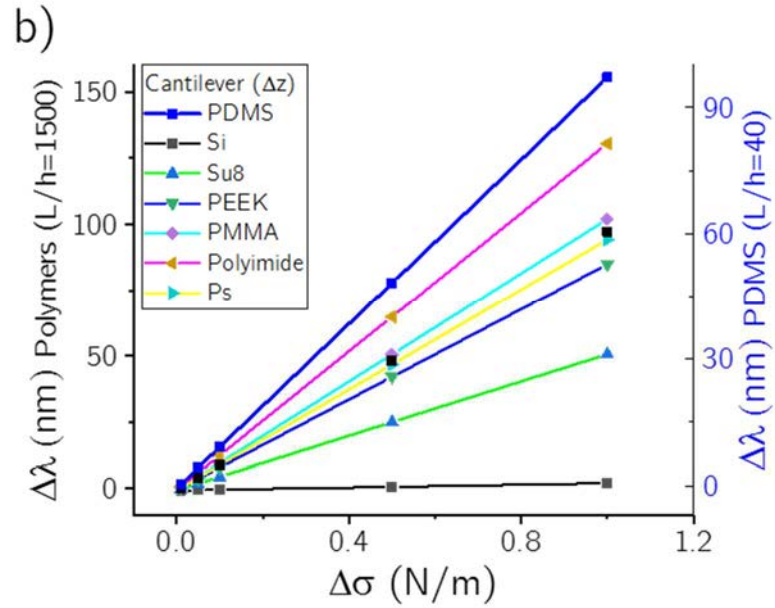
Figure 6.9 Colour change for polymeric and PDMS cantilevers in Littrow configuration, a) $\sigma = 0.1\,N/m$, b) from $10\,mN/m$ to $1\,N/m$. (Silicon cantilever is included for comparison proposes).

According to the **Figure 6.10**, for a PDMS cantilever with $L/h = 40$, subjected to $\sigma = 1\,N/m$, the calculated deflection angle is $\alpha = 1.8^o$. This small angular change produces a change in colour of $94\,nm$ for reflection, $96\,nm$ for Littrow configuration, and $7\,nm$ for transmission. Reflection and Littrow configuration have a small difference in colour sensitivity. For transmission configuration, the change in α by surface stress produces a minimum colour change in comparison with reflection and Littrow configuration in first order m_1.
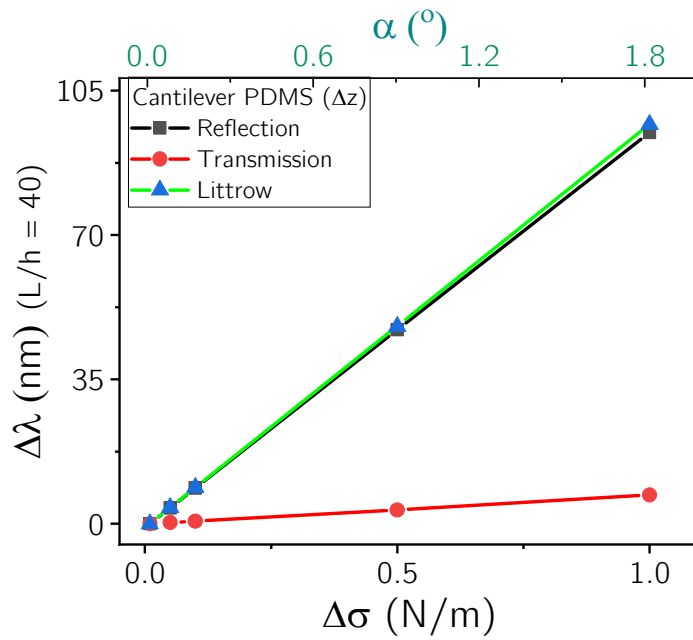
Figure 6.10 Comparison of colour change for a PDMS cantilever (L/h=40), and deflection angle associated to colour change for reflection, transmission, and Littrow configuration.

Beside the cantilever's dimensions and material, the surface stress produced by the bio-chemical reaction is as well a key parameter to increase the bending amplitude of mechanical biosensors as demonstrated in the calculation of Δz (**Figure 6.6**). Highly different values of surface stress have been reported depending on the forces playing role during the bio-chemical interaction. Chemical reactions, volume change of film polymers, self-assembled monolayers formations and large proteins interactions report surface stress values larger than $0.1\,N/m$, while the detection of small molecules such as pesticides produce values of about $8\,mN/m$ [206], [207]. Silicon or silicon nitride microcantilevers has been conventionally used for the detection of bio-recognition or conformational changes of biological molecules. Deflection in the order of $\sim 100\,nm$ have been reported, as consequence of induced surface stress changes of $0.1-0.01\,mN/m$, depending on the application/molecules. Surface stress changes as small as $0.001\,mN/m$ are expected when working with biological layers.

In other hand, from an optical point of view, the higher sensitivity of the colour response corresponds to the Littrow configuration, because of the higher

dependency on the angle change. In this way, the colour change associated to small deflections due to low surfaces stress can be read. For a colour change around $3\,nm$ produced by a surface stress of $0.1\,N/m$ a cantilever shape relation $L/h = 750$ is required for polymeric materials (polyimide). Fixing the cantilever length to $1500\mu m$, the thickness should be as thinner as $2\mu m$. For bends produced by lower surface stress as detected for biological monolayers $0.001\,mN/m$, the cantilever shape relation should be up to $L/h = 3000$, which may have some restrictions related to the fabrication technics, nanostructure height, and initial bending due to residual stress. According to this drawback, the minimum surface stress detected would be $\sigma = 0.05\,N/m$ in order to produce at least $3\,nm$ of colour change with polymeric cantilevers.

In the case of PDMS, high bends can be achieved with low surface stress changes. For the case of biological monolayers with surface stress of $0.001\,mN/m$, the cantilever shape relation should be $L/h = 231$, fixing the cantilever length to $1500\,\mu m$, the thickness should be around $6.5\,\mu m$ in order to achieve a colour change of $3\,nm$. This cantilever thickness can be easily achieved using the fabrication technics described in Chapter 3: for nanostructured PDMS-based cantilevers. The possible drawback can be the initial bending due to residual stress and difficulty to manipulate cantilevers with this thickness.

The minimum value of colour change -$3nm$- was considered in relation to the experimental signal noise ratio S/R of colour measurements made in section 5.4.4: colorimetric membrane sensitivity analysis by flow rate using UV-Visible spectrometry (Flame spectrometer from Ocean Optics).

6.4 Surface stress by molecular structure change

In this subchapter, I demonstrate the capability of polymeric mechanochromic cantilevers to quantify photo-induced molecular conformational changes through its conversion to colour changes (**Figure 6.11**) by the use of a low cost RGB camera. We study as well two different diffraction configuration schemes and their effect on the final device sensitivity.

Photo-sensitive azobenzene molecules, which present a reversible

photoisomerization from the thermally stable *trans* (E) to meta stable *cis*(Z) states, were used to demonstrate the actuation and sensing mechanism of structural conformational changes upon exposure to UV light. Azobenzene molecules and polymers has been used to induce bending of coated microcantilevers [203], and develop a large amount of photo-actuators with applications in light-driven robotics, artificial hands, sensing in biology, or even for light energy harvesting [199], [209].

Two light diffraction configurations (transmission and reflection) were studied. Higher sensitivities were achieved when using the reflection configuration according to the cantilever diffraction angle dependence.
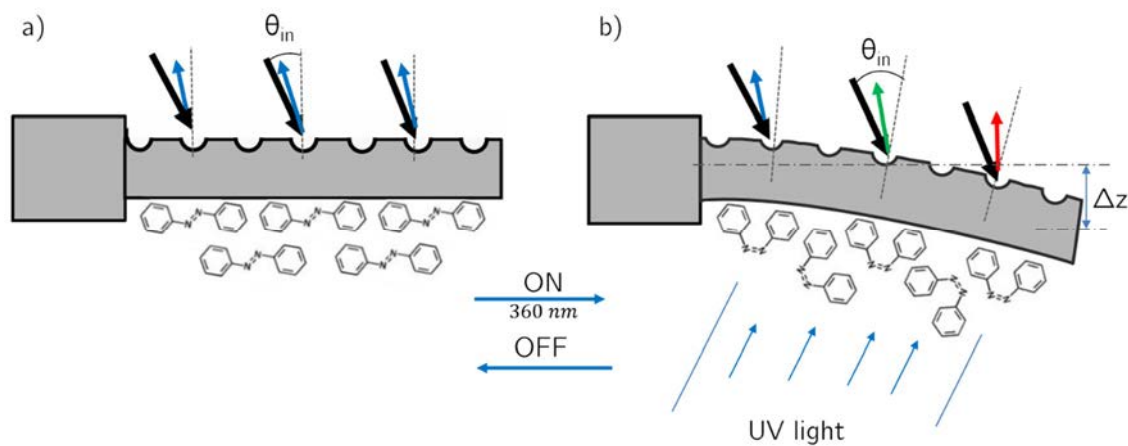
Figure 6.11 Orientative schematic for a colorimetric PDMS cantilever deflected by azobenzene conformational changes.

6.4.1 Cantilevers fabrication and integration

For cantilevers fabrication, a thin layer of PDMS was spin-coated over the 1D lineal PDMS master (see section 3.2.), achieving $50\,\mu m$ thickness layer after curing at $80\,^{o}C$ for 30 minutes in an oven. The PDMS relation was $10{:}1$. An array of cantilevers previously designed was cut by laser. The final PDMS cantilevers have one side corrugated surface by 1D linear diffraction grating with $600\,grooves/mm$ and dimensions $L = 1500\,\mu m$, $h = 50\,\mu m$, $w = 500\,\mu m$ for length, thickness and width, respectively.

Before peel-off, the cantilevers were cleaned from residues with ethanol in order to avoid optical artefacts, and covered with a layer of azobenzene molecules. Azobenzene based solution was prepared by dissolving $20\,mg$ of 4-(Dimethylamino)azobenzene-4′-sulfonyl chloride (Dabs-Cl) in $2\,ml$ of Dimethylformamide (DMF) stirring for 30 minutes at room temperature into a fume hood until achieve a uniform liquid solution.

The non-corrugated cantilevers surface was activated by oxygen plasma for 50 seconds at $40\,W$ of power, and $10\,ml/min$ of oxygen flux. $5\,\mu l$ of Dabs-Cl solution was released on the activated cantilever surface, then evaporated in oven for 10 minutes at $70\,^oC$ for helping to achieve a uniform layer. The cantilevers were peel-off from the master with help of a thin piece of COP leaving suspended the cantilevers. The COP surface was previously coated with APTES silane to be able to bond the PDMS by oxygen plasma treatment [210] . After evaporation, the cantilevers were stored in a black box in order to avoid the direct light exposure.
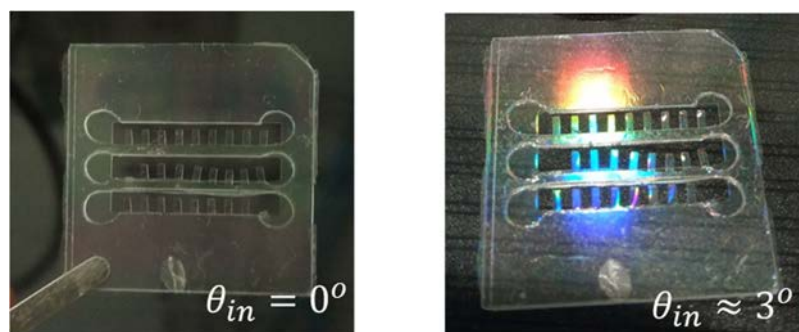
Figure 6.12 Array of cantilevers illuminated at (left) $0\,^o$, and (right) $\sim3\,^o$.

6.4.2 Characterization

The corrugated cantilever face was morphological analysed by electron microscopy to check that the grating grooves are in the direction perpendicular to the cantilever orientation (**Figure 6.13**, up). Changes in the grating direction give non-uniform cantilever coloration due to the azimuthal angle dependence. The thickness of the azobenzene layer was $3\pm0.5\,\mu m$, measured by confocal microscopy (**Figure 6.13**, down). The uniformity of the azobenzene layer can be

optimized by spin coating deposition, controlling the layer thickness by spinning rate regulation.
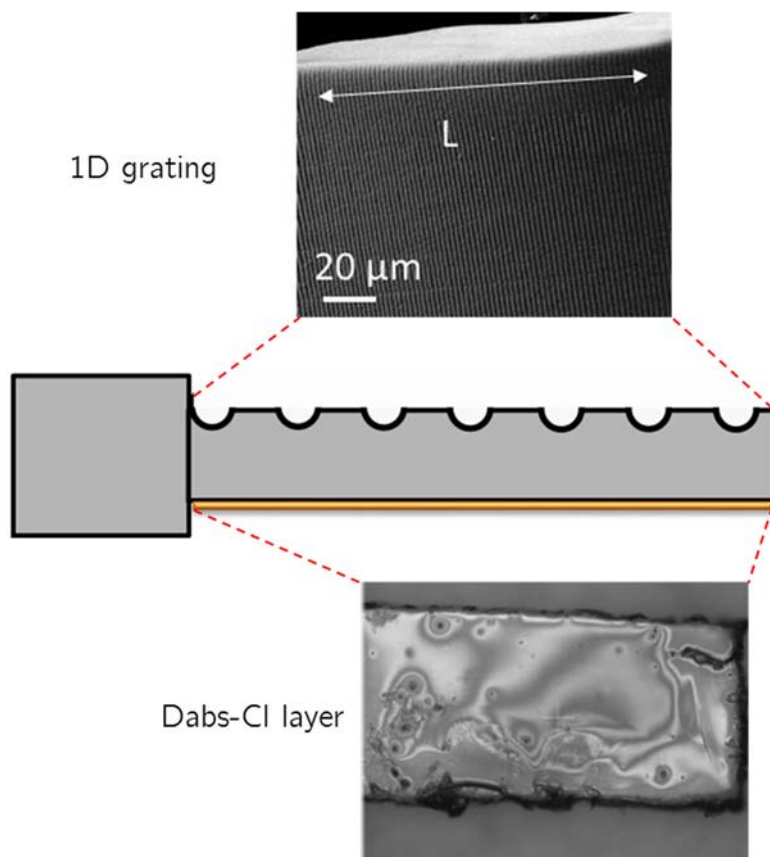
Figure 6.13 Activated PDMS cantilever: SEM image of the replicated 1D grating (up) and sensing layer of azobenzene (Dabs-Cl) of $3.5 \pm 5 \, \mu m$ thickness (down).

During the bending experiments, the cantilever profile and the cantilever free-end displacement were monitored by using an USB-microscope (Dino-Lite) situated perpendicular to the cantilever length. An image analysis software (Image J) was used to measure the free-end displacement and the angle change from the acquired images.

Simultaneously, the cantilever deflection was measured by analysing the colour diffracted by the corrugated surface in two different set-up configurations: transmission and reflection. In both cases, a collimated white light (halogen lamp Ocean Optics) and USB-microscope were used. The angles of incidence of the light and the angle of reflection and transmission were

selected in order to work in the visible range (**Figure 6.14**). For the fabricated corrugated surface with a periodicity of $\sim 1600\ nm$, angles of incidence of $\theta = 25^{o}$ and $\beta = 0^{o}$ for reflection, and $\theta = 0^{o}$ and $\beta = 25^{o}$ for transmission configuration were chosen, as shown in **Figure 6.14**.
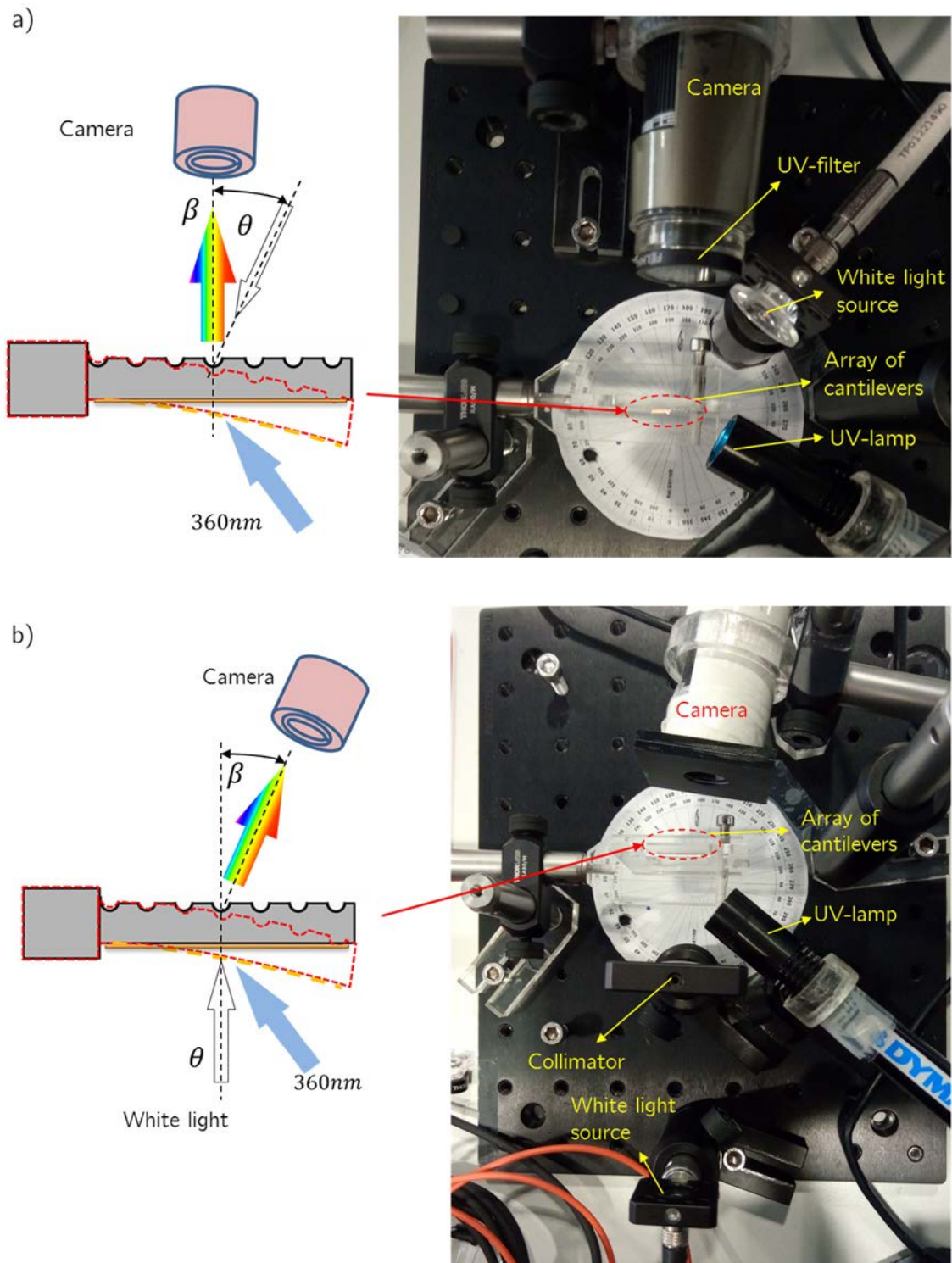
Figure 6.14 Angle configuration and set-up for a) reflection and b) transmission

Image processing was performed using free ImageJ software. For colour evaluation, a region of interest (ROI) at the cantilever free-end was marked in the resulting colour images to calculate the mean RGB values. Finally, the RGB values were converted to the HSV (Hue, saturation, value) colour space, were the H value represent the colour.

6.4.3 Results and discussion

6.4.3.1 Curvature analysis and z displacements:

The cantilever has an initial residual deflection due to the fabrication process. The measured initial cantilever displacement and deflection angle were $z_i = 138.26 \, \mu m$ and $\alpha_i = 10.48^o$ respectively.

Free bending experiments were first conducted to quantify changes in bending deformation upon irradiation to UV light of several powers. During the exposition to UV light at $360 \, nm$ to irradiate the azobenzene layer, the cantilever bent down toward the azobenzene layer side, producing a decreasing of the cantilever initial curvature. The free-end displacement Δz increases proportional as the power of the UV light increase.
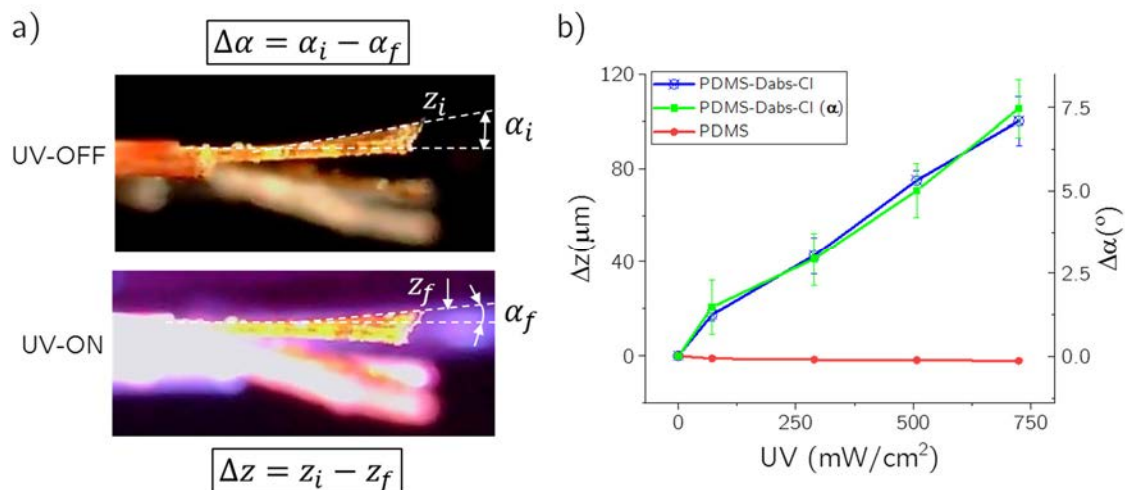
Figure 6.15 a) Cantilever curvature with initial displacement z_i at angle α_1 before UV exposure (UV-OFF), and during UV exposure (UV-ON) where the free end deflects until z_f at α_f for a power of $724 \, mW/cm^2$, b) cantilever free end displacements and

deflection angles for a reference PDMS cantilever and PDMS cantilever with azobenzene (Dabs-Cl), obtained by image analysis.

The cantilever bending toward the azobenzene layer side is due to a compression of the azobenzene layer (negative surface stress) during the isomerization process. The isomerization process involves a decrease in the distance between the two carbon atoms in position 4 of the aromatic rings of azobenzene, from 9.0 Å in the *trans* form to 5.5 Å in the *cis* form [211] leading to volume and shape changes of the azobenzene layer. An increase of the volume occupied by the cis-azobenzene induce the cantilever deformation, reducing the cantilever initial curvature (see **Figure 6.14a**). *Mirkin et al.* estimated that $cis - 1$ occupies approximately $1.5 - 2$ times the cross-sectional area occupied by $trans - 1$ [212]. For the thin layer of azobenzene deposited in the cantilever, the volume changes increase proportional to the exposure power increase. During trans-cis reaction, azobenzene does not suffer and can be isomerized on a timescale of microseconds down to sub-nanoseconds, reversibly $10^5 - 10^6$ times before fatigue [209], [211], [213].

6.4.3.2 Curvature analysis and colour change:

The PDMS cantilevers are transparent, which is ideal for working in the transmission configuration, achieving a vivid red diffracted colour when detecting the first diffracted mode (**Figure 6.16**). Due to the initial residual deflection, a gradient of colours can be observed along the cantilever, with the larger change close to the free-end. However, transmission configuration is less sensitive to small rotations of the grating respect to the normal (bending) than the reflection configuration, where for a fixed incident ray, the difference between initial and final reflection is twice the angle through which the sample has rotated. $\beta_f = 2\alpha$ (as demonstrated in section 6.3.3). This behaviour is repeated at the difference diffraction orders.

Figure 6.16 shows a sequence of cantilever images acquired at reflection and transmission configuration for several UV light power. Working in the reflection configuration is trickier, and the reflected colours are no so vivid or easy to detect due to the cantilever transparency. In both cases, due to large

initial bending, the cantilever shows a gradient of colours along its length. This behaviour is highlighted at the reflection configuration.

During the exposition to the UV light, the cantilever bent down toward azobenzene layer side, producing a reduction of the cantilever curvature and a reduction of the colour grading along the cantilever (as shown in **Figure 6.16**). Depending on the initial deformation and the power applied, the cantilever will reduce its curvature until reach a flat position, and will continue its deformation, increasing its curvature in opposite direction to the initial one and therefore increasing again the colour gradient. The cantilever show in **Figure 6.16** in transmission configuration shows exactly this behaviour. The initial colour gradient is reduced until reaching a practically flat position for $289.6 \, mW/cm^2$ power, and increases again its gradient for higher powers. Control experiments were performed with a bare PDMS reference microcantilever. No deflection of this cantilever was observed upon exposure to the $365 \, nm$ UV light (**Figure 6.15b**).
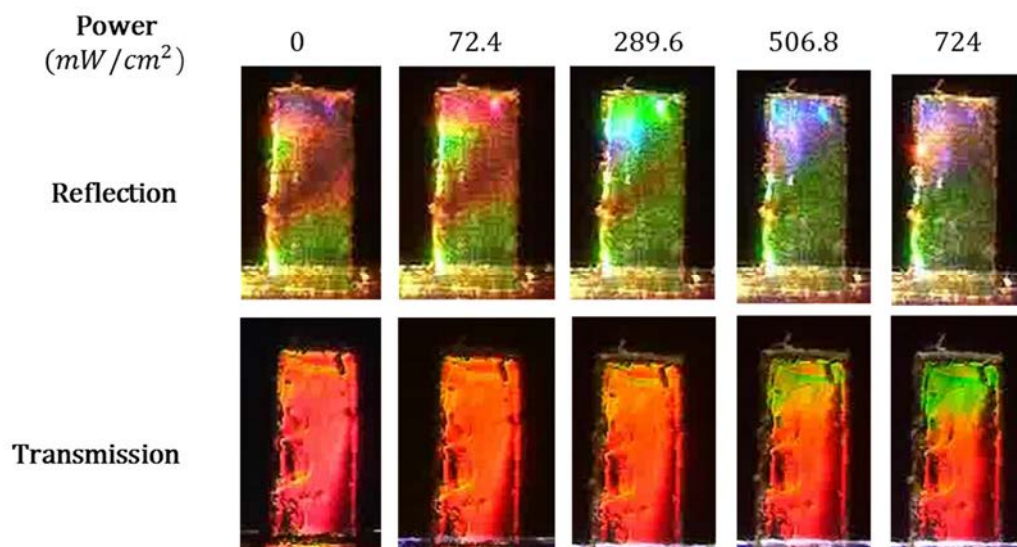
Figure 6.16 Cantilever coloration change at different UV power exposure for reflection and transmission configuration.

During the bending experiments, the maximum deflection occurs at the cantilever free-end (region of study **Figure 6.17a, (up)**), being therefore that section the one displaying the maximum colour change due to the grating angle dependence. In this case, each state of cantilever before and during the

exposure was captured at $10\,images/s$ rate, and then extracted the Δhue values of each image to be represented in function of time. **Figure 6.17bc(up)** shows the Δhue values for a periodical sequence of 3 seconds exposure at four different UV powers and 4 seconds of exposure absence.

For reflection configuration (**Figure 6.17b, (up)**), after the first power exposure ($72.4\,mW/cm^2$), the cantilevers deflection gradually returned to its original hue colour during the 4 seconds of exposure absence. For this first power was assumed that just a small percentage of azobenzene molecules reach the isomerization process giving a small colour change near $4\,^o$. For the second power exposure ($289.6\,mW/cm^2$), the cantilever achieve $109\,^o$ of Δhue, and for the third power ($506.8\,mW/cm^2$), Δhue was $233\,^o$. In both cases, the 4 seconds of exposure absence was not enough to the cantilever deflection totally returned to its original position. For the fourth power ($724\,mW/cm^2$), the 3 seconds exposure was enough to achieve $343\,^o$ of Δhue colour. In this case, around 10 seconds without exposure was needed to return the cantilever to its original position.

For transmission (**Figure 6.17c, (up)**), the 4 seconds of exposure absence seems to be enough to return the cantilever to its original position. In this case, the colour change for each power was less sensitive compared with colour change obtained in reflection configuration, being needed larger deflections to achieve higher Δhue values. According to experimental results, the detection relation was $0.47^o/mW$, and $0.095^o/mW$ for reflection and transmission respectively. Comparing this two values, the reflection configuration is more sensitive than transmission in $\sim 10{:}2$ ratio.

The theoretical sensitivity for transmission configuration was illustrated in **Figure 6.10** for PDMS cantilevers and for a surface stress range, where, the colour change was measured in wavelength. Therefore, the relation between the attribute hue and wavelength is led by the perception of the dominant wavelength and calculated performing a comparison between scales for hue and wavelength (**Figure 6.17a, (down)**)
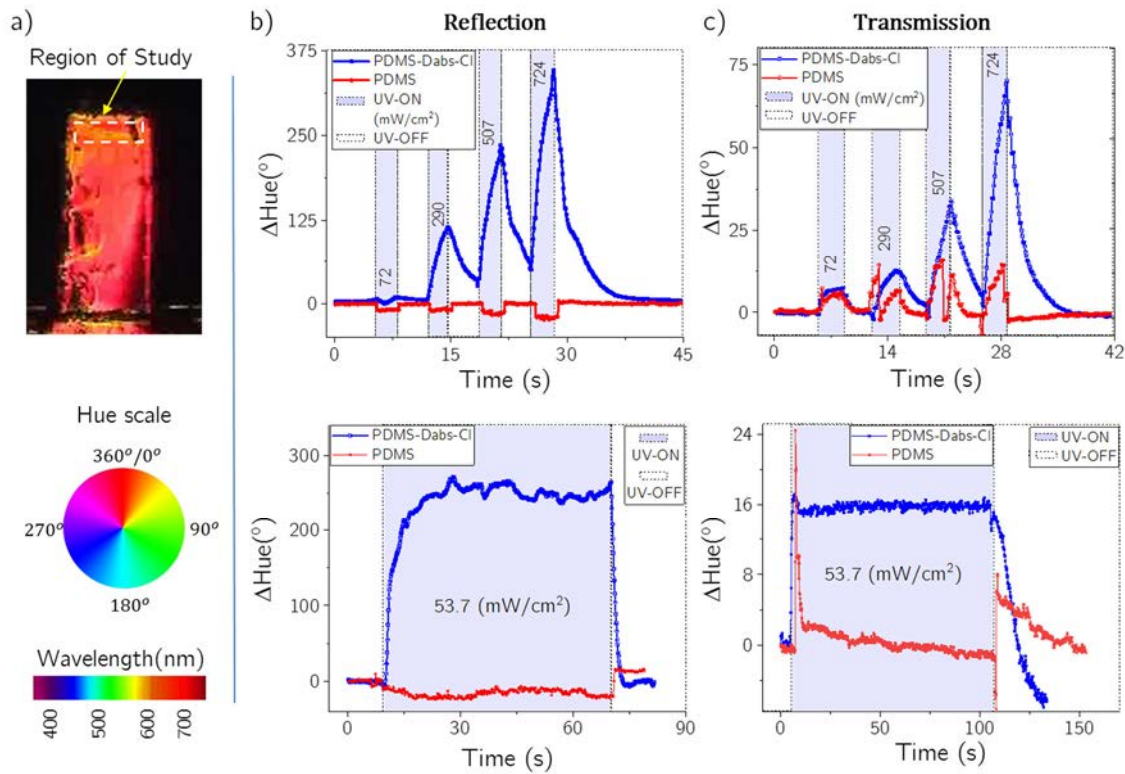
Figure 6.17 a)(up) Cantilever showing the region of interest (ROI) for image analysis, (down) visual relationship between wavelength and Hue colour scale. (b, c) Hue colour change by UV power exposure for Reflection and Transmission configuration, (up) Hue changes due to 3 seconds UV exposure at different powers, (down) Hue change due to continuous exposure at $53.7\ mW/cm^2$ UV power.

By evaluating the cantilevers under continuous UV exposure, the cantilevers reach stabilization at its maximum deflection after 10 seconds at $53.7\ mW/cm^2$ of power exposure. For reflection configuration, the corresponding Δhue value was 251° (**Figure 6.17b, (down)**). This same experiment was performed for transmission configuration; in this case, a maximum $\Delta hue = 16^o$ was achieved in the first 4 seconds of exposure. Given the high sensitivity of reflection configuration, the small perturbations detected when the cantilever was on the maximum deflection gave a colour change of ($\pm 7.5^o$). In contrast, in the transmission configuration the small perturbations gave a colour change $\sim 1^o$ (**Figure 6.17c, (down)**).

For a periodical sequence of exposure at the same UV power, $53.7\ mW/cm^2$, the cantilevers were irradiated alternating between on to off in a period of 10 seconds. The cantilever was stabilized at 10 seconds of exposure; when the

exposure was removed, the cantilever deflection gradually returned to its original position as shown in **Figure 6.18**. After the first 10 seconds pulse, the sequential maximum deflections were stabilized at $256 \pm 4\,^{o}$.
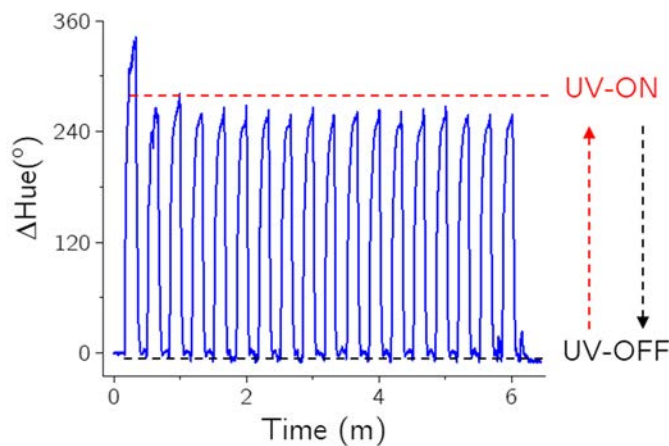
Figure 6.18 Δhue measured in reflection configuration for periodical switching on-off at $53.7\ mW/cm^2$ UV power.

The average RGB of the ROI was used for the HSV scale transformation. Therefore, the non-uniform coloration of the surface can modify the final average value to be transformed. For high colour changes, small irregularities can be not considered, but for detection of small changes, the few irregularities can modify the final colour transformation.

For these experimental results, most of colour irregularities are due to the initial bending and changes in the azimuthal angle of the cantilever. In this sense, future work would include the optimization of the detection method and the cantilever fabrication (alignment of the grating with the cantilever length). The initial bending can be reduced by changing the thin layer of azobenzene molecules by an azobenzene polymer monolayer (SAM), and the azimuthal angle dependence can be solved by using 2D nanostructures instead of linear diffraction gratings.

Chapter 7: Conclusions

The development of this thesis has led origin to a new kind of mechanical sensors based on colorimetric response for different application areas such as health, environment, optofluidics, radiation detectors, among others. These sensors change their colour intrinsically by external mechanical actions without the need of labelling, and allowing the monitoring in real time by a detection system of simple implementation. Following the trend of current advances in BIOMEMS technology, the developed sensors are based in low-cost and rapid fabrication processes, compatible with microfluidics platforms for POC applications.

For the optimum design of sensors, an analytical study about the physics of mechanical transducer (cantilevers and membranes) has been performed. In this study, the cantilever bending when it is working in static mode was analysed, including the relationship between deflection and surface stress associated. The mechanics of a membrane under load deformation was also studied taking into account the mathematical models used for thin and tick membranes according their maximum deformation. The physics involved in structural coloration, and its application to the sensors deformation, was also analysed looking to improve the performance and increase the detection sensitivity.

The fabrication and characterization of mechanochromic materials for the manufacture of mechanical sensors has been the prime objective to achieve in this thesis. Focusing on the development of low-cost devices, elastomeric materials were used for the fabrication of linear and 2D diffraction gratings, as well as 2D and 3D colloidal photonic crystals. The fabrication of colloidal mechanochromic materials with thickness lower than $50\mu m$ was the first challenge to overcome, being finally possible to fabricate materials with less than $5\mu m$ thickness maintaining the periodicity of the nanostructure. Polymeric materials show attractive optomechanical characteristics for the development of mechanochromic materials, thus, facilitating the fabrication of cantilevers. In this way, nanostructured cantilevers based in PDMS, polyimide and SU-8 were

fabricated using a 1D commercial diffraction grating with successful results, being ease to scale the method to standard microfabrication processes.

As alternative to the use of linear gratings, 2D colloidal assemblies were used as a mask for the fabrication of nanopillars and nanoholes on silicon wafers. Again polyimide (PI) and SU-8 were used for replication, facilitating the work in large surfaces and totally compatible with standard microtechnologies processes.

Two different types of photonic membranes, based on 3D and 2D photonic crystals were fabricated and compared. A deep study of the morphology of the crystals and the colour tuning of the membranes under external linear in-plane or out-of-plane mechanical stimulus was performed by SEM and UV-Visible spectrometry, respectively. In the case of 3D PhC, the change in coloration is produced in correspondence to changes in the interlayer distance, while the 2D PhC reflected colour depends on the periodicity and the angle of interaction, which results in higher sensitivities for small deformations of the membrane. Other contributors to the 2D PhC sensitivity is the lower Young's modulus compare to the 3D PhC membranes. The fabrication method used for 2D PhC membranes is ease to reproduce for material thickness up to $90 \mu m$.

A label-free and power-free array of colour tunable pressure sensors based on flexible nanostructured (inverse 2D-Phc) suspended membranes for multiplexed optofluidics applications has been demonstrated. The approach based on white light interrogation to measure the membranes bending was successfully demonstrated by using both UV-Visible spectrometry and image analysis. The fabricated optical pressure sensing platform displays a specific reflective colour for each sensor depending on the pressure-induced bending. The expected gradient of colours along the membrane was observed by image evaluation, depending on the pressure applied, and was found to agree with the wavelength dependency on the position of focus when using UV-Visible spectrometry. A simple and cost-effective method was used for the fabrication of the suspended photonic membranes. The platform shows a sensitivity of $0.17 \, kPa^{-1}$ for the detection of low pneumatic or fluid pressures (in a range between -1 and $1 \, kPa$), similar to others works with more complex fabrication

processes. In addition, a higher sensitivity could be achieved by adjusting the membrane size and the PDMS thickness.

A theoretical analysis of a surface stress colorimetric mechanical sensor based in cantilevers has been performed in the final part of this thesis. This sensor design has been a result of an effective combination of the diffraction capabilities of diffraction grating with the high performance of mechanical cantilevers. The diffraction grating on the cantilever surface produces an intrinsic coloration of the sensor, providing the capability to produce a change in coloration when the cantilever deflects. For this theoretical design, the minimum surface stress that could be detected is $\sigma = 0.05\,N/m$ in order to produce at least $3\,nm$ of colour change for PI cantilevers. For PDMS cantilevers, the minimum surface stress that could be detected is $0.001\,mN/m$, to produce the same $3\,nm$ of colour change, which means to have a cantilever with $1500\,\mu m$ length and $6.5\,\mu m$ thickness, that can be easily fabricated with certain difficulty for manipulation during the measures.

A label-free surface stress sensor based in colorimetric cantilevers has been fabricated and characterized by the use of simple camera and image processing. As proof-of-concept, colorimetric surface stress sensor has been achieved by the use of a photo-sensible material (azobenzene) disposed in the cantilever flat surface. The changes in surface stress were evaluated by irradiating the cantilevers at different powers and measuring the cantilever colour change by a transformation of RGB images to HSV scale. The method based in the hue analysis (HSV) allows the detection of 1° of colour change that is approximately 0.75 nm for the visible band in wavelengths ($400nm$ to $650nm$).

Future prospective

The development of mechanochromic sensors allowed achieving high sensitive and high throughput sensor platform facilitating the multidetection by the intrinsically colour change of the sensor and a simple detection system. In

this sense, possible improvements have been detected that would be developed in the future.

In the development of mechanochromic materials, colloidal assembly was used as a 2D grating mask for the fabrication of nanopillars and nanoholes on silicon wafers. However, small errors in the packaging reduce the final colour resolution, affecting the detection of small colour changes of the transducers. In this sense, the optimization of the colloidal assembly in large areas would be done preferably by using spin coating techniques, to achieve an error free 2D grating mask, with total compatibility with standard microtechnologies processes.

The theoretical design of mechanochromic sensors based in cantilevers indicates that by modifying the cantilever size and the nanostructured parameters, the cantilevers would be able to detect small surface stress around $0.001 \, mN/m$. However, the experimental demonstration to detect such small surface stress values has not been done in this Thesis. In this way, optimization of the sensor design and experimental essays producing such a small surface stress changes, such as self-assembly monolayer (SAM) formation or antigen-antibody interactions will be done in the near future.

The detection method based in a camera and image post-processing allowed the efficient acquisition and measurement of the transducers colour change, as demonstrated in this Thesis. However, the development of software for real time monitoring of the sensors colour, without a post-processing, is very convenient. Some work has been initiated in this direction, and future work would include the evaluation of the sensors and the continue monitoring in real time.

Given the portability and compatibility of the mechanochromic sensors developed in this Thesis, future work would include the integration of the sensor and the detection system into POC devises for the detection of cytokines at the medical consultancy, and their integration into other microtechnologies platforms, such as organ-on-a-chip (OOC), for the sensing and real time monitoring of different analytes and factors.

Appendices

Appendix A: Publications related with the Thesis

Articles

1. P. Escudero, J. Yeste, R. Villa, M. Alvarez, *"Low cost nanomechanical surfaces stress based sensors fabricated by hybrid materials"*. Proceedings SPIE Microtechnologies, June 2, 2017.

2. P. Escudero, J. Yeste, C. Pascual-Izarra, R. Villa, and M. Alvarez, *"Color tunable pressure sensors based on polymer nanostructured membranes for optofluidic applications", Scientific Reports, 9(1):3259, 2019.*

3. P. Escudero, C. Pascual-Izarra, R. Villa, and M. Alvarez, *"Surface stress-based mechanochromic sensors", In preparation*.

4. P. Escudero, C. Pascual-Izarra, R. Villa, and M. Alvarez, "*Sensitivity analysis of structural coloration for mechanical sensing*". *In preparation* (Sensors)

5. P. Güell-Grau, P. Escudero, R. Villa, B. Sepúlveda, M. Álvarez, "*Plasmonic nanomechanical infrared sensor with colorimetric readout, In preparation*.

Participation in Congress

1. P. Escudero, R. Villa, M. Alvarez, **"***Colorimetric surface stress sensors based on smart polymers***"**, 2nd Scientific Meeting of BNC-b Students, June 29, 2016. Poster Presentation.

2. P. Escudero, J. Yeste, R. Villa, M. Alvarez, "*Nanomechanical surfaces stress sensors fabricated by smart hybrid materials*", 5th International Conference on Multifunctional, Hybrid and Nanomaterials, March 9, 2017. Oral Presentation.

3. P. Escudero, R. Villa, M. Alvarez, "*Nanomechanical sensing based on 2D colloidal diffraction gratings*", 3rd Scientific Meeting of BNC-b Students, November 7-8, 2017. Oral Presentation.

4. P. Escudero, R. Villa, M. Alvarez, "*Nanomechanical Sensing with 2D colloidal Diffraction Gratings*". NanoBio&Med2017, November 22-24, 2017. Poster Presentation.

5. P. Escudero, R. Villa, M. Alvarez, "*Nanomechanical sensing based on 2D colloidal diffraction gratings*", 2nd International Congress on Physics, December 6-8, 2017. Oral Presentation.

6. P. Escudero, R. Villa, and M. Alvarez, "*Nanomechanical sensing based on colorimetric response*", Ibersensors-2018, September 17-20, 2018. Oral Presentation.

7. P. Escudero, J. Yeste, C. Pascual-Izarra, R. Villa, M. Alvarez, "*Polymeric opto-mechanical systems for sensing applications*", MNE2018, September 24-27, 2018. Oral Presentation.

8. P. Güell-Grau, P. Escudero, R. Villa, B. Sepúlveda, M. Álvarez, "*Plasmonic nanomechanical infrared sensor with colorimetric readout*", MNE2018, September 24-27, 2018. Poster Presentation.

9. P. Güell-Grau, P. Escudero, R. Villa, B. Sepúlveda, M. Álvarez, "*Wavelength-tunable near-infrared sensor with colorimetric readout*", MicroTAS2018, November 11-15, 2018. Poster Presentation.

10. P. Escudero, J. Yeste, C. Pascual-Izarra, R. Villa, M. Alvarez, "*Label-free colorimetric detection of nanomechanical bending for high-throughput sensing*", MicroTAS2018, November 11-15, 2018. Poster Presentation.

Appendix B: Thesis Framework

The development of this Thesis was supported by:

Acronyms and abbreviations

1D
One Dimensional, xvi, 36, 38, 39, 42, 47, 81, 96, 97, 101, 102, 112, 113, 114

2D
Two Dimensional, xvi, xvii, 37, 38, 39, 42, 47, 48, 50, 53, 54, 55, 57, 64, 67, 70, 75, 80, 81, 83, 84, 96, 97, 101, 121, 123, 125, 127

3D
Three Dimensional, xvi

APTES
3-Aminopropyl)triethoxysilane, 113

BIOMEMS
Biomedical Microelectromechanical Systems, 1

CCD
Charge-Coupled Device, xiv, 14

ccp
Cubic Close-Packed, 38, 39

COP
Cyclic Olefin Copolymer, 84, 113

CPhC
Colloidal Photonic Crystals, 83

Dabs-Cl
4-(Dimethylamino)azobenzene-4'-sulfonyl chloride, 113, 114, 117

DMF
Dimethylformamide, 113

DNA
Deoxyribonucleic acid, 5, 98

DRIE
Deep Reactive-Ion Etching, 64

FFT
Fast Fourier Transform, 53, 54

FSR
Free Spectral Range, 34, 36

HCMs
High-contrast meta-structures, 13, 14

HSV
Hue, Saturation, Value, 116, 121

INV-2D
Inverse of two dimensional photonic crystal, 52, 54, 77, 84, 123

IoT
Internet of Things, 2

LED
Light Emitting Diode, 14, 93

LOC
Laboratory-on-a-chip, 2, 3

MC
Mechanochromic Cantilever, 96

MEMS
Microelectromechanical Systems, 1, 2, ii, xiii, xiv, xvi, 1

MOSFET
Metal-oxide semiconductor field-effect transistors, 10

PDMS
Polydimethylsiloxane, xvii, 42, 43, 44, 45, 47, 48, 49, 50, 52, 53, 55, 56, 59, 60, 61, 63, 65, 66, 67, 68, 69, 74, 80, 81, 82, 83, 84, 85, 86, 89, 92, 98, 103, 104, 105, 106, 107, 108, 109, 110, 111, 112, 113, 114, 117, 118, 119, 124

PEEK
Polyether ether ketone, 98

Bibliography

[1]   R. and M. ltd, "Point Of Care/POC/Rapid Diagnostic Market By Test, Platform, Mode, End User – Global Forecast To 2024." [Online]. Available: https://www.researchandmarkets.com/reports/4746072/point-of-carepocrapid-diagnostic-market-by. [Accessed: 25-Mar-2019].

[2]   "Biomedical Diagnostics at Point-of-Care 2019-2029: Technologies, Applications, Forecasts," *IDTechEx*, 14-Aug-2018. [Online]. Available: https://www.idtechex.com/research/reports/biomedical-diagnostics-at-point-of-care-2019-2029-technologies-applications-forecasts-000622.asp. [Accessed: 25-Mar-2019].

[3]   P. Wang and L. J. Kricka, "Current and Emerging Trends in Point-of-Care Technology and Strategies for Clinical Validation and Implementation," *Clinical Chemistry*, vol. 64, no. 10, pp. 1439–1452, Oct. 2018.

[4]   J. L. V. Shaw, "Practical challenges related to point of care testing," *Practical Laboratory Medicine*, vol. 4, pp. 22–29, Apr. 2016.

[5]   H. Kim, D.-R. Chung, and M. Kang, "A new point-of-care test for the diagnosis of infectious diseases based on multiplex lateral flow immunoassays," *Analyst*, vol. 144, no. 8, pp. 2460–2466, Apr. 2019.

[6]   K. Khunti, "Near-patient testing in primary care," *Br J Gen Pract*, vol. 60, no. 572, pp. 157–158, Mar. 2010.

[7]   I. Hernández-Neuta *et al.*, "Smartphone-based clinical diagnostics: towards democratization of evidence-based health care," *Journal of Internal Medicine*, vol. 285, no. 1, pp. 19–39, 2019.

[8]   A. C. Sun and D. A. Hall, "Point-of-Care Smartphone-based Electrochemical Biosensing," *Electroanalysis*, vol. 31, no. 1, pp. 2–16, 2019.

[9]   D. Xu, X. Huang, J. Guo, and X. Ma, "Automatic smartphone-based microfluidic biosensor system at the point of care," *Biosensors and Bioelectronics*, vol. 110, pp. 78–88, Jul. 2018.

[10]   T. Kaya *et al.*, "Wearable Sweat Sensors: Background and Current Trends," *Electroanalysis*, vol. 31, no. 3, pp. 411–421, 2019.

[11]   M. Cuartero, M. Parrilla, and G. A. Crespo, "Wearable Potentiometric Sensors for Medical Applications," *Sensors*, vol. 19, no. 2, p. 363, Jan. 2019.

[12]   E. Ghafar-Zadeh, "Wireless Integrated Biosensors for Point-of-Care Diagnostic Applications," *Sensors*, vol. 15, no. 2, pp. 3236–3261, Feb. 2015.

[13]   G. Aroganam, N. Manivannan, and D. Harrison, "Review on Wearable Technology Sensors Used in Consumer Sport Applications," *Sensors*, vol. 19, no. 9, p. 1983, Jan. 2019.

[14]   Y. Liu *et al.*, "Epidermal mechano-acoustic sensing electronics for cardiovascular diagnostics and human-machine interfaces," *Science Advances*, vol. 2, no. 11, p. e1601185, Nov. 2016.

[15]   B. Ibarlucea, X. Munoz-Berbel, P. Ortiz, S. Büttgenbach, C. Fernández-Sánchez, and A. Llobera, "Self-validating lab-on-a-chip for monitoring enzyme-catalyzed biological reactions," *Sensors and Actuators B: Chemical*, vol. 237, pp. 16–23, Dec. 2016.

[16]   Y. Xu, Y. Liu, Y. Wu, X. Xia, Y. Liao, and Q. Li, "Fluorescent Probe-Based Lateral Flow Assay for Multiplex Nucleic Acid Detection," *Anal. Chem.*, vol. 86, no. 12, pp. 5611–5614, Jun. 2014.

[17]   J. Wei, Z. Zeng, and Y. Lin, "Localized Surface Plasmon Resonance (LSPR)-Coupled Fiber-Optic Nanoprobe for the Detection of Protein Biomarkers," in *Biosensors and Biodetection: Methods and Protocols Volume 1: Optical-Based Detectors*, A. Rasooly and B. Prickril, Eds. New York, NY: Springer New York, 2017, pp. 1–14.

[18]   "Biosensors Market Research Report: Market size, Industry outlook, Market Forecast, Demand Analysis,Market Share, Market Report 2018-2023." [Online]. Available: https://www.industryarc.com/Report/15704/biosensors-market.html?gclid=CjwKCAjw9dboBRBUEiwA7VrrzYhpKT_g5H8x8INNEvKZc XeQYv8VDYk0WeK9AmlY8xhMV3HT5nAJGxoCurIQAvD_BwE. [Accessed: 28-Jun-2019].

[19]   D. Dey and T. Goswami, "Optical Biosensors: A Revolution Towards Quantum Nanoscale Electronics Device Fabrication," *J Biomed Biotechnol*, vol. 2011, pp. 1–7, 2011.

[20]   S. M. Russell, A. Alba-Patiño, M. Borges, and R. de la Rica, "A Robust and User-Friendly Alternative to Densitometry Using Origami Biosensors and Digital Logic," *ACS Sens.*, vol. 3, no. 9, pp. 1712–1718, Sep. 2018.

[21]   L. Reverté, B. Prieto-Simón, and M. Campàs, "New advances in electrochemical biosensors for the detection of toxins: Nanomaterials, magnetic beads and microfluidics systems. A review," *Analytica Chimica Acta*, vol. 908, pp. 8–21, Feb. 2016.

[22]   D. Grieshaber, R. MacKenzie, J. Vörös, and E. Reimhult, "Electrochemical Biosensors - Sensor Principles and Architectures," *Sensors (Basel)*, vol. 8, no. 3, pp. 1400–1458, Mar. 2008.

[23]   Z. Qie *et al.*, "Fast detection of atrazine in corn using thermometric biosensors," *Analyst*, vol. 138, no. 17, pp. 5151–5156, Jul. 2013.

[24]   M. Pohanka, "Overview of Piezoelectric Biosensors, Immunosensors and DNA Sensors and Their Applications," *Materials (Basel)*, vol. 11, no. 3, Mar. 2018.

[25]   M. M. Álvarez Sánchez, "Desarrollo de un sensor nanomecánico para estudios de adsorción de moléculas biológicas y reconocimiento molecular," Universidad Autónoma de Madrid, Madrid, 2005.

[26]   R. Pechmann, J. M. Köhler, W. Fritzsche, A. Schaper, and T. M. Jovin, "The Novolever: A new cantilever for scanning force microscopy microfabricated from polymeric materials," *Review of Scientific Instruments*, vol. 65, no. 12, pp. 3702–3706, Dec. 1994.

[27]   G. Genolet *et al.*, "Soft, entirely photoplastic probes for scanning force microscopy," *Review of Scientific Instruments*, vol. 70, no. 5, pp. 2398–2401, May 1999.

[28]   J. Zou, X. Wang, D. Bullen, K. Ryu, C. Liu, and C. A. Mirkin, "A mould-and-transfer technology for fabricating scanning probe microscopy probes," *J. Micromech. Microeng.*, vol. 14, no. 2, pp. 204–211, Oct. 2003.

[29]   M. Alvarez and L. M. Lechuga, "Microcantilever-based platforms as biosensing tools," *Analyst*, vol. 135, no. 5, pp. 827–836, 2010.

[30]   A. S. Fiorillo, C. D. Critello, and S. A. Pullano, "Theory, technology and applications of piezoresistive sensors: A review," *Sensors and Actuators A: Physical*, vol. 281, pp. 156–175, Oct. 2018.

[31]   A. K. Basu, A. Basu, and S. Bhattacharya, "Study of pH induced conformational change of papain using polymeric nano-cantilever," *AIP Conference Proceedings*, vol. 2083, no. 1, p. 030001, Mar. 2019.

[32]   H.-F. Ji, Y. Feng, X. Xu, V. Purushotham, T. Thundat, and G. M. Brown, "Photon-driven nanomechanical cyclic motion," *Chem. Commun. (Camb.)*, no. 22, pp. 2532–2533, Nov. 2004.

[33]   M. Salve, M. Dhone, P. Rewatkar, S. Balpande, and J. Kalambe, "Design and Sensitivity Analysis of Micro-Cantilever Based Biosensor for Tumor Detection," *Sensor Letters*, vol. 17, pp. 64–68, Jan. 2019.

[34] C. Li, M. Zhang, Z. Zhang, J. Tang, and B. Zhang, "Microcantilever aptasensor for detecting epithelial tumor marker Mucin 1 and diagnosing human breast carcinoma MCF-7 cells," *Sensors and Actuators B: Chemical*, vol. 297, p. 126759, Oct. 2019.

[35] D. K. Agarwal *et al.*, "Detection of heart-type fatty acid-binding protein (h-FABP) using piezoresistive polymer microcantilevers functionalized by a dry method," *Appl Nanosci*, vol. 8, no. 5, pp. 1031–1042, Jun. 2018.

[36] G. Zhang, C. Li, S. Wu, and Q. Zhang, "Label-free aptamer-based detection of microcystin-LR using a microcantilever array biosensor," *Sensors and Actuators B: Chemical*, vol. 260, pp. 42–47, May 2018.

[37] A. K. Basu, A. N. Sah, A. Pradhan, and S. Bhattacharya, "Poly-L-Lysine functionalised MWCNT-rGO nanosheets based 3-d hybrid structure for femtomolar level cholesterol detection using cantilever based sensing platform," *Scientific Reports*, vol. 9, no. 1, p. 3686, Mar. 2019.

[38] S. B. Patil *et al.*, "Modified cantilever arrays improve sensitivity and reproducibility of nanomechanical sensing in living cells," *Communications Biology*, vol. 1, no. 1, p. 175, Oct. 2018.

[39] K.-W. Li and Y.-K. Yen, "Gentamicin drug monitoring for peritonitis patients by using a CMOS-BioMEMS-based microcantilever sensor," *Biosensors and Bioelectronics*, vol. 130, pp. 420–426, Apr. 2019.

[40] W. Song and D. Psaltis, "Optofluidic membrane interferometer: An imaging method for measuring microfluidic pressure and flow rate simultaneously on a chip.," *Biomicrofluidics 5*, vol. 11, no. 2011 SRC-BaiduScholar, pp. 044110–044110.

[41] C. Tsai and M. Kaneko, "On-chip pressure sensor using single-layer concentric chambers.," *Biomicrofluidics*, vol. 10 SRC-BaiduScholar, 2016.

[42] S. T. Choi, B. S. Son, G. W. Seo, S.-Y. Park, and K.-S. Lee, "Opto-mechanical analysis of nonlinear elastomer membrane deformation under hydraulic pressure for variable-focus liquid-filled microlenses," *Opt. Express, OE*, vol. 22, no. 5, pp. 6133–6146, Mar. 2014.

[43] V. Tsouti *et al.*, "Detection of DNA mutations using a capacitive micro-membrane array," *Biosensors and Bioelectronics*, vol. 26, no. 4, pp. 1588–1592, Dec. 2010.

[44] S. Satyanarayana, D. T. McCormick, and A. Majumdar, "Parylene micro membrane capacitive sensor array for chemical and biological sensing," *Sensors and Actuators B: Chemical*, vol. 115, no. 1, pp. 494–502, May 2006.

[45]   G. Yoshikawa *et al.*, "Two Dimensional Array of Piezoresistive Nanomechanical Membrane-Type Surface Stress Sensor (MSS) with Improved Sensitivity," *Sensors*, vol. 12, no. 11, pp. 15873–15887, Nov. 2012.

[46]   X. Lu, Q. Guo, Z. Xu, W. Ren, and Z.-Y. Cheng, "Biosensor platform based on stress-improved piezoelectric membrane," *Sensors and Actuators A: Physical*, vol. 179, pp. 32–38, Jun. 2012.

[47]   S. Sang, Y. Zhao, W. Zhang, P. Li, J. Hu, and G. Li, "Surface stress-based biosensors," *Biosensors and Bioelectronics*, vol. 51, pp. 124–135, Jan. 2014.

[48]   M. Chatzipetrou, G. Tsekenis, V. Tsouti, S. Chatzandroulis, and I. Zergioti, "Biosensors by means of the laser induced forward transfer technique," *Applied Surface Science*, vol. 278, pp. 250–254, Aug. 2013.

[49]   G. Yoshikawa, T. Akiyama, S. Gautsch, P. Vettiger, and H. Rohrer, "Nanomechanical Membrane-type Surface Stress Sensor," *Nano Lett.*, vol. 11, no. 3, pp. 1044–1048, Mar. 2011.

[50]   V. Tsouti *et al.*, "Detection of the biotin–streptavidin interaction by exploiting surface stress changes on ultrathin Si membranes," *Microelectronic Engineering*, vol. 86, no. 4, pp. 1495–1498, Apr. 2009.

[51]   W. Zhang *et al.*, "Structural optimization of the micro-membrane for a novel surface stress-based capacitive biosensor," *Microelectronic Engineering*, vol. 106, pp. 9–12, Jun. 2013.

[52]   M. Cha *et al.*, "Biomolecular detection with a thin membrane transducer," *Lab Chip*, vol. 8, no. 6, pp. 932–937, May 2008.

[53]   S. Sang and H. Witte, "A novel PDMS micro membrane biosensor based on the analysis of surface stress," *Biosensors and Bioelectronics*, vol. 25, no. 11, pp. 2420–2424, Jul. 2010.

[54]   V. Tsouti and S. Chatzandroulis, "Sensitivity study of surface stress biosensors based on ultrathin Si membranes," *Microelectronic Engineering*, vol. 90, pp. 29–32, Feb. 2012.

[55]   A. Jian *et al.*, "A PDMS surface stress biosensor with optimized micro-membrane: Fabrication and application," *Sensors and Actuators B: Chemical*, vol. 242, pp. 969–976, Apr. 2017.

[56]   J. Fritz, "Cantilever biosensors," *Analyst*, vol. 133, no. 7, pp. 855–863, Jun. 2008.

[57]   H. C. Pedersen, M. L. Jakobsen, S. G. Hanson, C. Dam-Hansen, T. Olesen, and P. Hansen, "Cantilever biosensor reader using a common-path, holographic

optical interferometer," *Appl. Phys. Lett.*, vol. 97, no. 22, p. 221110, Nov. 2010.

[58]   G. G. Yaralioglu, A. Atalar, S. R. Manalis, and C. F. Quate, "Analysis and design of an interdigital cantilever as a displacement sensor," *Journal of Applied Physics*, vol. 83, no. 12, pp. 7405–7415, May 1998.

[59]   F. L. Degertekin, A. G. Onaran, M. Balantekin, W. Lee, N. A. Hall, and C. F. Quate, "Sensor for direct measurement of interaction forces in probe microscopy," *Appl. Phys. Lett.*, vol. 87, no. 21, p. 213109, Nov. 2005.

[60]   R. I. Hermans, B. Dueck, J. W. Ndieyira, R. A. McKendry, and G. Aeppli, "Optical diffraction for measurements of nano-mechanical bending," *Scientific Reports*, vol. 6, p. 26690, Jun. 2016.

[61]   A. F. S. L. Chris Rowe Taitt, *Optical Biosensors, 2nd edition: Today and Tomorrow*, 2nd ed. Elsevier Science, 2008.

[62]   N. V. Lavrik, M. J. Sepaniak, and P. G. Datskos, "Cantilever transducers as a platform for chemical and biological sensors," *Review of Scientific Instruments*, vol. 75, no. 7, pp. 2229–2253, Jun. 2004.

[63]   A. Alodhayb, S. M. S. Rahman, S. Rahman, P. E. Georghiou, and L. Y. Beaulieu, "A 16-microcantilever array sensing system for the rapid and simultaneous detection of analyte," *Sensors and Actuators B: Chemical*, vol. 237, pp. 459–469, Dec. 2016.

[64]   N. Maloney *et al.*, "Fibre Optic Readout of Microcantilever Arrays for Fast Microorganism Growth Detection," *Journal of Sensors*, 2012.

[65]   M. Alvarez, J. Tamayo, and B. Actuators, "Optical sequential readout of microcantilever arrays for biological detection," vol. 106, no. 2 SRC-BaiduScholar, pp. 687–690, 2005.

[66]   C. L. Britton *et al.*, "Multiple-input microcantilever sensors," *Ultramicroscopy*, vol. 82, no. 1, pp. 17–21, Feb. 2000.

[67]   J. Fu *et al.*, "Fabrication of capacitive pressure sensor using single crystal diamond cantilever beam," *Scientific Reports*, vol. 9, no. 1, p. 4699, Mar. 2019.

[68]   M. A. Saeed, S. M. Khan, N. Ahmed, M. U. Khan, and A. Rehman, "Design and analysis of capacitance based Bio-MEMS cantilever sensor for tuberculosis detection," in *2016 International Conference on Intelligent Systems Engineering (ICISE)*, 2016, pp. 175–180.

[69]   Y. Wei, R. Torah, K. Yang, S. Beeby, and J. Tudor, "Screen printing of a capacitive cantilever-based motion sensor on fabric using a novel sacrificial layer

process for smart fabric applications," *Meas. Sci. Technol.*, vol. 24, no. 7, p. 075104, Jun. 2013.

[70] J. H. HE and Y. F. LI, "High sensitivity piezoresistive cantilever sensor for biomolecular detection," *J. Phys.: Conf. Ser.*, vol. 34, pp. 429–435, Apr. 2006.

[71] A. Setiono *et al.*, "Real-Time Frequency Tracking of an Electro-Thermal Piezoresistive Cantilever Resonator with ZnO Nanorods for Chemical Sensing," *Chemosensors*, vol. 7, no. 1, p. 2, Mar. 2019.

[72] A. Setiono *et al.*, "Phase optimization of thermally actuated piezoresistive resonant MEMS cantilever sensors," *Journal of Sensors and Sensor Systems*, vol. 8, no. 1, pp. 37–48, Jan. 2019.

[73] A. Vyas *et al.*, "A Micromachined Coupled-Cantilever for Piezoelectric Energy Harvesters," *Micromachines*, vol. 9, no. 5, p. 252, May 2018.

[74] Q. Zhao, Y. Liu, L. Wang, H. Yang, and D. Cao, "Design method for piezoelectric cantilever beam structure under low frequency condition," *International Journal of Pavement Research and Technology*, vol. 11, no. 2, pp. 153–159, Mar. 2018.

[75] J. H. Lee, K. S. Hwang, J. Park, K. H. Yoon, D. S. Yoon, and T. S. Kim, "Immunoassay of prostate-specific antigen (PSA) using resonant frequency shift of piezoelectric nanomechanical microcantilever," *Biosensors and Bioelectronics*, vol. 20, no. 10, pp. 2157–2162, Apr. 2005.

[76] G. Shekhawat, S.-H. Tark, and V. P. Dravid, "MOSFET-Embedded Microcantilevers for Measuring Deflection in Biomolecular Sensors," *Science*, vol. 311, no. 5767, pp. 1592–1595, Mar. 2006.

[77] B. S. Panwar, "MOS Integrated MEMS Structure for Bio-sensing," *Materials Today: Proceedings*, vol. 5, no. 7, Part 2, pp. 15335–15341, Jan. 2018.

[78] R. Takei *et al.*, "High-efficiency MOSFET bridge rectifier for AlN MEMS cantilever vibration energy harvester," *Jpn. J. Appl. Phys.*, vol. 56, no. 4S, p. 04CC03, Mar. 2017.

[79] T. Y. Kwon, K. Eom, J. H. Park, D. S. Yoon, T. S. Kim, and H. L. Lee, "In situ real-time monitoring of biomolecular interactions based on resonating microcantilevers immersed in a viscous fluid," *Appl. Phys. Lett.*, vol. 90, no. 22, p. 223903, May 2007.

[80] S. Mostafa *et al.*, "Integrated MOSFET-Embedded-Cantilever-Based Biosensor Characteristic for Detection of Anthrax Simulant," *IEEE Electron Device Letters*, vol. 32, no. 3, pp. 408–410, Mar. 2011.

[81]   A. Orth, E. Schonbrun, and K. Crozier, "Multiplexed pressure sensing with elastomer membranes.," *Lab Chip*, vol. 11 SRC-BaiduScholar, pp. 3810–3815, 2011.

[82]   B. Wunderlich and A. Bausch, "Diffusive spreading of time-dependent pressures in elastic microfluidic devices.," *Lab Chip*, vol. 10 SRC-BaiduScholar, pp. 1025–1029, 2010.

[83]   K. Takahashi *et al.*, "Elastomer-based MEMS optical interferometric transducers for highly sensitive surface stress sensing for biomolecular detection," *MRS Communications*, vol. 9, no. 1, pp. 381–389, Mar. 2019.

[84]   T. Takahashi, T. Hizawa, N. Misawa, M. Taki, K. Sawada, and K. Takahashi, "Surface stress sensor based on MEMS Fabry–Perot interferometer with high wavelength selectivity for label-free biosensing," *J. Micromech. Microeng.*, vol. 28, no. 5, p. 054002, Feb. 2018.

[85]   V. Jović *et al.*, "Characterization of PDMS membranes fabricated by bulkmicromachining on silicon wafers," *6th International Scientific Conference on Defensive Technologies, OTEH 2014, Belgrade, 09-10 October 2014: Proceedings*, pp. 674–679, 2014.

[86]   B. Grzybowski, D. Qin, R. Haag, and G. Whitesides, "Elastomeric optical elements with deformable surface topographies: applications to force measurements, tunable light transmission and light focusing.," *Sens Actuators Phys*, vol. 86 SRC-BaiduScholar, pp. 81–85, 2000.

[87]   Y. Tung and K. Kurabayashi, "Nanoimprinted strain-controlled elastomeric gratings for optical wavelength tuning.," *Appl Phys Lett 86*, vol. 161113, no. 2005 SRC-BaiduScholar.

[88]   C. Pada and R. Guerrero, "Fluid-enhanced tunable diffraction with an elastomeric grating.," *Opt Eng 56*, vol. 054101, no. 2017 SRC-BaiduScholar.

[89]   K. Hosokawa, K. Hanada, and R. Maeda, "A polydimethylsiloxane (PDMS) deformable diffraction grating for monitoring of local pressure in microfluidic devices.," *J Micromechanics Microengineering 12*, vol. 1, no. 2002 SRC-BaiduScholar.

[90]   X. Lu, Z. Xu, X. Yan, S. Li, W. Ren, and Z. Cheng, "Piezoelectric biosensor platform based on ZnO micro membrane," *Current Applied Physics*, vol. 11, no. 3, Supplement, pp. S285–S287, May 2011.

[91]   M. Qin, M. Sun, M. Hua, and X. He, "Bioinspired structural color sensors based on responsive soft materials," *Current Opinion in Solid State and Materials Science*, vol. 23, no. 1, pp. 13–27, Feb. 2019.

[92]   A. Piriya V.S, P. Joseph, K. Daniel S.C.G., S. Lakshmanan, T. Kinoshita, and S. Muthusamy, "Colorimetric sensors for rapid detection of various analytes," *Materials Science and Engineering: C*, vol. 78, pp. 1231–1245, Sep. 2017.

[93]   L. Shang, W. Zhang, K. Xu, and Y. Zhao, "Bio-inspired intelligent structural color materials," *Mater. Horiz.*, vol. 6, no. 5, pp. 945–958, Jun. 2019.

[94]   Yoshioka S., Matsuhana B., Tanaka S., Inouye Y., Oshima N., and Kinoshita S., "Mechanism of variable structural colour in the neon tetra: quantitative evaluation of the Venetian blind model," *Journal of The Royal Society Interface*, vol. 8, no. 54, pp. 56–66, Jan. 2011.

[95]   S. Kinoshita, S. Yoshioka, and J. Miyazaki, "Physics of structural colors," *Rep. Prog. Phys.*, vol. 71, no. 7, p. 076401, Jun. 2008.

[96]   L. P. Biró and J. P. Vigneron, "Photonic nanoarchitectures in butterflies and beetles: valuable sources for bioinspiration," *Laser & Photonics Reviews*, vol. 5, no. 1, pp. 27–51, 2011.

[97]   M. Srinivasarao, "Nano-Optics in the Biological World: Beetles, Butterflies, Birds, and Moths," *Chem. Rev.*, vol. 99, no. 7, pp. 1935–1962, Jul. 1999.

[98]   X. Shi, W. Gu, C. Zhang, L. Zhao, W. Peng, and Y. Xian, "A label-free colorimetric sensor for Pb2+ detection based on the acceleration of gold leaching by graphene oxide," *Dalton Trans.*, vol. 44, no. 10, pp. 4623–4629, Feb. 2015.

[99]   S. Kim, S. G. Han, Y. G. Koh, H. Lee, and W. Lee, "Colorimetric Humidity Sensor Using Inverse Opal Photonic Gel in Hydrophilic Ionic Liquid," *Sensors*, vol. 18, no. 5, p. 1357, May 2018.

[100]   A. Choe, J. Yeom, R. Shanker, M. P. Kim, S. Kang, and H. Ko, "Stretchable and wearable colorimetric patches based on thermoresponsive plasmonic microgels embedded in a hydrogel film," *NPG Asia Materials*, vol. 10, no. 9, p. 912, Sep. 2018.

[101]   E. P. Chan, J. J. Walish, A. M. Urbas, and E. L. Thomas, "Mechanochromic Photonic Gels," *Adv. Mater.*, vol. 25, no. 29, pp. 3934–3947, Aug. 2013.

[102]   I. B. Burgess, M. Lončar, and J. Aizenberg, "Structural colour in colourimetric sensors and indicators," *J. Mater. Chem. C*, vol. 1, no. 38, pp. 6075–6086, Sep. 2013.

[103]   J. Sun, B. Bhushan, and J. Tong, "Structural coloration in nature," *RSC Advances*, vol. 3, no. 35, pp. 14862–14889, 2013.

[104]   A. K. Yetisen *et al.*, "Photonic hydrogel sensors," *Biotechnology Advances*, vol. 34, no. 3, pp. 250–271, May 2016.

[105] R. Zhang, Q. Wang, and X. Zheng, "Flexible mechanochromic photonic crystals: routes to visual sensors and their mechanical properties," *Journal of Materials Chemistry C*, vol. 6, no. 13, pp. 3182–3199, 2018.

[106] J.-P. Couturier, M. Sütterlin, A. Laschewsky, C. Hettrich, and E. Wischerhoff, "Responsive Inverse Opal Hydrogels for the Sensing of Macromolecules," *Angew. Chem. Int. Ed.*, vol. 54, no. 22, pp. 6641–6644, May 2015.

[107] H. Fudouzi and T. Sawada, "Photonic Rubber Sheets with Tunable Color by Elastic Deformation," *Langmuir*, vol. 22, no. 3, pp. 1365–1368, Jan. 2006.

[108] H. Fudouzi, T. Sawada, Y. Tanaka, I. Ario, T. Hyakutake, and I. Nishizaki, "Smart photonic coating as a new visualization technique of strain deformation of metal plates," 2012, vol. 8345, pp. 83451S-83451S–7.

[109] N. L. Privorotskaya, C. J. Choi, B. T. Cunningham, and W. P. King, "Sensing micrometer-scale deformations via stretching of a photonic crystal," *Sensors and Actuators A: Physical*, vol. 161, no. 1, pp. 66–71, Jun. 2010.

[110] S. Zeng *et al.*, "Bio-inspired sensitive and reversible mechanochromisms via strain-dependent cracks and folds," *Nature Communications*, vol. 7, p. 11802, Jul. 2016.

[111] T. Karrock and M. Gerken, "Pressure sensor based on flexible photonic crystal membrane," *Biomed Opt Express*, vol. 6, no. 12, pp. 4901–4911, Nov. 2015.

[112] L. Zhu, J. Kapraun, J. Ferrara, and C. J. Chang-Hasnain, "Flexible photonic metastructures for tunable coloration," *Optica, OPTICA*, vol. 2, no. 3, pp. 255–258, Mar. 2015.

[113] J. E. Sader, "Surface stress induced deflections of cantilever plates with applications to the atomic force microscope: V-shaped plates," *Journal of Applied Physics*, vol. 91, no. 11, pp. 9354–9361, May 2002.

[114] E. Reissner and M. Stein, "Torsion and transverse bending of cantilever plates," Jun. 1951.

[115] M. J. Lachut and J. E. Sader, "Buckling of a cantilever plate uniformly loaded in its plane with applications to surface stress and thermal loads," *Journal of Applied Physics*, vol. 113, no. 2, p. 024501, Jan. 2013.

[116] M. Urdampilleta *et al.*, "Molecule-based microelectromechanical sensors," *Scientific Reports*, vol. 8, no. 1, p. 8016, May 2018.

[117] R. Mathew and A. R. Sankar, "Design of a triangular platform piezoresistive affinity microcantilever sensor for biochemical sensing applications," *J. Phys. D: Appl. Phys.*, vol. 48, no. 20, p. 205402, Apr. 2015.

[118] J. Sun, B. Bhushan, J. Tong, and RSC, "Structural coloration in nature.," vol. 3 SRC-BaiduScholar, pp. 14862–14889, 2013.

[119] I. Burgess and J. Aizenberg, "Structural colour in colourimetric sensors and indicators.," *J Mater Chem C*, vol. 1 SRC-BaiduScholar, pp. 6075–6086, 2013.

[120] S. Zeng, "Bio-inspired sensitive and reversible mechanochromisms via strain-dependent cracks and folds.," *Nat Commun 7*, vol. 11802, no. 2016 SRC-BaiduScholar.

[121] A. Yetisen, "Photonic hydrogel sensors.," *Biotechnol Adv*, vol. 34, pp. 250–271, 2016.

[122] J. W. Gibbs, "On the equilibrium of heterogeneous substances," *American Journal of Science*, vol. s3-16, no. 96, pp. 441–458, Dec. 1878.

[123] R. C. Cammarata, "Surface and interface stress effects in thin films," *Progress in Surface Science*, vol. 46, no. 1, pp. 1–38, May 1994.

[124] D. Kramer, "Dependence of surface stress, surface energy and surface tension on potential and charge," *Physical Chemistry Chemical Physics*, vol. 10, no. 1, pp. 168–177, 2008.

[125] R. Shuttleworth, "The Surface Tension of Solids," *Proc. Phys. Soc. A*, vol. 63, no. 5, pp. 444–457, May 1950.

[126] Stoney George Gerald and Parsons Charles Algernon, "The tension of metallic films deposited by electrolysis," *Proceedings of the Royal Society of London. Series A, Containing Papers of a Mathematical and Physical Character*, vol. 82, no. 553, pp. 172–175, May 1909.

[127] R. Koch, "The intrinsic stress of polycrystalline and epitaxial thin metal films," *J. Phys.: Condens. Matter*, vol. 6, no. 45, pp. 9519–9550, Nov. 1994.

[128] J. M. Gere and S. P. Timoshenko, *Mechanics of materials*. Boston: PWS Publishing Company, 1997.

[129] C. A. Klein, "How accurate are Stoney's equation and recent modifications," *Journal of Applied Physics*, vol. 88, no. 9, pp. 5487–5489, Oct. 2000.

[130] K. Dahmen, S. Lehwald, and H. Ibach, "Bending of crystalline plates under the influence of surface stress — a finite element analysis," *Surface Science*, vol. 446, no. 1, pp. 161–173, Feb. 2000.

[131] S. W.-K. Timoshenko, *Theory of Plates and Shells*, 2nd ed. New York: McGraw-Hill.

[132] J. Li and W. K. Schomburg, "Metal strain gauges on membranes at large deflection," *Meas. Sci. Technol.*, vol. 24, no. 10, p. 105108, Sep. 2013.

[133] Syed Ali Ashter, *Thermoforming of Single and Multilayer Laminates*. Elsevier Inc., 2014.

[134] J.-Y. Sheng, L.-Y. Zhang, B. Li, G.-F. Wang, and X.-Q. Feng, "Bulge test method for measuring the hyperelastic parameters of soft membranes," *Acta Mech*, vol. 228, no. 12, pp. 4187–4197, Dec. 2017.

[135] X. Qian *et al.*, "Characterizing the Deformation of the Polydimethylsiloxane (PDMS) Membrane for Microfluidic System through Image Processing," *Micromachines (Basel)*, vol. 7, no. 5, May 2016.

[136] A. L. Thangawng, R. S. Ruoff, M. A. Swartz, and M. R. Glucksberg, "An ultra-thin PDMS membrane as a bio/micro–nano interface: fabrication and characterization," *Biomed Microdevices*, vol. 9, no. 4, pp. 587–595, Aug. 2007.

[137] F. Michielin, E. Serena, P. Pavan, and N. Elvassore, "Microfluidic-assisted cyclic mechanical stimulation affects cellular membrane integrity in a human muscular dystrophy in vitro model," *RSC Adv.*, vol. 5, no. 119, pp. 98429–98439, Nov. 2015.

[138] C. S. Lin *et al.*, "Mechanical Properties Measurement of Polymer Films by Bulge Test and Fringe Projection," *Advances in Materials Science and Engineering*, p. 12, 2014.

[139] P. Martins, C. Malhaire, S. Brida, and D. Barbier, "On the determination of Poisson's ratio of stressed monolayer and bilayer submicron thick films," *Microsyst Technol*, vol. 15, no. 9, pp. 1343–1348, Sep. 2009.

[140] W. K. Schomburg, *Introduction to Microsystem Design*, 2nd ed. Berlin Heidelberg: Springer-Verlag, 2015.

[141] W. K. Schomburg, Z. Rummler, P. Shao, K. Wulff, and L. Xie, "The design of metal strain gauges on diaphragms," *J. Micromech. Microeng.*, vol. 14, no. 7, pp. 1101–1108, Jun. 2004.

[142] J. Zi *et al.*, "Coloration strategies in peacock feathers," *PNAS*, vol. 100, no. 22, pp. 12576–12578, Oct. 2003.

[143] Seago Ainsley E, Brady Parrish, Vigneron Jean-Pol, and Schultz Tom D, "Gold bugs and beyond: a review of iridescence and structural colour mechanisms in beetles (Coleoptera)," *Journal of The Royal Society Interface*, vol. 6, no. suppl_2, pp. S165–S184, Apr. 2009.

[144] E. G. Loewen and E. Popov, *Diffraction Gratings and Applications*. CRC Press, 1997.

[145] Christopher Palmer, *Diffraction Grating Handbook*, 7th ed. 2014.

[146] A. Heinrich, J. Bischoff, K. Meiner, U. Richter, T. Mikolajick, and I. Dirnstorfer, "Interpretation of azimuthal angle dependence of periodic gratings in Mueller matrix spectroscopic ellipsometry," *J. Opt. Soc. Am. A, JOSAA*, vol. 32, no. 4, pp. 604–610, Apr. 2015.

[147] E. Armstrong and C. O'Dwyer, "Artificial opal photonic crystals and inverse opal structures – fundamentals and applications from optics to energy storage," *J. Mater. Chem. C*, vol. 3, no. 24, pp. 6109–6143, Jun. 2015.

[148] E. Armstrong and C. O'Dwyer, "Artificial opal photonic crystals and inverse opal structures – fundamentals and applications from optics to energy storage," *J. Mater. Chem. C*, vol. 3, no. 24, pp. 6109–6143, Jun. 2015.

[149] E. Popov, "Introduction to Diffraction Gratings: Summary of Applications," *HAL archives-overtes*, no. 2012, pp. 1–23, 2012.

[150] G. Zyla *et al.*, "Generation of bioinspired structural colors via two-photon polymerization," *Scientific Reports*, vol. 7, no. 1, p. 17622, Dec. 2017.

[151] R. Zhang, Q. Wang, and X. Zheng, "Flexible mechanochromic photonic crystals: routes to visual sensors and their mechanical properties," *Journal of Materials Chemistry C*, vol. 6, no. 13, pp. 3182–3199, 2018.

[152] X. Liang, R. Dong, and J. C. Ho, "Self-Assembly of Colloidal Spheres toward Fabrication of Hierarchical and Periodic Nanostructures for Technological Applications," *Advanced Materials Technologies*, vol. 4, no. 3, p. 1800541, Mar. 2019.

[153] D. K. Yi, M. J. Kim, L. Turner, K. S. Breuer, and D.-Y. Kim, "Colloid Lithography-Induced Polydimethylsiloxane Microstructures and their Application to Cell Patterning," *Biotechnology Letters*, vol. 28, no. 3, pp. 169–173, Feb. 2006.

[154] J.-T. Zhang, L. Wang, D. N. Lamont, S. S. Velankar, and S. A. Asher, "Fabrication of Large-Area Two-Dimensional Colloidal Crystals," *Angewandte Chemie International Edition*, vol. 51, no. 25, pp. 6117–6120, Jun. 2012.

[155] J.-Y. Choi, T. L. Alford, and C. B. Honsberg, "Solvent-Controlled Spin-Coating Method for Large-Scale Area Deposition of Two-Dimensional Silica Nanosphere Assembled Layers," *Langmuir*, vol. 30, no. 20, pp. 5732–5738, May 2014.

[156] Z. Cai, N. L. Smith, J.-T. Zhang, and S. A. Asher, "Two-Dimensional Photonic Crystal Chemical and Biomolecular Sensors," *Analytical Chemistry*, vol. 87, no. 10, pp. 5013–5025, May 2015.

[157] S. Yu, Z. Han, X. Jiao, D. Chen, and C. Li, "Ultrathin polymer gel-infiltrated monolayer colloidal crystal films for rapid colorimetric chemical sensing," *RSC Advances*, vol. 6, no. 70, pp. 66191–66196, 2016.

[158] C. Zhou, X. Gong, J. Han, and R. Guo, "Ethanol vapor-induced fabrication of colloidal crystals with controllable layers and photonic properties," *Soft Matter*, vol. 11, no. 13, pp. 2555–2562, 2015.

[159] N. Vogel, S. Goerres, K. Landfester, and C. K. Weiss, "A Convenient Method to Produce Close- and Non-close-Packed Monolayers using Direct Assembly at the Air-Water Interface and Subsequent Plasma-Induced Size Reduction," *Macromolecular Chemistry and Physics*, vol. 212, no. 16, pp. 1719–1734, Aug. 2011.

[160] H. J. Nam, J.-H. Kim, D.-Y. Jung, J. B. Park, and H. S. Lee, "Two-dimensional nanopatterning by PDMS relief structures of polymeric colloidal crystals," *Applied Surface Science*, vol. 254, no. 16, pp. 5134–5140, Jun. 2008.

[161] K. Matsubara, M. Watanabe, and Y. Takeoka, "A Thermally Adjustable Multicolor Photochromic Hydrogel," *Angewandte Chemie*, vol. 119, no. 10, pp. 1718–1722, Feb. 2007.

[162] T. Ding *et al.*, "Revealing Invisible Photonic Inscriptions: Images from Strain," *ACS Appl. Mater. Interfaces*, vol. 7, no. 24, pp. 13497–13502, Jun. 2015.

[163] T. Ito, C. Katsura, H. Sugimoto, E. Nakanishi, and K. Inomata, "Strain-Responsive Structural Colored Elastomers by Fixing Colloidal Crystal Assembly," *Langmuir*, vol. 29, no. 45, pp. 13951–13957, Nov. 2013.

[164] B. Viel, T. Ruhl, and G. P. Hellmann, "Reversible Deformation of Opal Elastomers," *Chem. Mater.*, vol. 19, no. 23, pp. 5673–5679, Nov. 2007.

[165] Y. Cho *et al.*, "Elastoplastic Inverse Opals as Power-Free Mechanochromic Sensors for Force Recording," *Adv. Funct. Mater.*, vol. 25, no. 38, pp. 6041–6049, Oct. 2015.

[166] Y. Fang, Y. Ni, S.-Y. Leo, C. Taylor, V. Basile, and P. Jiang, "Reconfigurable photonic crystals enabled by pressure-responsive shape-memory polymers," *Nature Communications*, vol. 6, p. 7416, Jun. 2015.

[167] A. Chiappini, A. Piotrowska, M. Marciniak, M. Ferrari, and D. Zonta, "Design and fabrication of mechanochromic photonic crystals as strain sensor," presented

at the SPIE Smart Structures and Materials + Nondestructive Evaluation and Health Monitoring, San Diego, California, United States, 2015, p. 94350J.

[168] T. Erber, S. A. Guralnick, and S. C. Michels, "Hysteresis and Fatigue," *Annals of Physics*, vol. 224, no. 2, pp. 157–192, Jun. 1993.

[169] W. Song, A. Vasdekis, and D. Psaltis, "Elastomer based tunable optofluidic devices.," *Lab Chip*, vol. 12 SRC-BaiduScholar, pp. 3590–3597, 2012.

[170] Z. Ding *et al.*, "Surface profiling of an aspherical liquid lens with a varied thickness membrane," *Opt Express*, vol. 25, no. 4, pp. 3122–3132, Feb. 2017.

[171] K. Mishra, H. T. M. van den Ende, and F. G. Mugele, "Recent Developments in Optofluidic Lens Technology," *Micromachines*, vol. 7, no. 6, pp. 1–24, 2016.

[172] C. U. Murade, D. van der Ende, and F. Mugele, "High speed adaptive liquid microlens array," *Opt Express*, vol. 20, no. 16, pp. 18180–18187, Jul. 2012.

[173] A. Orth, E. Schonbrun, and K. B. Crozier, "Multiplexed pressure sensing with elastomer membranes," *Lab Chip*, vol. 11, no. 22, pp. 3810–3815, Oct. 2011.

[174] C.-H. D. Tsai and M. Kaneko, "On-chip pressure sensor using single-layer concentric chambers," *Biomicrofluidics*, vol. 10, no. 2, Mar. 2016.

[175] B. K. Wunderlich, U. A. Kleßinger, and A. R. Bausch, "Diffusive spreading of time-dependent pressures in elastic microfluidic devices," *Lab Chip*, vol. 10, no. 8, pp. 1025–1029, Apr. 2010.

[176] W. Song and D. Psaltis, "Optofluidic membrane interferometer: An imaging method for measuring microfluidic pressure and flow rate simultaneously on a chip," *Biomicrofluidics*, vol. 5, no. 4, pp. 044110-044110–11, Nov. 2011.

[177] C.-Y. Huang, Y. Matsuda, J. W. Gregory, H. Nagai, and K. Asai, "The applications of pressure-sensitive paint in microfluidic systems," *Microfluid Nanofluid*, vol. 18, no. 5–6, pp. 739–753, May 2015.

[178] C. Hoera, A. Kiontke, M. Pahl, and D. Belder, "A chip-integrated optical microfluidic pressure sensor," *Sensors and Actuators B: Chemical*, vol. 255, no. Part 2, pp. 2407–2415, Feb. 2018.

[179] B. Grzybowski, D. Qin, R. Haag, and G. M. Whitesides, "Elastomeric optical elements with deformable surface topographies: applications to force measurements, tunable light transmission and light focusing," *Sensors and Actuators A: Physical*, vol. 86, no. 1, pp. 81–85, Oct. 2000.

[180] Y.-C. Tung and K. Kurabayashi, "Nanoimprinted strain-controlled elastomeric gratings for optical wavelength tuning," *Appl. Phys. Lett.*, vol. 86, no. 16, p. 161113, Apr. 2005.

[181] C. T. Pada and R. A. Guerrero, "Fluid-enhanced tunable diffraction with an elastomeric grating," *OE, OPEGAR*, vol. 56, no. 5, p. 054101, May 2017.

[182] K. Hosokawa, K. Hanada, and R. Maeda, "A polydimethylsiloxane (PDMS) deformable diffraction grating for monitoring of local pressure in microfluidic devices," *J. Micromech. Microeng.*, vol. 12, no. 1, p. 1, 2002.

[183] P. Escudero, J. Yeste, R. Villa, and M. Alvarez, "Low cost nanomechanical surfaces stress based sensors fabricated by hybrid materials.," in *102460P*, vol. 0246 SRC-BaiduScholar, 2017.

[184] E. Armstrong and C. Dwyer, "Artificial opal photonic crystals and inverse opal structures-fundamentals and applications from optics to energy storage.," *J Mater Chem C*, vol. 3 SRC-BaiduScholar, pp. 6109–6143, 2015.

[185] F. Michielin, E. Serena, P. Pavan, N. Elvassore, and RSC, "Microfluidic-assisted cyclic mechanical stimulation affects cellular membrane integrity in a human muscular dystrophy in vitro model.," vol. 5 SRC-BaiduScholar, pp. 98429–98439, 2015.

[186] "Available at: https://gitlab.com/c-p/peakevo."

[187] Z. Cai, N. L. Smith, J.-T. Zhang, and S. A. Asher, "Two-Dimensional Photonic Crystal Chemical and Biomolecular Sensors," *Anal. Chem.*, vol. 87, no. 10, pp. 5013–5025, May 2015.

[188] A. Raj, P. Suthanthiraraj, and A. Sen, "Pressure-driven flow through PDMS-based flexible microchannels and their applications in microfluidics.," *Microfluid Nanofluidics 22*, vol. 128, no. 2018 SRC-BaiduScholar.

[189] T. Gervais, J. El-Ali, A. Günther, and K. F. Jensen, "Flow-induced deformation of shallow microfluidic channels," *Lab Chip*, vol. 6, no. 4, pp. 500–507, Mar. 2006.

[190] A. Raj, P. P. A. Suthanthiraraj, and A. K. Sen, "Pressure-driven flow through PDMS-based flexible microchannels and their applications in microfluidics," *Microfluid Nanofluid*, vol. 22, no. 11, p. 128, Oct. 2018.

[191] I. C. Christov, V. Cognet, T. C. Shidhore, and H. A. Stone, "Flow rate–pressure drop relation for deformable shallow microfluidic channels," *Journal of Fluid Mechanics*, vol. 841, pp. 267–286, Apr. 2018.

[192] R. Mathew and A. Ravi Sankar, "A Review on Surface Stress-Based Miniaturized Piezoresistive SU-8 Polymeric Cantilever Sensors," *Nano-Micro Lett.*, vol. 10, no. 2, p. 35, Feb. 2018.

[193] M. Alvarez and L. M. Lechuga, "Microcantilever-based platforms as biosensing tools.," *The Analyst*, vol. 135, no. 5, pp. 827–36, May 2010.

[194] H. Lim, T. Park, J. Na, C. Park, B. Kim, and E. Kim, "Construction of a photothermal Venus flytrap from conductive polymer bimorphs," *NPG Asia Materials*, vol. 9, no. 7, p. e399, Jul. 2017.

[195] Y. Cui *et al.*, "Transient thermo-mechanical analysis for bimorph soft robot based on thermally responsive liquid crystal elastomers," *Appl. Math. Mech.-Engl. Ed.*, vol. 40, no. 7, pp. 943–952, Jul. 2019.

[196] J. Li *et al.*, "Photothermal Bimorph Actuators with In-Built Cooler for Light Mills, Frequency Switches, and Soft Robots," *Advanced Functional Materials*, vol. 29, no. 27, p. 1808995, Jul. 2019.

[197] J. Li *et al.*, "Multi-responsive and multi-motion bimorph actuator based on super-aligned carbon nanotube sheets," *Carbon*, vol. 148, pp. 487–495, Jul. 2019.

[198] Z. L. Pianowski, "Recent Implementations of Molecular Photoswitches into Smart Materials and Biological Systems," *Chemistry – A European Journal*, vol. 25, no. 20, pp. 5128–5144, 2019.

[199] Y. Hu, Z. Li, T. Lan, and W. Chen, "Photoactuators for Direct Optical-to-Mechanical Energy Conversion: From Nanocomponent Assembly to Macroscopic Deformation," *Advanced Materials*, vol. 28, no. 47, pp. 10548–10556, 2016.

[200] V. Toshchevikov, J. Ilnytskyi, and M. Saphiannikova, "Photoisomerization Kinetics and Mechanical Stress in Azobenzene-Containing Materials," *J. Phys. Chem. Lett.*, vol. 8, no. 5, pp. 1094–1098, Mar. 2017.

[201] S. V. Serak, N. V. Tabiryan, T. J. White, and T. J. Bunning, "Azobenzene liquid crystal polymer-based membrane and cantilever optical systems," *Opt. Express, OE*, vol. 17, no. 18, pp. 15736–15746, Aug. 2009.

[202] N. Hosono *et al.*, "Photoinduced Deformation of Rigid Azobenzene-Containing Polymer Networks," *Macromolecules*, vol. 46, no. 3, pp. 1017–1026, Feb. 2013.

[203] L. Cheng *et al.*, "Photomechanical bending mechanics of polydomain azobenzene liquid crystal polymer network films," *Journal of Applied Physics*, vol. 112, no. 1, p. 013513, Jul. 2012.

[204] D. Baigl, "Photo-actuation of liquids for light-driven microfluidics: state of the art and perspectives," *Lab Chip*, vol. 12, no. 19, pp. 3637–3653, Aug. 2012.

[205] G. Petroffe, C. Wang, X. Sallenave, G. Sini, F. Goubard, and S. Péralta, "Fast and reversible photo-responsive wettability on TiO2 based hybrid surfaces," *J. Mater. Chem. A*, vol. 3, no. 21, pp. 11533–11542, May 2015.

[206] A. M. Moulin, S. J. O'Shea, R. A. Badley, P. Doyle, and M. E. Welland, "Measuring Surface-Induced Conformational Changes in Proteins," *Langmuir*, vol. 15, no. 26, pp. 8776–8779, Dec. 1999.

[207] H.-F. Ji and B. D. Armon, "Approaches to Increasing Surface Stress for Improving Signal-to-Noise Ratio of Microcantilever Sensors," *Anal. Chem.*, vol. 82, no. 5, pp. 1634–1642, Mar. 2010.

[208] J. L. Arlett, E. B. Myers, and M. L. Roukes, "Comparative advantages of mechanical biosensors," *Nat Nanotechnol*, vol. 6, no. 4, Apr. 2011.

[209] A. Goulet-Hanssens and C. J. Barrett, "Photo-control of biological systems with azobenzene polymers," *Journal of Polymer Science Part A: Polymer Chemistry*, vol. 51, no. 14, pp. 3058–3070, Jul. 2013.

[210] K. Kim, S. W. Park, and S. S. Yang, "The optimization of PDMS-PMMA bonding process using silane primer," *BioChip J*, vol. 4, no. 2, pp. 148–154, Jun. 2010.

[211] E. Merino and M. Ribagorda, "Control over molecular motion using the cis–trans photoisomerization of the azo group," *Beilstein J Org Chem*, vol. 8, pp. 1071–1090, Jul. 2012.

[212] D. G. Walter, D. J. Campbell, and C. A. Mirkin, "Photon-Gated Electron Transfer in Two-Component Self-Assembled Monolayers," *J. Phys. Chem. B*, vol. 103, no. 3, pp. 402–405, Jan. 1999.

[213] Z. Mahimwalla, K. G. Yager, J. Mamiya, A. Shishido, A. Priimagi, and C. J. Barrett, "Azobenzene photomechanics: prospects and potential applications," *Polymer Bulletin*, vol. 69, no. 8, pp. 967–1006, Nov. 2012.